

M-SSL-74-1
June 15, 1974

SPACE SCIENCES LABORATORY

(NASA-TM-X-70354) APOLLO-SKYLAB
CONTAMINATION PHOTOGRAPHY (S226) Final
Report (NASA) 99 p HC \$4.00 CSCL 22B

N74-33305

Unclas
G3/31 47614

APOLLO-SKYLAB CONTAMINATION PHOTOGRAPHY (S226)

FINAL REPORT

By

P. D. Craven and G. A. Gary



NATIONAL AERONAUTICS AND SPACE ADMINISTRATION

TECHNICAL REPORT STANDARD TITLE PAGE

1. REPORT NO. M-SSL-74-1	2. GOVERNMENT ACCESSION NO.	3. RECIPIENT'S CATALOG NO.	
4. TITLE AND SUBTITLE Apollo-Skylab Contamination Photography (S226) Final Report		5. REPORT DATE June 15, 1974	
		6. PERFORMING ORGANIZATION CODE	
7. AUTHOR(S) P. D. Craven and G. A. Gary		8. PERFORMING ORGANIZATION REPORT #	
9. PERFORMING ORGANIZATION NAME AND ADDRESS George C. Marshall Space Flight Center Marshall Space Flight Center, Alabama 35812		10. WORK UNIT NO.	
		11. CONTRACT OR GRANT NO.	
12. SPONSORING AGENCY NAME AND ADDRESS National Aeronautics and Space Administration Washington, D. C. 20546		13. TYPE OF REPORT & PERIOD COVERED Miscellaneous	
		14. SPONSORING AGENCY CODE	
15. SUPPLEMENTARY NOTES Prepared by Space Sciences Laboratory, Science and Engineering			
16. ABSTRACT Photographs taken on Apollo 16 before, during, and after a water dump are analyzed for residual background brightness, particle dynamics, and time decay of background brightness. No conclusive results were obtained because of the illumination of the windows or window openings by extraneous light sources, e.g., the moon.			
17. KEY WORDS		18. DISTRIBUTION STATEMENT Unclassified-unlimited G. A. Gary	
19. SECURITY CLASSIF. (of this report) Unclassified	20. SECURITY CLASSIF. (of this page) Unclassified	21. NO. OF PAGES 100	22. PRICE NTIS

TABLE OF CONTENTS

	Page
INTRODUCTION	1
DESCRIPTION OF EXPERIMENTS	3
DATA OBTAINED	6
CALIBRATION OF FILM	16
DATA DESCRIPTION	20
DATA RESULTS	29
Phase Function	29
Particle Dynamics	30
Decay of Background Brightness	36
Plume Structure	36
APPENDIX — A SPACECRAFT CONTAMINATION PARTICLE TRAJECTORY STUDY	43
REFERENCES	90

LIST OF ILLUSTRATIONS

Figure	Title	Page
1.	Geometry of the CSM and the coordinate system used	4
2.	θ , ϕ angles of earth, moon, and sun in first attitude for phase function of cloud; $\theta = 43$ and 73 deg	8
3.	θ , ϕ angles of earth, moon, and sun in second attitude for phase function of cloud; $\theta = 120$ and 150 deg	9
4.	θ , ϕ angles of earth, moon, and sun in attitude used for the water dump	10
5.	θ , ϕ angles of earth, moon, and sun in postdump attitude, window 2	11
6.	θ , ϕ angles of earth, moon, and sun in postdump attitude, window 4	12
7.	1-sec exposure through window 2 in first postdump performance	14
8.	1-sec exposure through window 4 in first postdump performance	14
9.	1-sec exposure through window 2 in last postdump performance	15
10.	1-sec exposure through window 4 in last postdump performance	15
11.	Calibration of 16-mm film, 1-sec exposure time; density read on microdensitometer	17
12.	B/B_{\odot} versus density for 1-sec exposure on 2485 film; film pre-exposed before sensitometric data put on; density read on MacBeth densitometer	18
13.	Calibration for 70-mm 2485 film; B/B_{\odot} calculated using $f/16$ and $1/125$ -sec exposure time	19

LIST OF ILLUSTRATIONS (Continued)

Figure	Title	Page
14.	Edge scan	26
15.	Computer printout of density readings on magnetic tape	28
16.	First phase function performance, 1/8-sec exposure	32
17.	First phase function performance, 1-sec exposure	33
18.	First phase function performance, 10-sec exposure	34
19.	Trace of all identifiable particle tracks; tracks are as seen from CM 2	35
20.	Orientation of CSM with respect to sun during S226 dump and postdump performance	37
21.	Decay of background brightness	38
22.	First 70-mm frame showing particles from water dump	39
23.	Second 70-mm frame showing particles from water dump	40
24.	Last 70-mm frame showing particles from water dump	41
A-1.	Particle coordinate system	45
A-2.	Camera coordinate system	45
A-3.	Transformation of \vec{R}_2	46
A-4.	Nozzle rotation angles	47
A-5.	Transformation of \vec{R}_3	48
A-6.	Position parameter $V \cdot t$	50
A-7.	The scattering angle Θ	52
A-8.	Spherical trigonometry	53

LIST OF ILLUSTRATIONS (Continued)

Figure	Title	Page
A-9.	The scattering angle Θ in terms of right ascension	55
A-10.	Coordinate systems for spacecraft motion considerations . . .	56
A-11.	Perspective projection	60
A-12.	Field-of-view boundaries	61
A-13.	Defocusing effects	62
A-14.	Computer plot of particle from water dump as seen in window 2; $\beta = 50$ deg and $\theta = 5, 0, -5, -10, -15, -20$ deg . . .	65
A-15.	Computer plot of particle from water dump as seen in window 2; $\beta = 60$ deg and $\theta = 5, 0, -5, -10, -15, -20$ deg . . .	66
A-16.	Surfaces of the cones formed by water dump as seen from window 2; cones are defined by β and generated by θ	67
A-17.	Effect of spacecraft rotation on particle tracks as seen from window 2; $\beta = 60$ deg and $\theta = 5, 0, -5, -10, -15$ deg	68
A-18.	Effect of spacecraft rotation on particle tracks as seen from window 4; $\beta = 60$ deg and $\theta = 5, 0, -5, -10, -15, -20$ deg . . .	69
A-19.	Effect of location of source on particle tracks	71
A-20.	Accumulation for trajectories of particles seen in Figure A-14	72
A-21.	Position of particle in 1-sec increments; $\theta = 0$ and $\beta = 60$ deg; window 1, water dump nozzle, and $V = 100$ cm/sec used to generate tracks	73
A-22.	Effective exposure versus time from emergence from nozzle; the effective radiance shows the $1/R^2$ effect	73
A-23.	Particle trajectories resulting from water dump from auxiliary dump nozzle and viewed from windows 2 and 4	75

LIST OF ILLUSTRATIONS (Concluded)

Figure	Title	Page
A-24.	Trajectory of particle from hatch dump nozzle as seen from window 2 and 4 simultaneously	76
A-25.	Trajectories of particles from water dump seen from window 4 with a DAC	77
A-26.	Trajectories of particles from urine dump seen from window 4 with a DAC	79
A-27.	Extended trajectories of particles from water and urine dumps as seen from window 4	81
A-28.	20-sec photographs of water and urine dump; photographs are from Apollo 15	82
A-29.	Selected tracks from Figure 28(a) ; particle A is associated with the water dump, and particle B with the urine dump nozzle	83
A-30.	Slope versus track length for particles from urine and water dump nozzle	84
A-31.	Example of stellar camera frame from Apollo 15 which records a particle shower	85
A-32.	Trajectories of Figure A-31 retraced to show relationship to particles from reaction control system A-1 engine and waste water dump	87
A-33.	Locus of origins for particle tracks seen in Apollo 15 stellar camera frame	88

LIST OF TABLES

Table	Title	Page
1.	Skylab Contamination Photography	2
2.	Summary of Cameras, Film, and Attitude	3
3.	Right Ascension and Declination for the CSM x and z Axis, Moon, Venus, and Mars	6
4.	Angles of Incidence for Moonlight on Apollo 16 Windows	13
5.	Identification of Files on Magnetic Tape	21
6.	File Numbers for Simultaneous Frames of Postdump	26
7.	Range of Brightness from 1-sec Exposures on 35-mm Film	30
8.	Sky Background in B/B_{\odot} at Phase Function Positions	31
A-1.	Water Dump Nozzle, $V = 1$ m/sec	78
A-2.	Urine Dump Nozzle, $V = 1$ m/sec	80
A-3.	Time Correlation of Dumps with Stellar Camera Frames Containing Contamination	86
A-4.	Time of Events which May Generate Particles	89

APOLLO-SKYLAB CONTAMINATION PHOTOGRAPHY (S226)

INTRODUCTION

The purpose of the Skylab Contamination Photography Experiment (S226) on Apollo 16 was to obtain data concerning exterior contamination induced by and associated with manned spacecraft. The functional test objectives were to measure the background brightness from the spacecraft coma, to obtain data on particulate size and dynamics during a dump of liquids, and to determine the decay of the background brightness resulting from these dumps [1].

The 35-mm Nikon camera with the 55-mm lens was used for the background brightness measurements. For the particle dynamics measurements, two 16-mm Data Acquisition Cameras (DAC) and the 70-mm Hasselblad Electric Camera (HEC) were used. Kodak type 2485 film was used for all portions of the experiment.

Exposures to record the background brightness of the residual contamination cloud were to be taken (1) in lunar orbit at sunrise or sunset in and out of sunlight, (2) after the transearth injection burn but prior to the first waste water dump, and (3) at a time late in the transearth coast. These exposures were expected to give, through photographic photometry, data on the amount of light scattered by the contamination cloud for several scattering angles, establish the buildup of contamination in lunar orbit and in transearth coast, and establish a baseline contamination environment.

The waste water dump was performed using the auxiliary urine dump nozzle on the Command Module (CM). During the dump, a 70-mm HEC and a 16-mm DAC were employed to record the actual dump event and give data on plume structure and particle dynamics. A second series of photographs was taken using two 16-mm DAC's to provide stereoscopic views of postdump conditions for analysis of particle size, dynamics, and stay times. The experiment was planned so that the distance of particles from the camera could be ascertained. Distance from the camera is an essential parameter in determining sizes and trajectories.

As a result of real-time changes in the mission, all lunar orbit photography and the early transearth coast sequences were not performed. Table 1 gives the planned sequence and the sequence actually obtained as a result of real-time changes in the mission. Table 2 is a synopsis of the spacecraft attitudes, cameras, and camera settings used for the photographs obtained.

TABLE 1. SKYLAB CONTAMINATION PHOTOGRAPHY

Objective	Sequence	Results
Background	Double-Umbra Lunar Orbit Sunlit at (60° and 90°)	Cancelled (Early Return)
Growth Rate of Residual/Baseline	TEI/Post Water Dump (60°)	Cancelled (Crew Slept Late)
Phase Function of Residual Debris Cloud and Growth	Late TEI (60°, 90°, 120°, 150°)	Obtained 18 Nikon Frames (35 mm)
Dynamics and Structure of Nozzle Dump	Auxiliary Hatch Dump	Obtained 7 Hasselblad Frames (70 mm)
Stay Time, Dynamics, and Physical Properties	Postdump	Obtained 16 mm — Dual Camera Clean Nozzle

TABLE 2. SUMMARY OF CAMERAS, FILM, AND ATTITUDE

Operational Time	Camera	Film	Exposure (sec)	Focus (ft)	f Stop	Lens	Attitude		
								Elev. (deg)	Azim. (deg)
Phase Function	35 mm, N	2485	100, 10, 1, 1/8	∞	1.2	55 mm 3EB33100009-301 Serial No. 1004	Sun	43	180
							Earth	78	169
							Moon	134	359
							Sun	120	181
							Earth	120	222
Moon	60	4							
Dump	70 mm, H	2485	1/125	6	16	80 mm Serial No. 1052			
	16 mm, D	2485			T8	SEB33100018-301			
					Time to Run (sec)				
			1/125	∞	15		Sun	60	180
			1/500	∞	15		Earth	69	142
			1/500	10	15		Moon	119	367
			1/125	10	15				
			1/60	10	15				
			1/125	10	15				
			1/500	10	15				
			1/500	∞	15				
			1/125	∞	15				
			1/60	∞	15				
Postdump	D (2 simultaneous)	2485	10, 5, 1, 1/60	∞	T1 (f/0.95)	18 mm SEB33100018-301 Serial No. 1032 and 1035	Sun Earth Moon	177 120 C2	250 209 67

D DAC

H Hassleblad

N Nikon

Elevation and azimuth are with respect to spacecraft as shown in Figure 1.

DESCRIPTION OF EXPERIMENTS

Two spacecraft orientations and two camera positions were required to map the phase function. The bracket which holds the Nikon camera has two positions. In one position the line of sight of the camera is along the +x axis (Fig. 1), and in the other it is 30 deg from the +x axis toward the -z axis of the Command Service Module (CSM). As shown in Table 2, the CSM was oriented with the +x axis 43 deg and 120 deg from the sun. Using the two

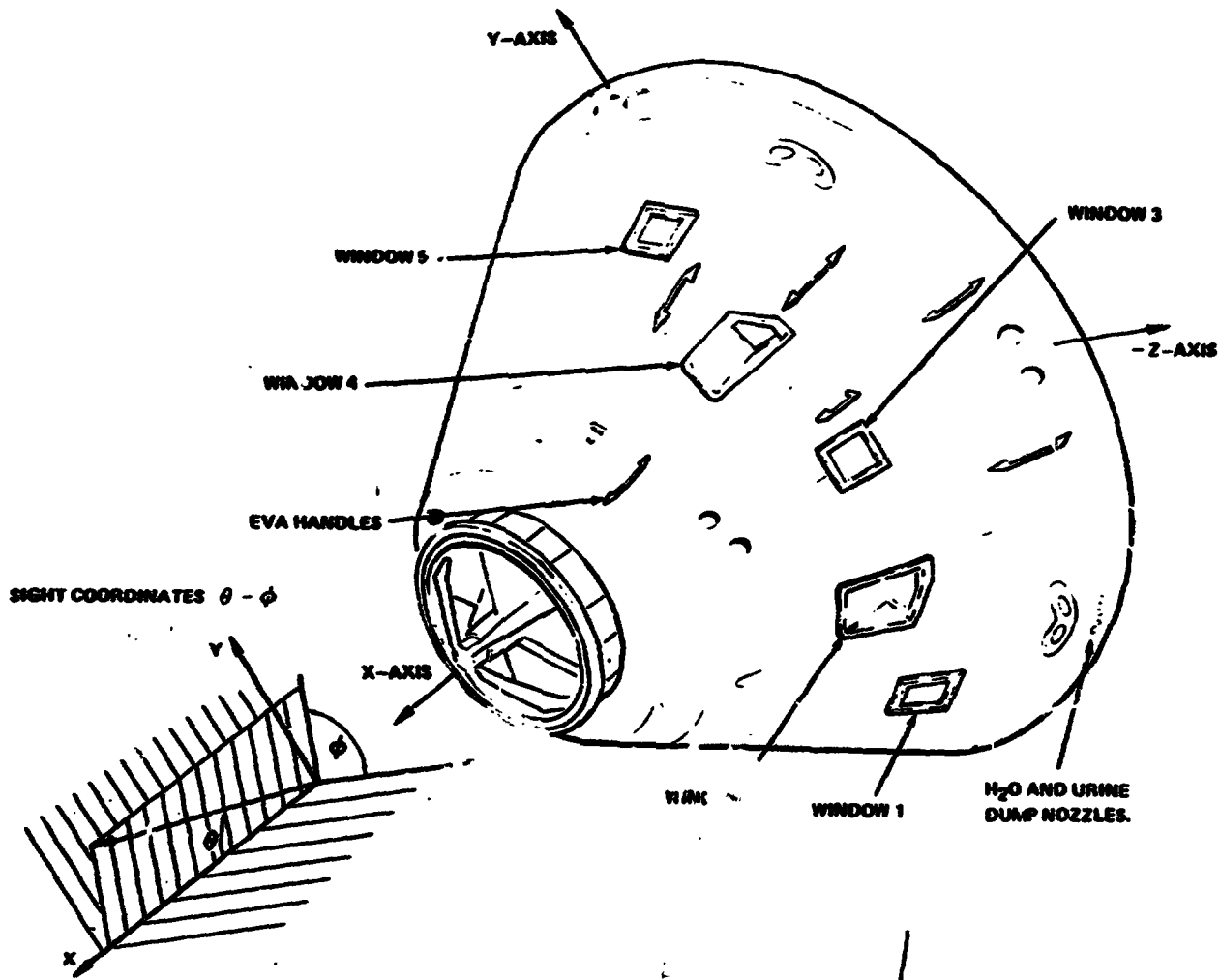


Figure 1. Geometry of the CSM and the coordinate system used.

camera positions, the line of sight of the camera was positioned at 43, 73, 126, and 150 deg from the sun. Four photographs (one exposure each of 100, 10, 1 and 1/8 sec) were taken at each position. Spacecraft rates were allowed to damp to less than 0.05 deg/sec before photographs were taken; interior lights were dimmed, and the camera shield for the Nikon was used. The magazine identification for this film is X.

A bracket-mounted DAC (which looks along the +x direction) and a hand-held Hasselblad were used for photography during the dump. The DAC was mounted in window 2 (loaded with magazine MM), and the Hasselblad (loaded with magazine TT) was used in window 3. Spacecraft rates were allowed to damp, interior lights were dimmed, and window shades were installed in CM windows 1 and 5. Table 2 gives the settings for each camera. A total of seven frames was taken with the HEC.

To eliminate the effects of previous dumps, the auxiliary urine dump nozzle was used. This nozzle is next to the hatch window (window 3) and has coordinates of

10° 32' from -z toward -y

10.16 cm in x, toward -x, from x coordinate of center of window 3.

Approximately 3.55 kg of potable water were dumped, using cabin pressure as the driving force. This was accomplished by filling a water enhancement bag and connecting the bag to the urine dump line. Immediately after the dump was initiated, the water in the line (inside the CSM) to the dump nozzle froze. The line was consequently disassembled and reassembled to restore the water flow. No further trouble was encountered, and the dump proceeded smoothly; some water was lost, but the exact amount is unknown. According to the Command Module Pilot, the dump required approximately 6 to 10 min to complete. Table 2 gives the schedule for the photographs taken with the DAC and the Hasselblad. Table 3 gives the right ascension and declination of the x and z axis for each spacecraft attitude. The position of the moon, Venus, and Mars is also given.

After completion of the dump, the CSM was maneuvered so that its +x axis was in the direction of the dump. Window shades were installed in CM window 3. Two DAC cameras pointed in the same direction, one in window 2 and one in window 4, were used to take simultaneous photographs. The DAC in window 4 was loaded with magazine HH.

**TABLE 3. RIGHT ASCENSION AND DECLINATION FOR THE CSM
x AND z AXIS, MOON, VENUS, AND MARS**

Test Objectives	Component	Magnitude	Right Ascension (hr:min)	Declination (deg:min)
Phase Function 1	x axis		5:16	23:04
	z axis		23:23	-03:58
Phase Function 2	x axis		12:10	-70:56
	z axis		02:44	-15:09
Postdump	x axis		15:02	47:22
	z axis		21:12	26:12
	Moon	See Note	13:30	14:47
	Venus	-4.2	5:19	27:16
	Mars	1.8	5:16	24:11

Note: The experiment was performed at approximately 12:00 hours GMT April 27. The moon reached opposition at 12:44 hours GMT April 28.

Three sets of nine photographs were taken with each camera. The first set was exposed as soon as the CSM attained the attitude. Three photographs each at 5-, 1-, and 1/60-sec exposures were taken. After 5 min, a second set was obtained using the same exposure times. A set with exposure times of 10, 5, and 1 sec was taken 15 min after the first set was taken. Between each set there are 2 sec of film run at 24 frames/sec and 1000-sec exposure time.

DATA OBTAINED

All frames of the S226 photography were plagued by moonlight shining on the CM windows. This unfortunate effect resulted because the Apollo 16 returned 1 day earlier than planned.

Figures 2 through 6 show the positions of the three most important light sources, the sun, earth and moon, in terms of CM polar angles. If the source is below the bottom line in the figure, the light from the source is shining directly on the window. If the source is between the two lines, the window opening, but not the window, is illuminated. As seen from the figures, the only part of S226 in which moonlight was not directly on the window was the phase function photography with a sun angle of 43 deg. Even in this part, light was on the window opening. The angles of incidence of moonlight on the windows are given in Table 4.

Problems with light on the window opening were also experienced during photography for contamination studies on Apollo 15 [2].

An examination of the postdump photographs shows (Figs. 7 through 10) that those taken through CM window 2 are more exposed than those taken through CM window 4. Figures 7 and 8 are 1-sec exposures from the first postdump performance. Figures 9 and 10 are 1-sec exposures from the last postdump performance. The maximum brightness on CM window 2, as determined from the 1-sec exposures, is approximately $1.5 \times 10^{-12} B/B_{\odot}$. In CM 4 the maximum is approximately $4.5 \times 10^{-13} B/B_{\odot}$. This is a factor of about 3.3 difference. The angle of incidence for moonlight on these windows does differ somewhat. However, the transmission of the window should decrease as the angle of incidence increases. Therefore, CM 4 should have less exposure than CM 2, the opposite of the actual condition. The scattering angle for material on the window is the same for both windows so that for windows with equal amounts of material on them, there should be no difference in the light scattered into the camera. To account for the difference using scattered light, one window would have to be considerably more contaminated than the other. In fact, CM 2 would have to have a scattering efficiency S , found from Reference 2,

$$B = 3.1 \times 10^{-10} SB_{\odot} ,$$

of 0.005. This is not unreasonable for a window exposed to the space environment for 272 hours. The crew, in the debriefing, noted that condensation on the windows was a problem that resulted from delaying normal passive thermal control maneuvers. They also noted that none of the windows frosted over during the dump. Contamination on the window plus small amounts of condensation could account for the scattering efficiency. However, it is difficult to account for the differences in the windows using this argument because both windows were exposed to the same environment.

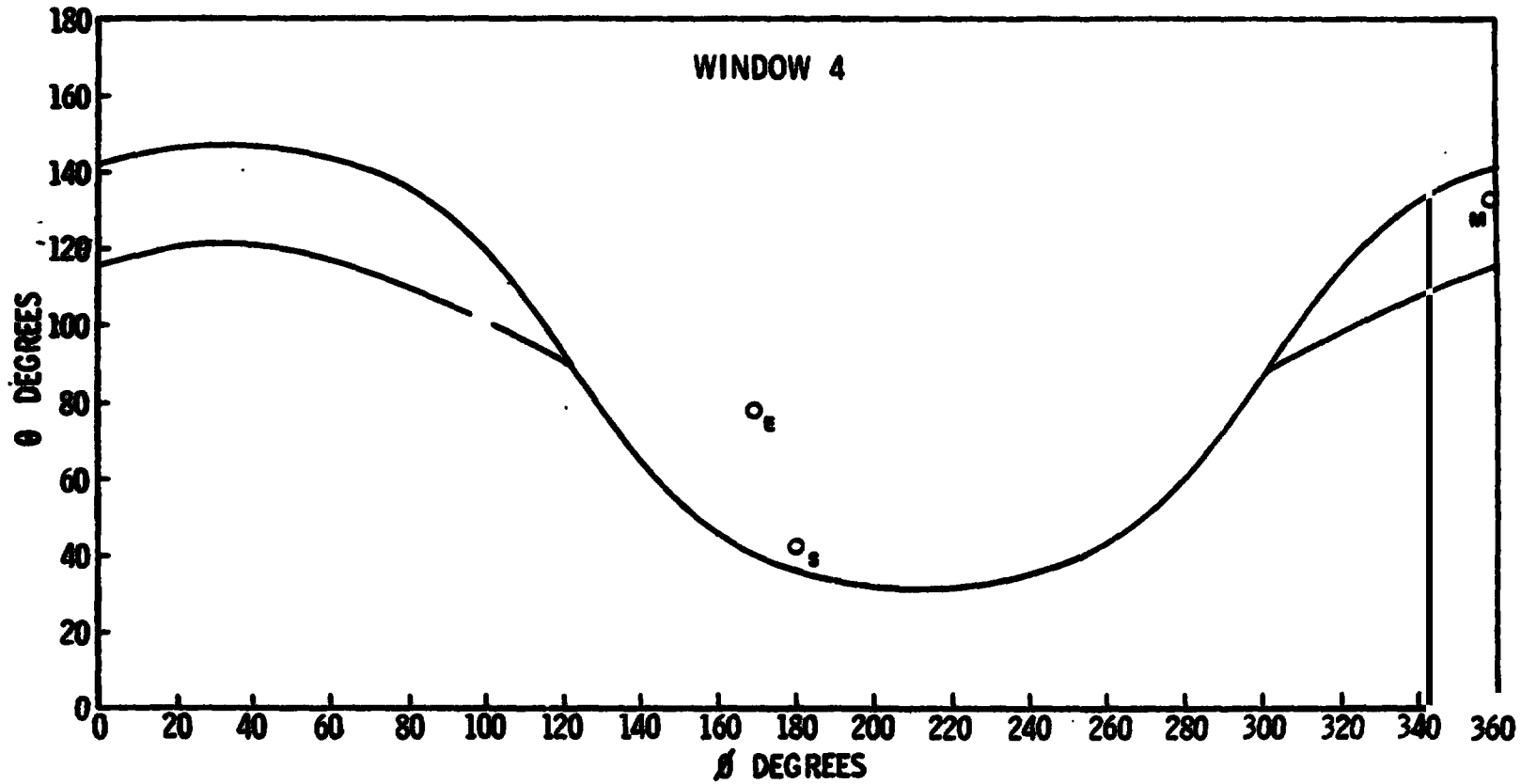


Figure 2. θ , ϕ angles of earth, moon, and sun in first attitude for phase function of cloud; $\theta = 43$ and 73 deg.

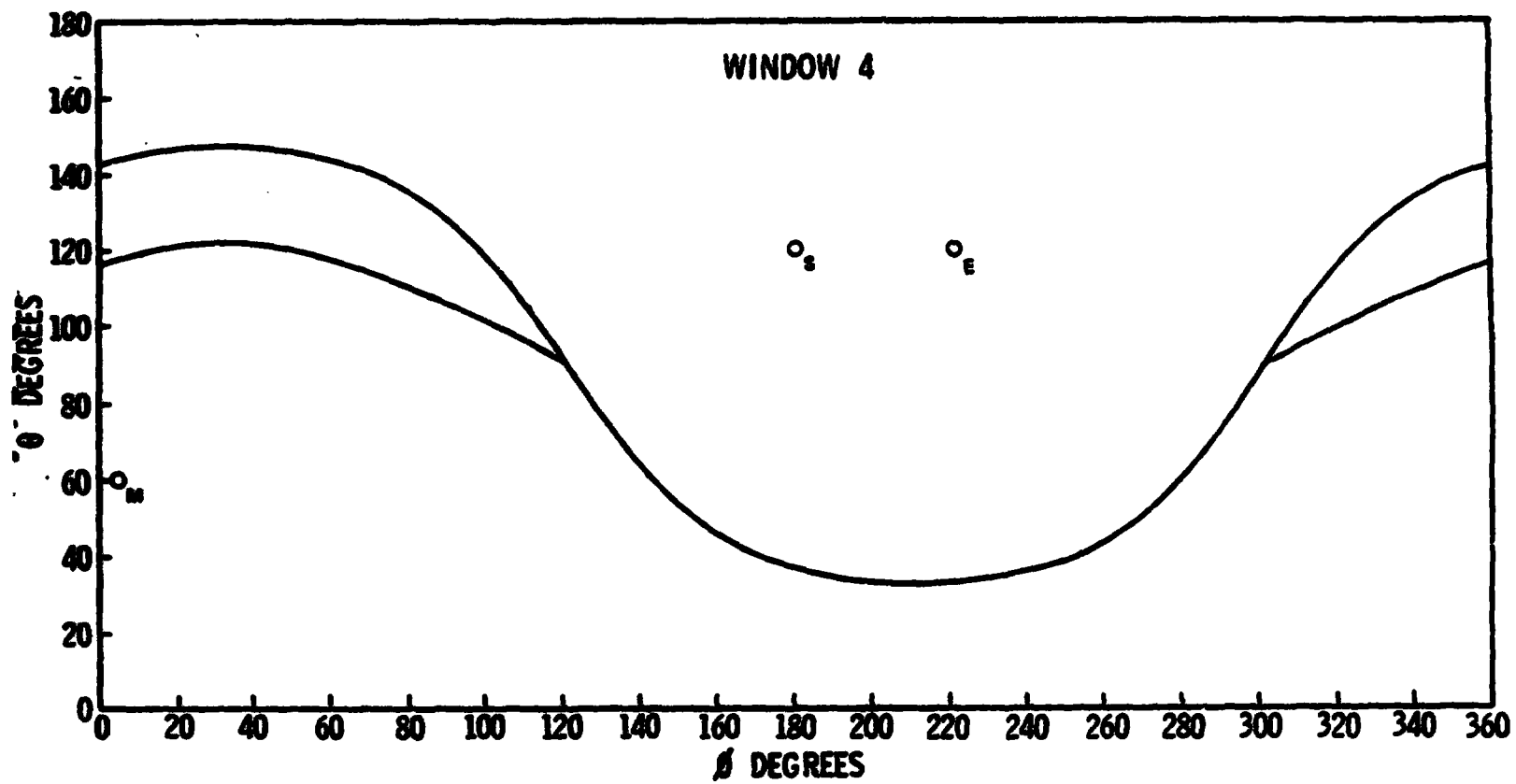


Figure 3. θ , ϕ angles of earth, moon, and sun in second attitude for phase function of cloud; $\theta = 120$ and 150 deg.

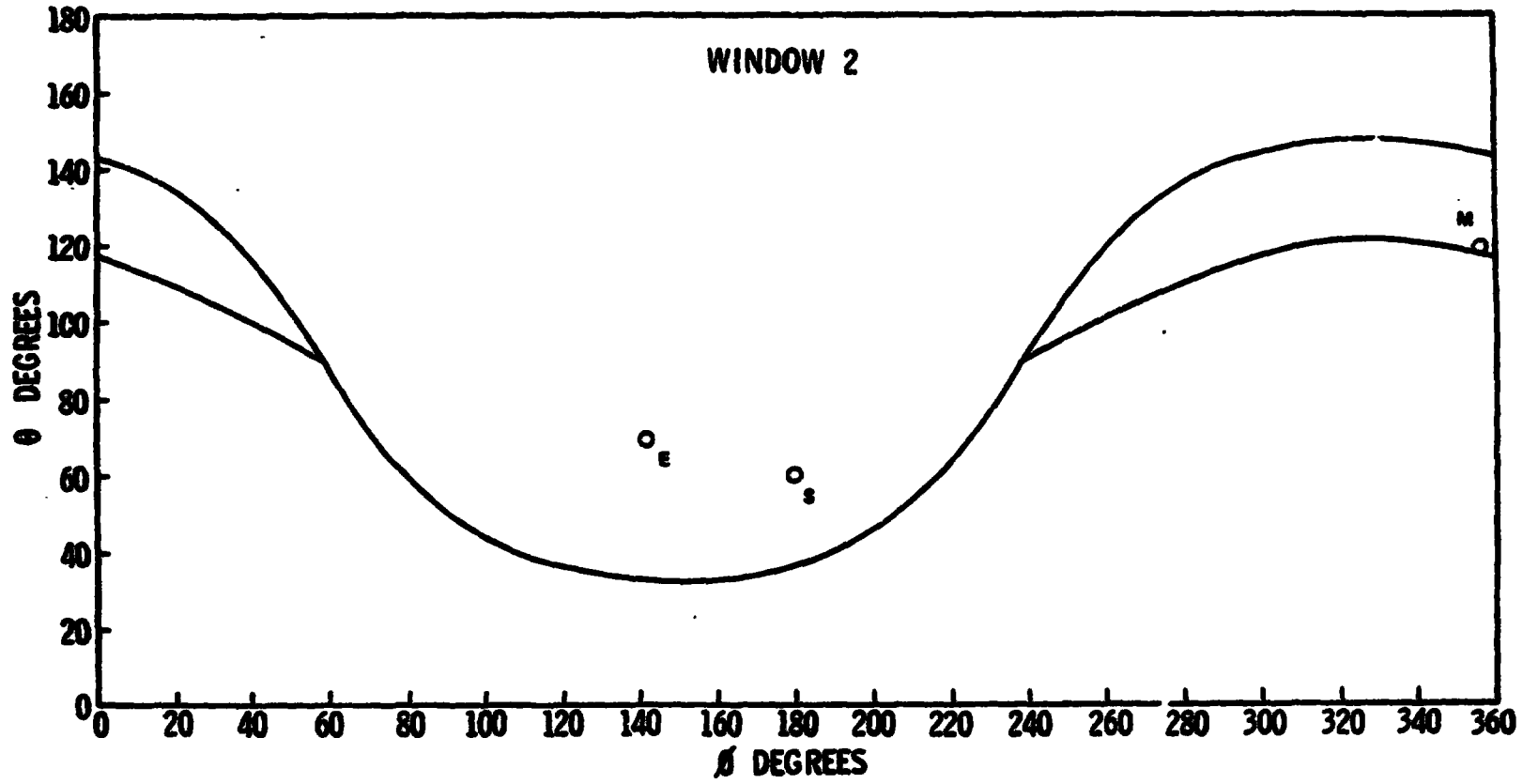


Figure 4. θ , ϕ angles of earth, moon, and sun in attitude used for the water dump.

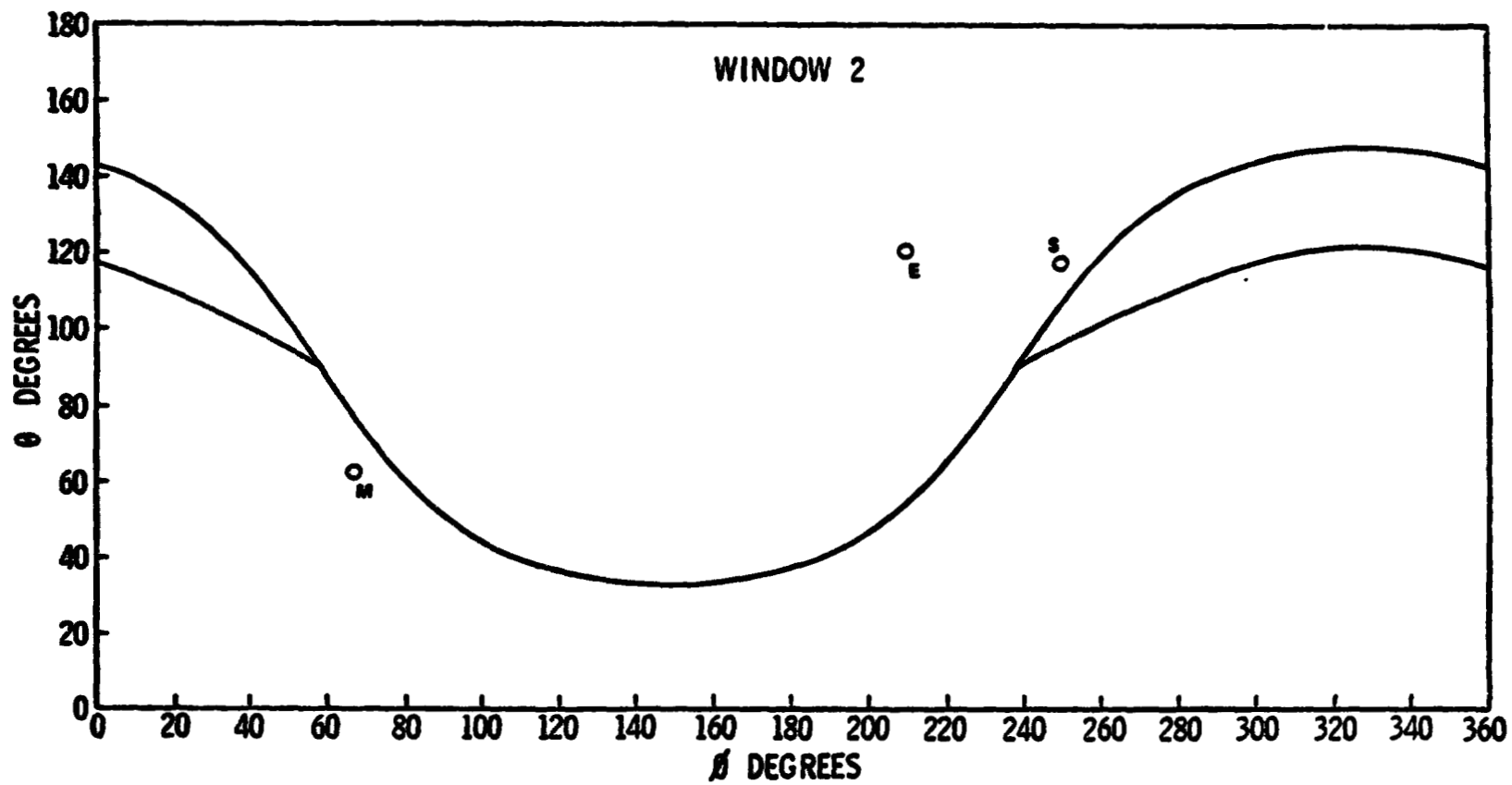


Figure 5. θ , ϕ angles of earth, moon, and sun in postdump attitude, window 2.

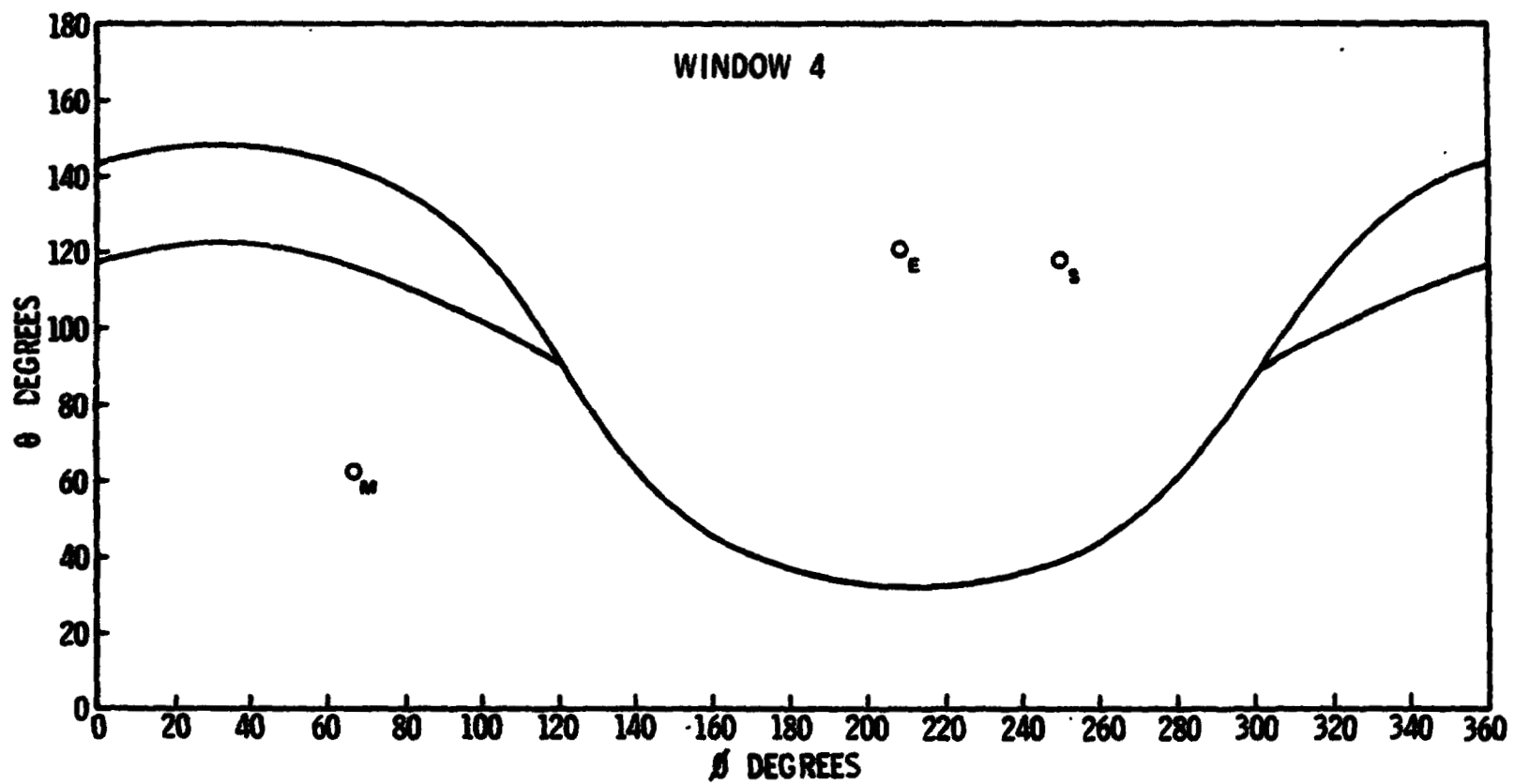


Figure 6. θ , ϕ angles of earth, moon, and sun in postdump attitude, window 4.

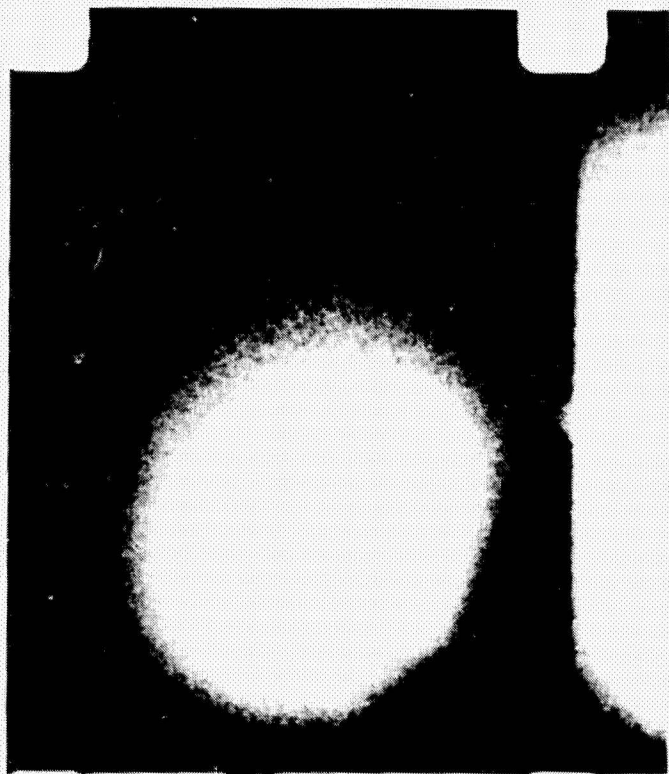
**TABLE 4. ANGLES OF INCIDENCE FOR MOONLIGHT
ON APOLLO 16 WINDOWS**

Window	Moon Angle (deg)	Test Objective	Incident Angle for Moonlight (deg)
4	60.0	Phase Function	34.1
3	119.0	Particle Dynamics (Dump)	60.5
2	62.0	Particle Dynamics (Postdump)	70.6
4	62.0	Particle Dynamics (Postdump)	39.1

Since sunlight is close to being incident on the window opening (Fig. 5), it may be reflecting from some portion of the spacecraft into CM window 2. The angle of incidence to the sun is greater than 90 deg, and 10^{-12} B \odot seems low for a single reflection from any part of the CM. Therefore, although possible, this explanation seems unlikely.

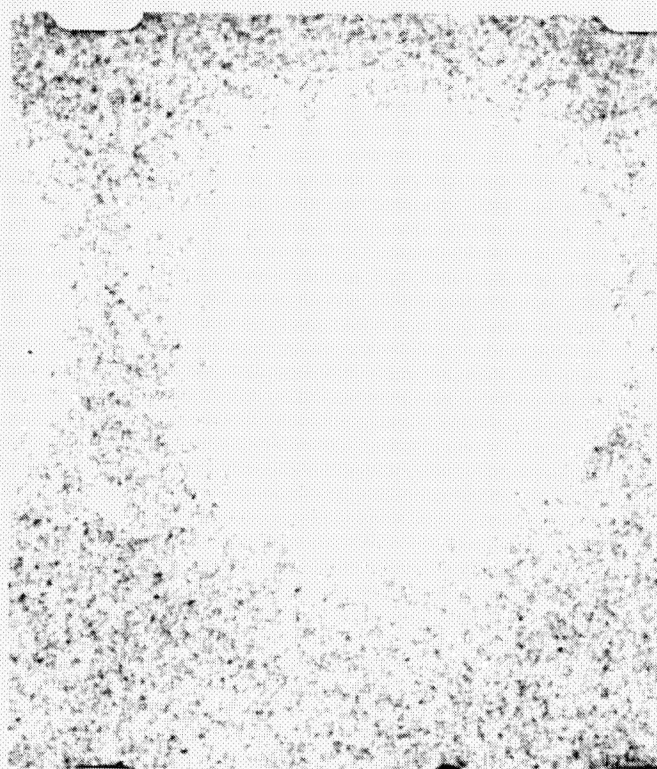
A more likely explanation for the difference can be found using the fact that the bright spot on the film is not in the same position in the photographs taken through each window. (Compare Figure 7 to Figure 8 and Figure 9 to Figure 10.) The cameras are oriented the same in each window but look through different portions of them. That is, the camera in CM 2 looks close to the left edge of the window, and, with the 18-mm lens, the edge of the window or window opening is in the field of view; in CM 4, the camera looks close to the right edge of the window, but the edge is not in the field of view.

Since the moon is incident from the right, the left edge of both windows and window openings is directly illuminated. Hence, the light in CM 2 is probably moonlight plus glare directly from the edge of the window or the window opening. The light in CM 4 is moonlight plus multiply reflected light from the left side of the window.



82

Figure 7. 1-sec exposure through window 2 in first postdump performance.



11d

Figure 8. 1-sec exposure through window 4 in first postdump performance (taken at same time as photograph in Figure 7).

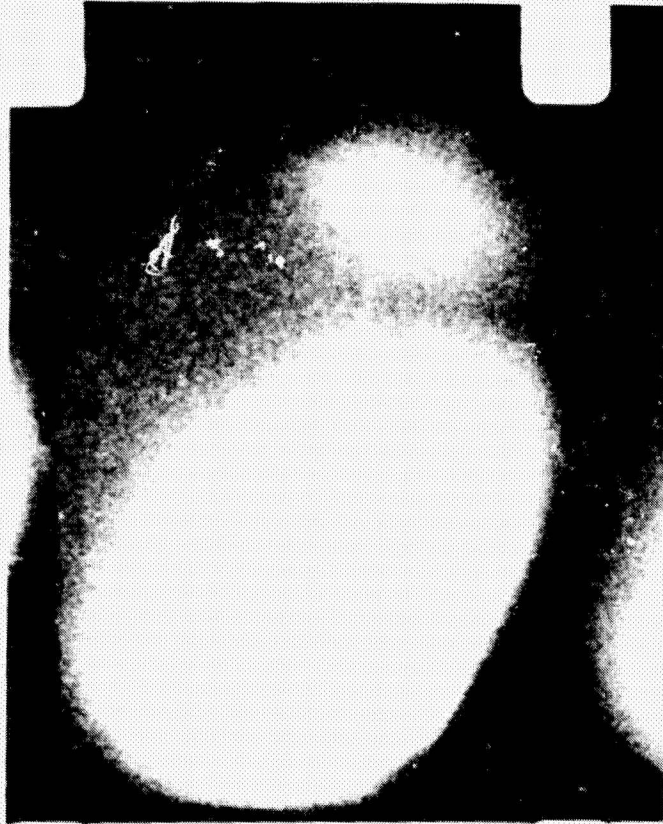


Figure 9. 1-sec exposure through window 2
in last postdump performance.

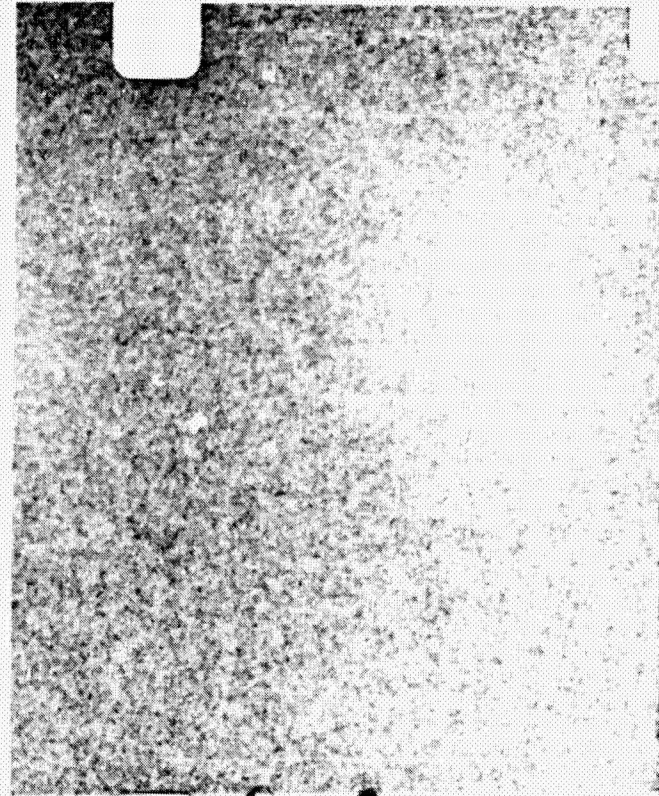


Figure 10. 1-sec exposure through window 4
in last postdump performance (taken at
same time as photograph in Figure 9).

The window opening could be the source of light even though it is painted black. Black paint with an absorptance of 0.9 [3] could cause the brightness seen in CM 2 if the window has a scattering efficiency of 0.04. This is an acceptable value for a dirty window [2].

CALIBRATION OF FILM

A calibrated step wedge was put on the film by the Apollo Photographic Team. Calibration was placed on the 16-mm magazines MM and HH. None was put on the 35-mm magazine X although it was placed on the film in the other 35-mm magazines. All calibration was in accordance with the appropriate specifications [4, 5]. Calibration was put on the film both preflight and postflight. The conversion from exposure on the film E_{film} to the ratio of the surface brightness B to that of the sun B_{\odot} is given by

$$B/B_{\odot} = \frac{4f^2}{T \cdot 2.02 \times 10^9 t} E_{\text{film}}$$

where f is the f number setting, T is the lens and window transmission, and t is the exposure time. In the following discussion, T is assumed equal to 0.75.

It appears that the preflight sensitometric exposures on the film in magazine MM were out of focus. For this reason, only the postflight exposures were used to define the calibration of the 16-mm film. Figure 11 is a plot of the brightness-versus-density curve found from this calibration with the microdensitometer readings. The exposures at 1 sec were used because this is the exposure time for which the most information can be obtained from the experiment exposures.

Figure 12 is a plot of brightness versus density for the 2485 film. These data were not obtained from flight film. However, the film was pre-fogged to a density comparable to the radiation plus fog density on the flight film. Sensitometric data were then placed on the film and the film processed in the same manner as the flight film. Data for the 1-sec exposures are given.

The plots in Figures 11 and 12 curve in opposite directions. Densities in Figure 11 are near the shoulder of the density-log exposure (D -log E) curve, while in Figure 12 they are near the toe of the curve. Figure 13 is the brightness density curve for the 70-mm film in magazine TT. An exposure time of

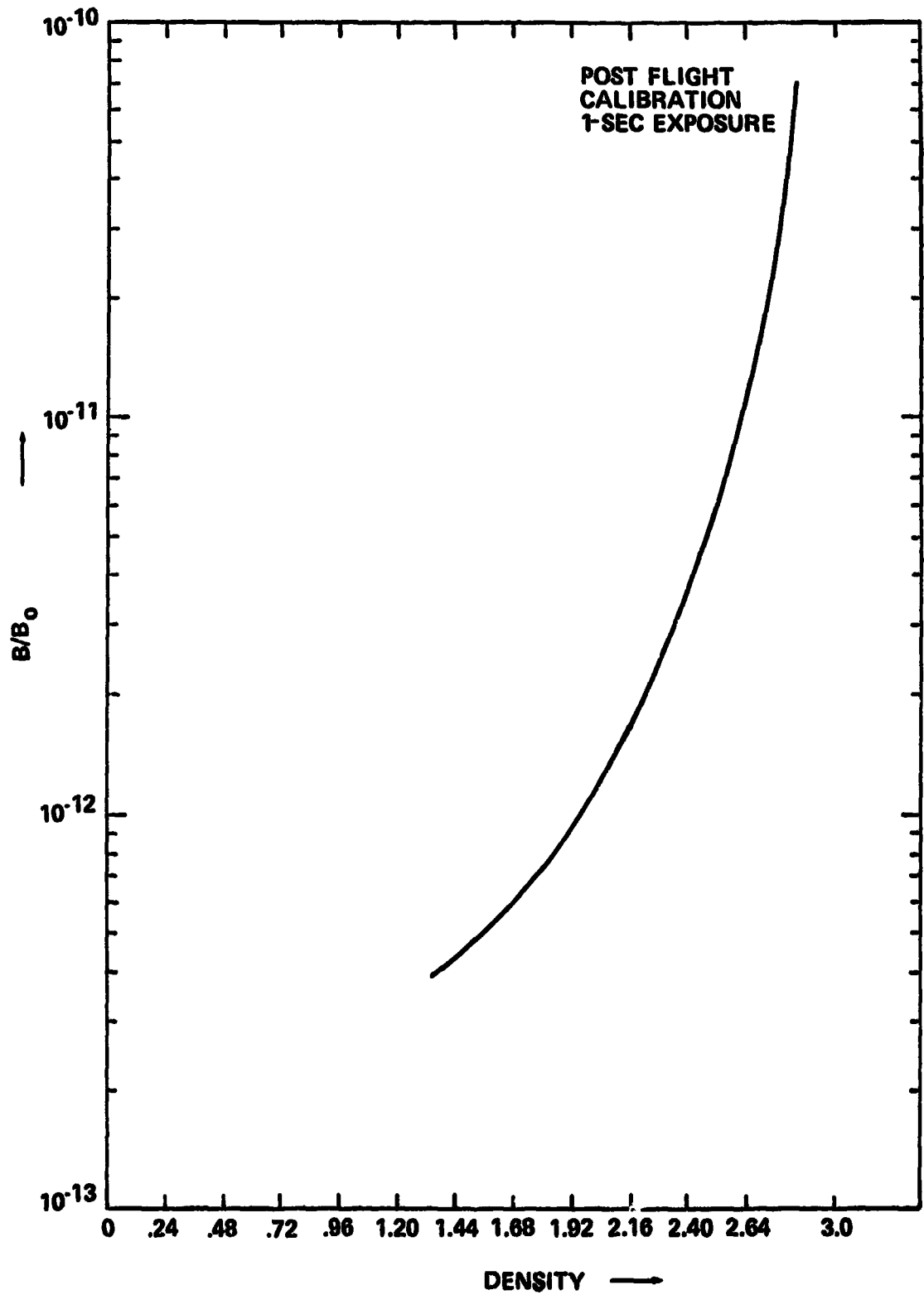


Figure 11. Calibration of 16-mm film, 1-sec exposure time; density read on microdensitometer.

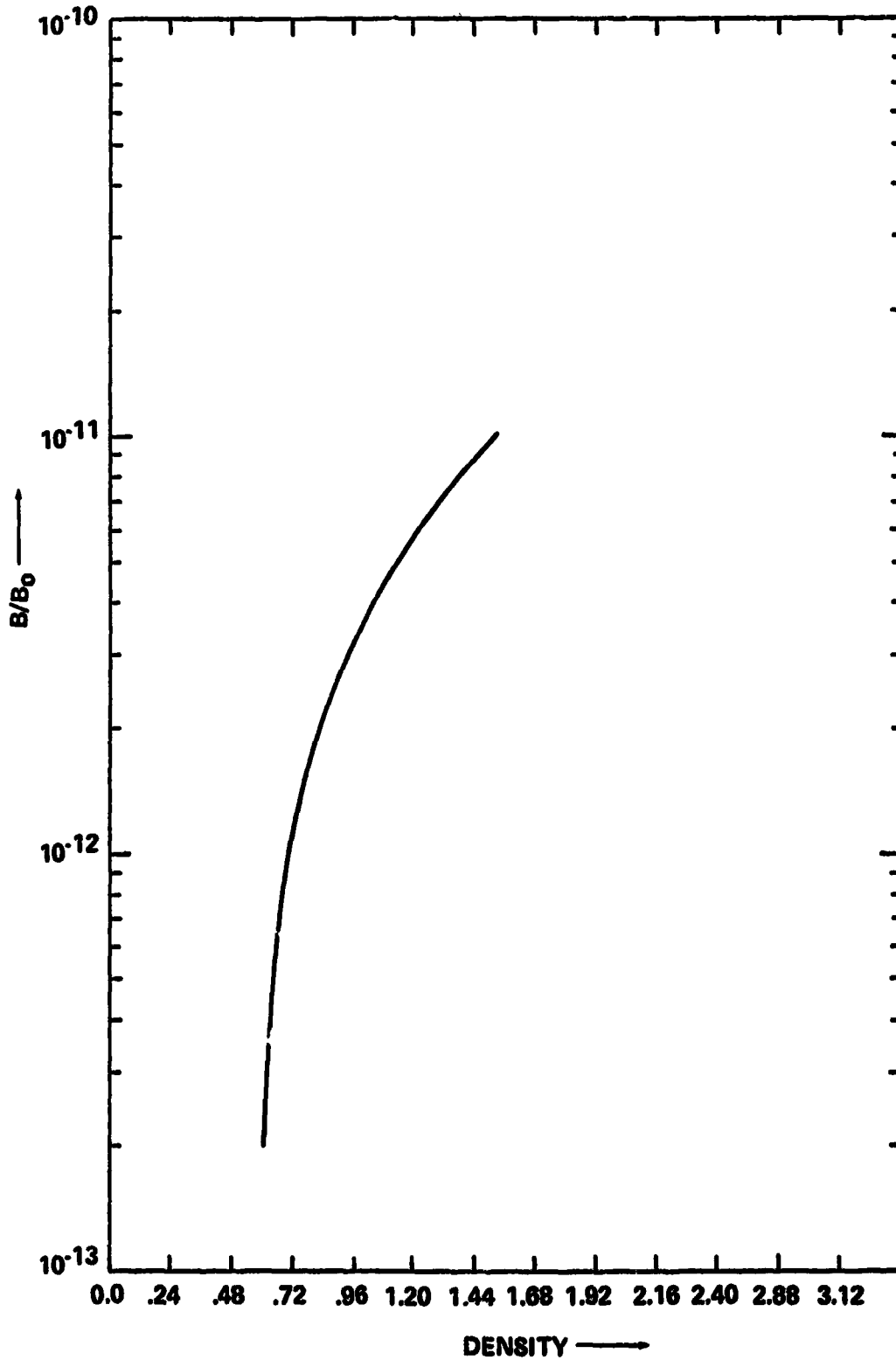


Figure 12. B/B_0 versus density for 1-sec exposure on 2485 film; film pre-exposed before sensitometric data put on; density read on MacBeth densitometer.

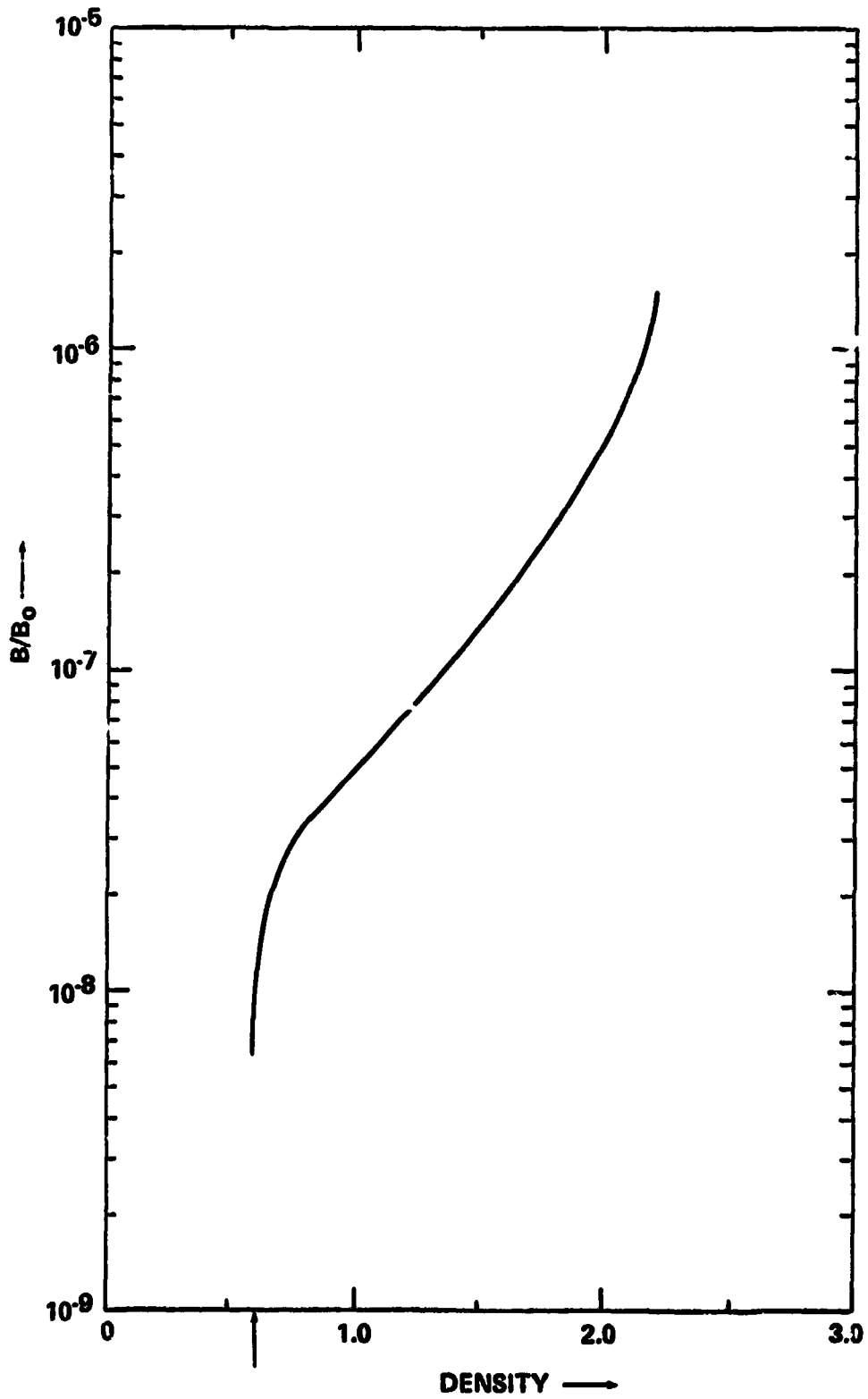


Figure 13. Calibration for 70-mm 2485 film; B/B_0 calculated using $f/16$ and $1/125$ -sec exposure time (arrow marks base fog).

1/125 sec and an f number of 16 were used to find the curve. Postflight sensitometric data were used to obtain the curve. Densities in these figures cannot be directly compared, since the density is specular in Figure 11 and diffuse in Figures 12 and 13. The specular densities were read on a microdensitometer with a 100- μ m square aperture. All diffuse densities were read on a MacBeth densitometer with a 2-mm square aperture.

DATA DESCRIPTION

Density data obtained from selected frames were placed on magnetic tape. A copy of the tape is in the National Space Sciences Data Center (NSSDC). Unfortunately, no calibration frames were available for the 35-mm film when the density readings were taken. Hence, no absolute brightness levels for the 35-mm film can be found from the density readings on the magnetic tape. The calibration was on magazine MM of the 16-mm film. Although calibration frames were on magazine HH, they were not available when the density readings were made. All frames of the 35-mm film were scanned. Frames of the 16-mm film scanned were chosen for the probability of containing good data or representative data. Table 5 lists the frames scanned. The frame numbers of the 16-mm film were arbitrarily assigned. Table 6 lists the file numbers of simultaneous photographs. All of the original flight film has been returned to the Johnson Space Center (JSC) for storage.

A Photometric Data Systems Corporation microdensitometer system consisting of a Model 1010A microdensitometer, a Model 2100A magnetic tape system, and a Model 3100A computer control system was used to take all the data.

The variable parameters as they were used for the scanning were

Scan speed	24 mm/sec
Objective	10X, 0.25 NA
Eyepiece	5X
Physical aperture	5 x 5 mm
Effective aperture	100 x 100 μ m

An edge scan was made. In each record, the data in each record start at the same x coordinate (F). The step in x and y is 100 μ m long.

TABLE 5. IDENTIFICATION OF FILES ON MAGNETIC TAPE (MAGAZINES MM AND HH ARE 16 mm, MAGAZINE X IS 35 mm, AND MAGAZINE TT IS 70 mm)

File Number	Magazine Identification	Exposure Time (sec)	Frame Number	Preflight Calibration	Postflight Calibration	Number of Records	Number of Words Per Record ^a
1	MM	5	C1	x		83	35
2	↓	↓	C2	x		81	↓
3	↓	↓	C3	x		↓	↓
4	↓	↓	C4	x		↓	↓
5	↓	↓	C5	x		↓	↓
6	↓	5	C6	x		↓	↓
7	↓	1	C25	x		↓	↓
8	↓	↓	C27	x		↓	↓
9	↓	↓	C28	x		↓	↓
10	↓	↓	C29	x		↓	↓
11	↓	↓	C30	x		↓	↓
12	↓	1	C31	x		↓	↓
13	↓	1/1000	C56	x		↓	↓
14	↓	↓	C57	x		↓	↓
15	↓	↓	C58	x		↓	↓
16	↓	↓	C59	x		↓	↓
17	↓	↓	C60	x		↓	↓
18	↓	1/1000	C61	x		81	35
19	↓	1/60	41			105	27
20	↓	↓	42			↓	↓
21	↓	↓	77			↓	↓
22	MM	1/60	78			105	27

TABLE 5. (Continued)

File Number	Magazine Identification	Exposure Time (sec)	Frame Number	Preflight Calibration	Postflight Calibration	Number of Records	Number of Words per Record ^a
23	MM	1/60	pre 81			105	27
24	↓	5	84			↓	↓
25	↓	-	bad file			↓	↓
26	↓	1	85			↓	↓
27	↓	↓	86			↓	↓
28	↓	1	87			↓	↓
29	↓	1/60	88			↓	↓
30	↓	1/1000	92			↓	↓
31	↓	5	95			↓	↓
32	↓	1	96			↓	↓
33	↓	↓	97			105	↓
34	↓	↓	bad file			67	↓
35	↓	1	98			105	↓
36	↓	1/60	99			↓	↓
37	↓	1/1000	103			↓	↓
38	↓	10	106			↓	↓
39	↓	5	108			↓	↓
40	↓	1	110			↓	↓
41	↓	↓	111			↓	↓
42	↓	1	112			↓	↓
43	↓	?	113			↓	↓
44	↓	1/1000	114			105	27
45	MM	10	C101		x	11	35

TABLE 5. (Continued)

File Number	Magazine Identification	Exposure Time (sec)	Frame Number	Preflight Calibration	Postflight Calibration	Number of Records	Number of Words per Record ^a
46	MM ↓	10	C102		x	11 ↓	35 ↓
47			C103		x		
48			C104		x		
49			C105		x		
50		10	C106		x		
51		5	C107		x		
52			C108		x		
53			C109		x		
54			C110		x		
55			C111		x		
56		5	C112		x		
57		1	C133		x		
58			C134		x		
59			C135		x		
60			C136		x		
61			C139		x		
62		1	C140		x		
63		1/60	C141		x		
64			C142		x		
65			C143		x		
66		C144		x			
67		C145		x	11	35	
68	MM	1/60	C146		x		

TABLE 5. (Continued)

File Number	Magazine Identification	Exposure Time (sec)	Frame Number	Preflight Calibration	Postflight Calibration	Number of Records	Number of Words per Record ^a
69	MM	1/1000	C166		x	11	35
70	↓	↓	C167		x	↓	↓
71	↓	↓	C168		x	↓	↓
72	↓	↓	C169		x	↓	↓
73	↓	↓	C170		x	↓	↓
74	MM	1/1000	C171		x	11	35
75	HH	1/1000	115			105	27
76	↓	5	117			↓	↓
77	↓	1	119			↓	↓
78	↓	↓	120			↓	↓
79	↓	1	121			↓	↓
80	↓	1/60	122			↓	↓
81	↓	1/1000	125			↓	↓
82	↓	5	127			↓	↓
83	↓	1	129			↓	↓
84	↓	↓	130			↓	↓
85	↓	1	131			↓	↓
86	↓	1/60	132			↓	↓
87	↓	1/1000	136			↓	↓
88	↓	10	138			↓	↓
89	↓	5	140			↓	↓
90	↓	↓	141			↓	↓
91	↓	5	142			↓	↓
92	HH	1	143			105	27

TABLE 5. (Concluded)

File Number	Magazine Identification	Exposure Time (sec)	Frame Number	Preflight Calibration	Postflight Calibration	Number of Records	Number of Words per Record ^a
93	HH	1	144			105	27
94	HH	1	145			105	27
95	X	100	seq 1			255	127
96	↓	10	↓			↓	↓
97		1	↓				
98		1/8	seq 1				
99		100	seq 2				
100		10	↓				
101		1	↓				
102		1/8	seq 2				
103		100	seq 3				
104		10	↓				
105		1	↓				
106	1/8	seq 3					
107	100	seq 4					
108	10	↓					
109	1	↓					
110	X	1/8	seq 4			255	127

a. These are 36-bit words and include 16 words of record identification.

TABLE 6. FILE NUMBERS FOR SIMULTANEOUS FRAMES OF POSTDUMP

File Number Mag MM	File Number Mag HH	Exposure Time (sec)
26	77	1
27	78	1
28	79	1
32	83	1
33	84	1
35	85	1
38	88	10
39	90	5
40	92	1
41	93	1
42	94	1
36	86	1/60
29	80	1/60

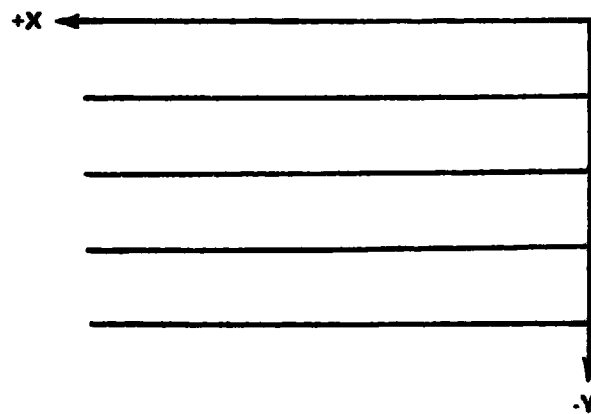


Figure 14. Edge scan.

All data were recorded on 9-track tape but have been converted to 7-track tape at 800 bpi. Record identification and data are as described in the next section. Each complete photograph is a file, and each scan is a record. Record lengths within a file are the same but do vary between files, as do the number of records per file. The first file is 83 records long, but the last three records are duplicates of each other. Table 5 lists the number of records for each file and the number of 36-bit words per record.

The data were recorded on a 7-channel tape at 300 bpi and with odd parity. Each tape character has been recorded to represent six binary bits of information.

The contents of each data record are as follows:

1. Two characters representing the octal number 7777. These are used to designate the beginning of a record and are not part of the program data.

2. Eighty characters representing forty 12-bit words of sample identification information. Each pair of characters contains the ASCII code for one identification word; e.g., the two tape characters (000011) (000001) would produce the octal number 0301, which is the ASCII code for the letter A.

3. Two characters representing the octal value for minus the number of data values following the coordinate information in the record. Each data value will be comprised of two tape characters, making one 12-bit word; e.g., the two tape characters (110000) (000000) = $6000_8 = -2000_8$ would indicate that there are 2000_8 data values following the coordinate information in this record.

4. Four characters representing a 24-bit binary number which is the x coordinate on the sample (in micrometers) where data taking begins for the current data record. The most significant bit is a sign bit.

If the sign bit is the number one, the coordinate value represented has a negative value. The binary absolute value of the coordinate, in this case, is found by two's complementing the 24-digit number and incrementing the result by one; e.g., the tape characters (000000) (000010) (011100) (010000) represent the coordinate $+00023420_8 = +10000_{10} \mu\text{m}$. The tape characters (111111) (111101) (100011) (110000) represent the coordinate $-00023420_8 = -10000_{10} \mu\text{m}$.

5. Four characters representing a 24-bit binary number which is the y coordinate on the sample (in micrometers) where data taking begins for the current data record. The interpretation is the same as explained previously for the x coordinate.

6. Four characters representing a 24-bit binary number which is the x distance (in micrometers) between density readings. The interpretation is the same as explained for the x and y coordinates.

The y coordinate where this record begins is

$$(7777)(1434)_8 = -00006344_8 = -3300_{10} \mu\text{m} .$$

Figure 14, which shows the geometry of the edge scan, also shows why the y coordinate is negative.

Density readings in x were taken at a distance apart equal to

$$(0000)(0144)_8 = 100_{10} \mu\text{m} .$$

The first data value is

$$0434_8 = 284_{10} ,$$

which corresponds to a density of

$$\frac{284}{400} = 0.710 .$$

All other density values are found in a similar manner.

DATA RESULTS

Phase Function

The total exposure on the film is due to energetic radiation, integrated star light, zodiacal light and other sources, including light scattered by the window. The total integrated starlight and zodiacal light are known, so the energetic radiation can be found by using unexposed portions of the film. Therefore, the exposure due to scattering by a residual cloud of contamination can be found by subtraction if there are no sources of extraneous light. If other light sources are present whose magnitudes are unknown, then obviously the subtraction process cannot isolate the effects of the residual cloud. This is the case with the phase function photography. The intensity due to moonlight cannot be factored out since the amount of scattering by the window is unknown.

Density readings taken from the middle of each frame of 1-sec exposure time show that the total background brightness is on the order of $10^{-12} B/B_{\odot}$ for the photographs looking down the $+x$ axis. For the photographs looking up

30 deg from the +x axis, slightly lower background levels were recorded. Table 7 lists the total range of brightness recorded for each 1-sec exposure. The sky brightness at the locations of the +x axis is given in Table 8. Background brightness from the film is an order of magnitude higher than the sky background.

The effects of the scattered moonlight on CM window 4 can be seen in Figures 16 through 18. These are three of the four photographs taken in the first set of exposures. Exposure times are 1/8, 1, and 10 sec respectively. The extent of the scattered moonlight increases with increasing exposure, indicating that the window is completely covered by moonlight. Both Venus and Mars are in the photographs. Venus is the very bright image near the center of all three figures. Mars is almost directly under Venus. When the photograph was taken, Venus and Mars had magnitudes of -4.2 and 1.8, respectively. The lowest magnitude star seen in the figures is sixth.

TABLE 7. RANGE OF BRIGHTNESS FROM 1-sec EXPOSURES ON 35-mm FILM

Angle of Sun from x Axis (deg)	Range of Brightness (B/B _☉)
43	$5-9 \times 10^{-12}$
73	$\approx 10^{-13}$ (In Gross Fog of Film)
120	$4-9 \times 10^{-12}$
150	Less than 3×10^{-12}

Since the amount of scattering by the window was not known and since a good calibration was not available, this effort was pursued no further.

Particle Dynamics

Figure 19 is a collection, to relative scale, of densities and lengths of all the possible particle tracks seen in the 16-mm film. It is not known if any of these tracks were caused by energetic radiation. No identifiable individual particles are seen in any of the postdump photographs.

TABLE 8. SKY BACKGROUND IN B/B ⊙ AT PHASE FUNCTION POSITIONS [6, 7, 8]

Angle of Sun From x Axis (deg)	Zodiacal Light	Integrated Starlight
43	4.1×10^{-13}	6.8×10^{-14}
73	1.6×10^{-13}	1.8×10^{-14}
120	5×10^{-14a}	1.0×10^{-13}
150	5×10^{-14a}	9.8×10^{-14}

a. These values obtained by assuming zodiacal light is symmetric about the ecliptic and using values found in Reference 5.

The number of particles seen on Apollo 16 versus the number seen on other Apollo missions for liquid waste dumps is less for several reasons. Less water was dumped for S226 than normally is dumped for urine or waste water. Also, the dump nozzle was one not previously used, therefore, no frost was on it; and the lines to the nozzle were such that the entire length was subject only to cabin atmosphere. Lastly, the geometries for viewing are different.

The tracks were filmed during the maneuver from the dump to the post-dump attitude. Because the camera was focused at infinity, the distance of the particle from the spacecraft cannot easily be found. Therefore, efforts to use the film to study particle dynamics were terminated.

A theoretical analysis of particle trajectories was established early in the study. This analysis is included as an appendix. Stellar camera photographs with particles in them are analyzed in the appendix for possible sources. No plausible source was found. It should be noted that although many stellar camera frames from Apollo 15 had particles in them, very few particles were seen in the stellar camera frames from Apollo 16 and 17. There is no known explanation at this time for this difference.

REPRODUCIBILITY OF THE ORIGINAL PAGE IS POOR,

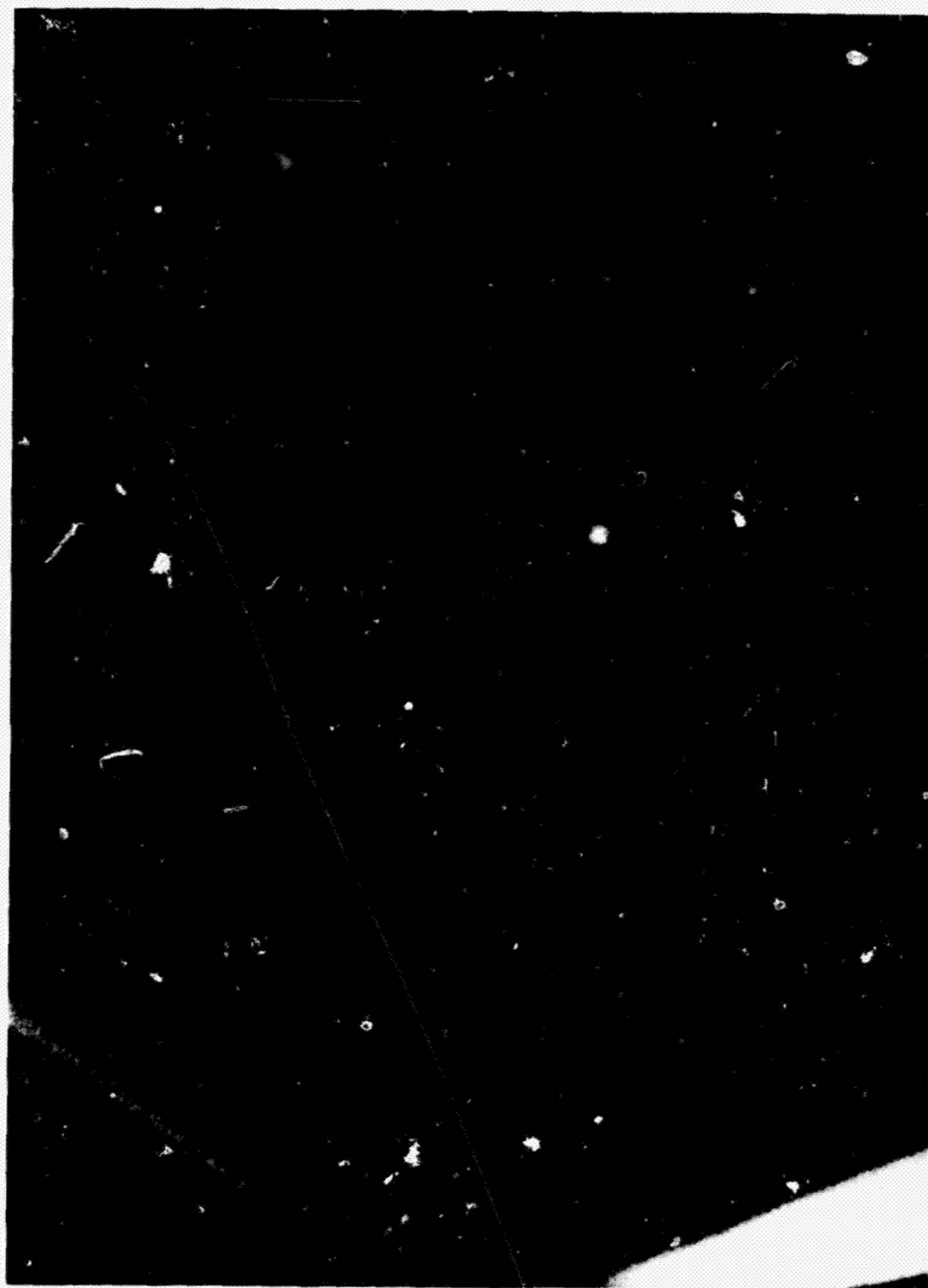


Figure 16. First phase function performance. 1/8-sec exposure.

REPRODUCIBILITY OF THE ORIGINAL PAGE IS POOR,



Figure 17. First phase function performance, 1-sec exposure.

REPRODUCIBILITY OF THE ORIGINAL PAGE IS POOR,

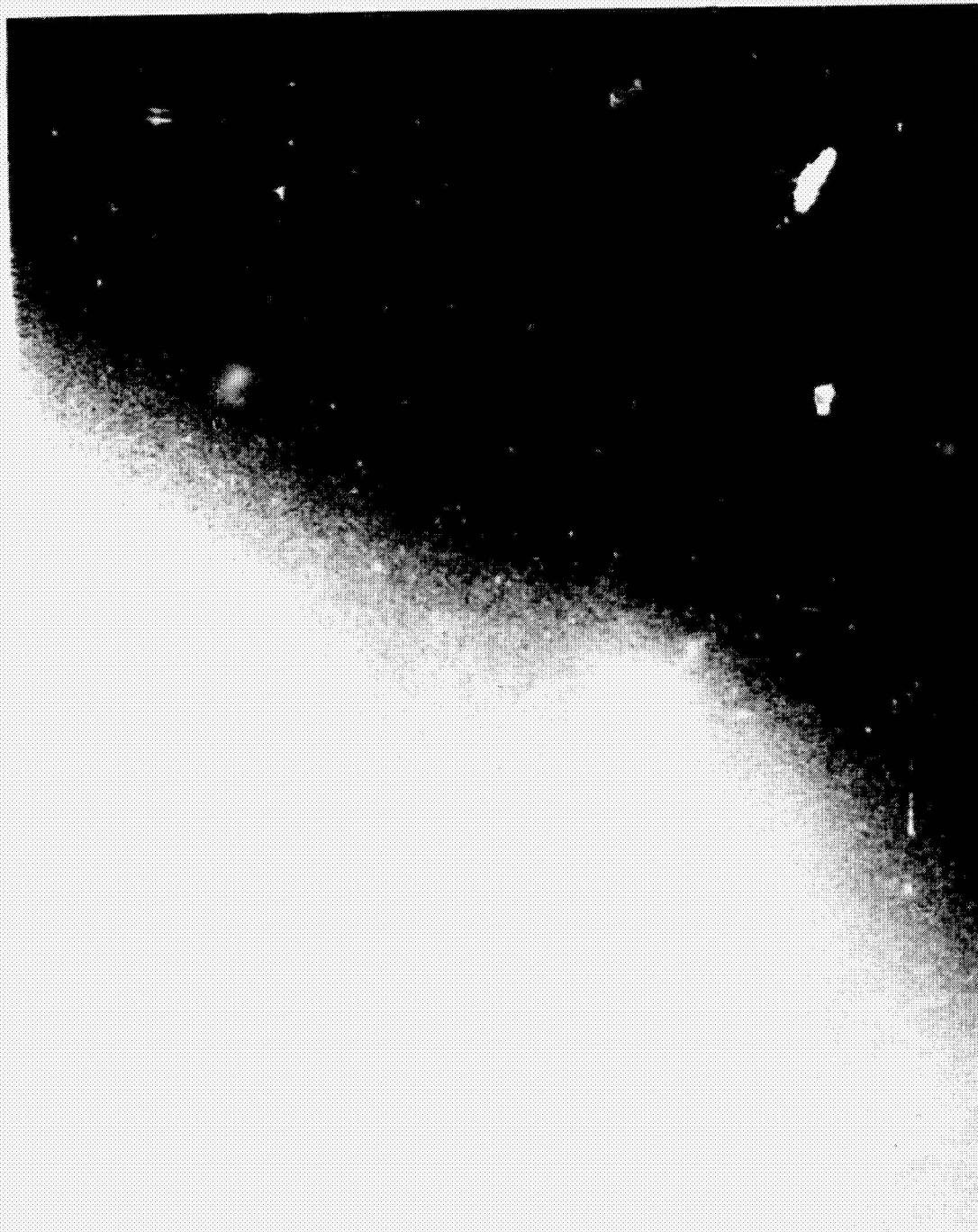


Figure 18. First phase function performance, 10-sec exposure.

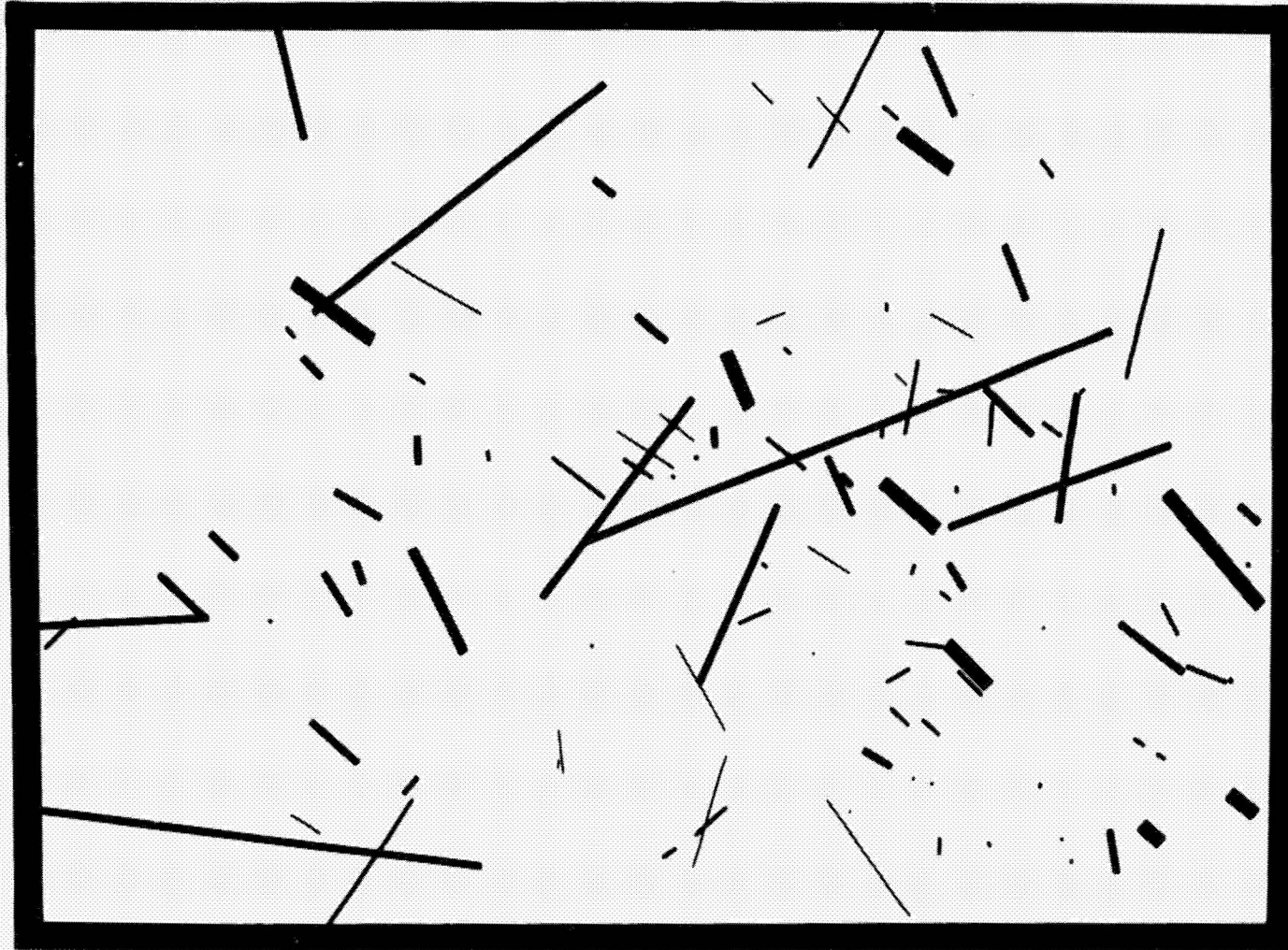


Figure 19. Trace of all identifiable particle tracks; tracks are as seen from CM 2.

Decay of Background Brightness

The time decay of the background brightness due to a dump can be found by examining the total background brightness as a function of time. If the spacecraft attitude does not change during the experiment, the only source that is changing is that due to the dump. Hence, the decay is caused by the expansion and recession of the dumped material.

Figure 20 is a chart of the θ , ϕ angles to the sun during the performance of S226. The angles were recorded from real time displays on control consoles at Mission Control Center. As can be seen, the attitude of the spacecraft did not change by more than 2 deg during the postdump photography. This should cause little change in the amount of scattered moonlight (Fig. 5) and sources other than the dump material.

Mag HH was used to find the time decay. Density readings were taken from one of the three 1-sec exposures for each performance of the postdump photography. Exposures were made 7, 12, and 22 minutes after the end of the dump.

Six density readings were made on each frame — two at the top, two in the middle, and two at the bottom. All readings were made using the MacBeth densitometer at JSC. The points are plotted in Figure 21. The agreement between the decay found here and the fitted curve found by Naumann [2] is surprisingly good. However, there is some difference in the experiment. In the S226 experiment, the dump nozzle was clean and all lines to the nozzle were in a warm environment. Thus, no freezing in the lines took place so that there was no additional material leaking off after the dump ended. Hence the decay given here is not encumbered by repeated increases in the background brightness. Also, the cameras were looking through the cloud in the direction of the dump on Apollo 16, whereas on Apollo 15 they were looking obliquely through the cloud.

Plume Structure

Of the seven 70-mm photographs taken, three recorded the dump plume. Figures 22, 23, and 24 are these photographs as taken; i. e., Figure 22 was taken first, Figure 24 last. The frames were exposed in rapid sequence, one after the other. It was felt that because of the juxtaposition of the nozzle and the window, the hatch window (CM window 3) would frost over. However, the window remained clear throughout the dump.

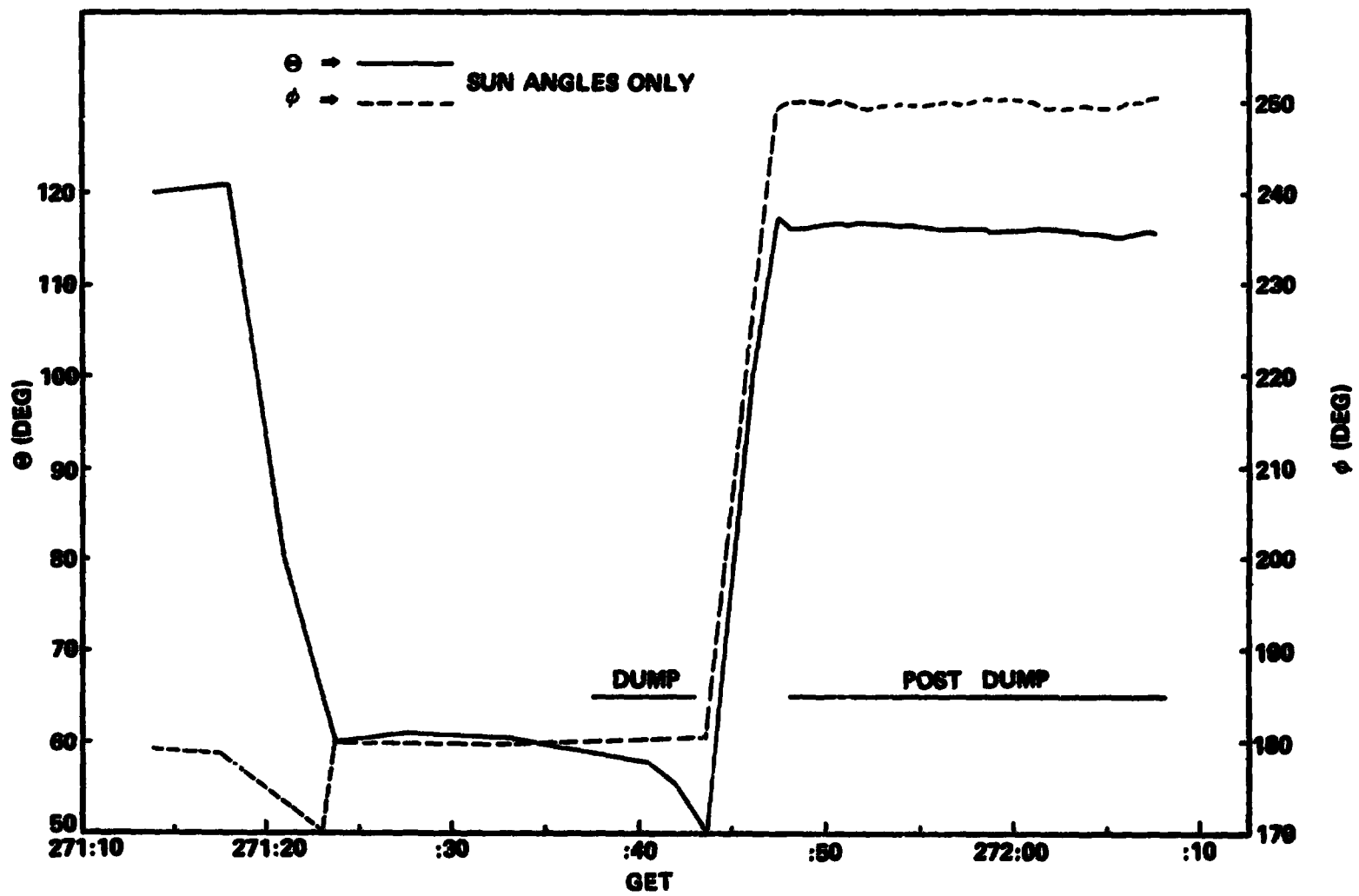


Figure 20. Orientation of CSM with respect to sun during S226 dump and postdump performance.

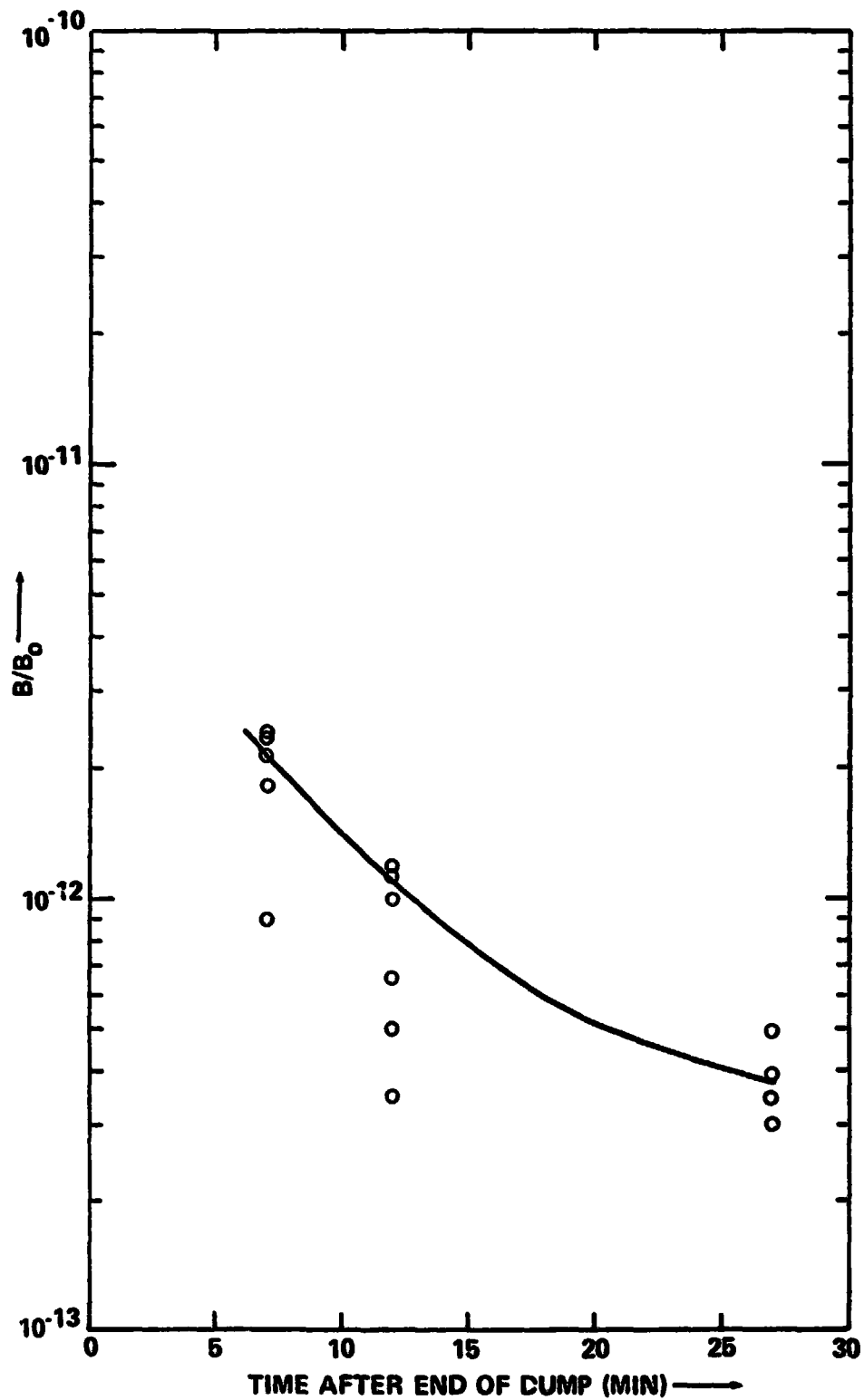


Figure 21. Decay of background brightness (circles denote spread of density readings; curve drawn through data obtained from center of frame).

REPRODUCIBILITY OF THE ORIGINAL PAGE IS POOR,

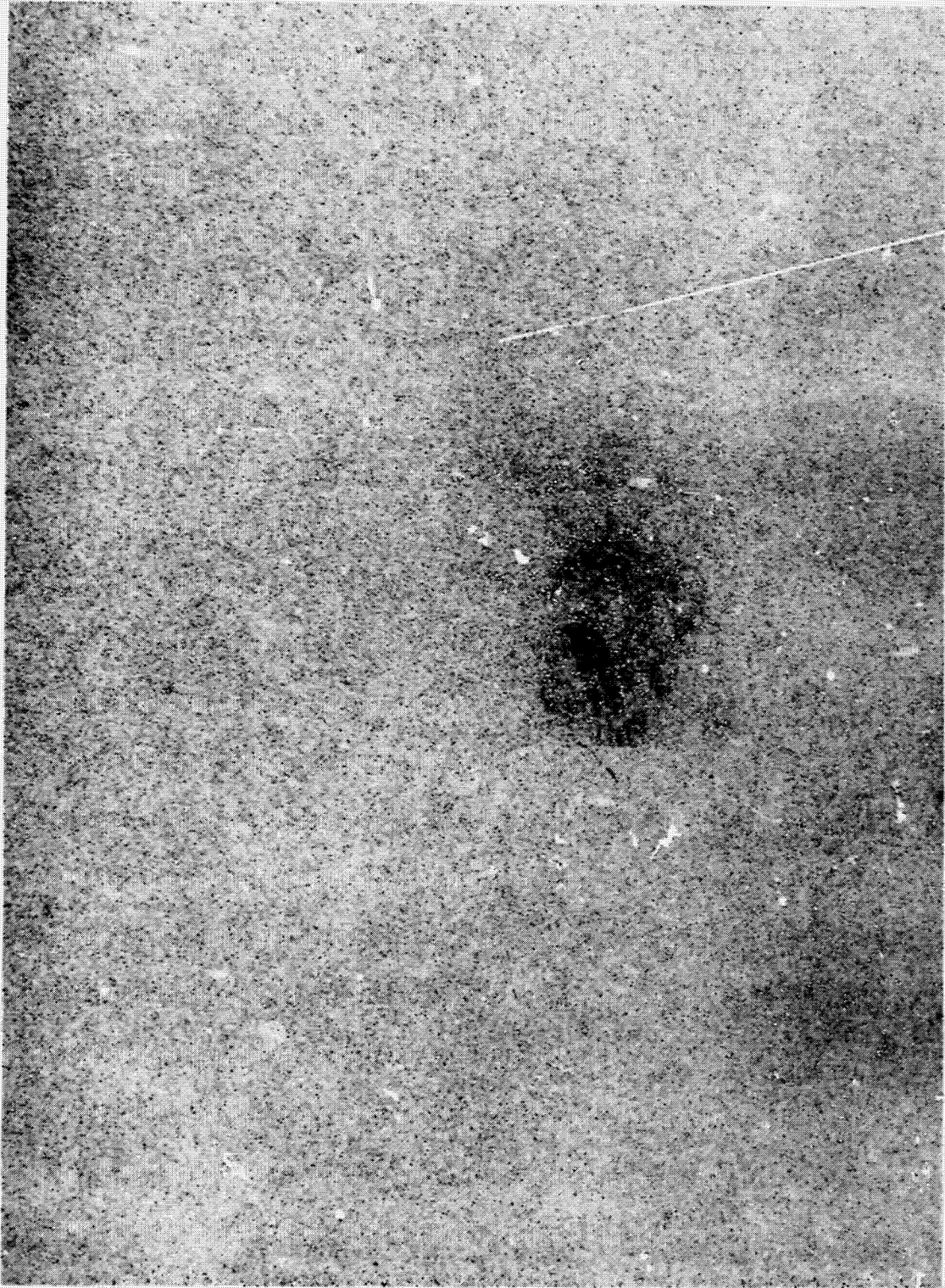


Figure 22. First 70-mm frame showing particles from water dump.

REPRODUCIBILITY OF THE ORIGINAL PAGE IS POOR,

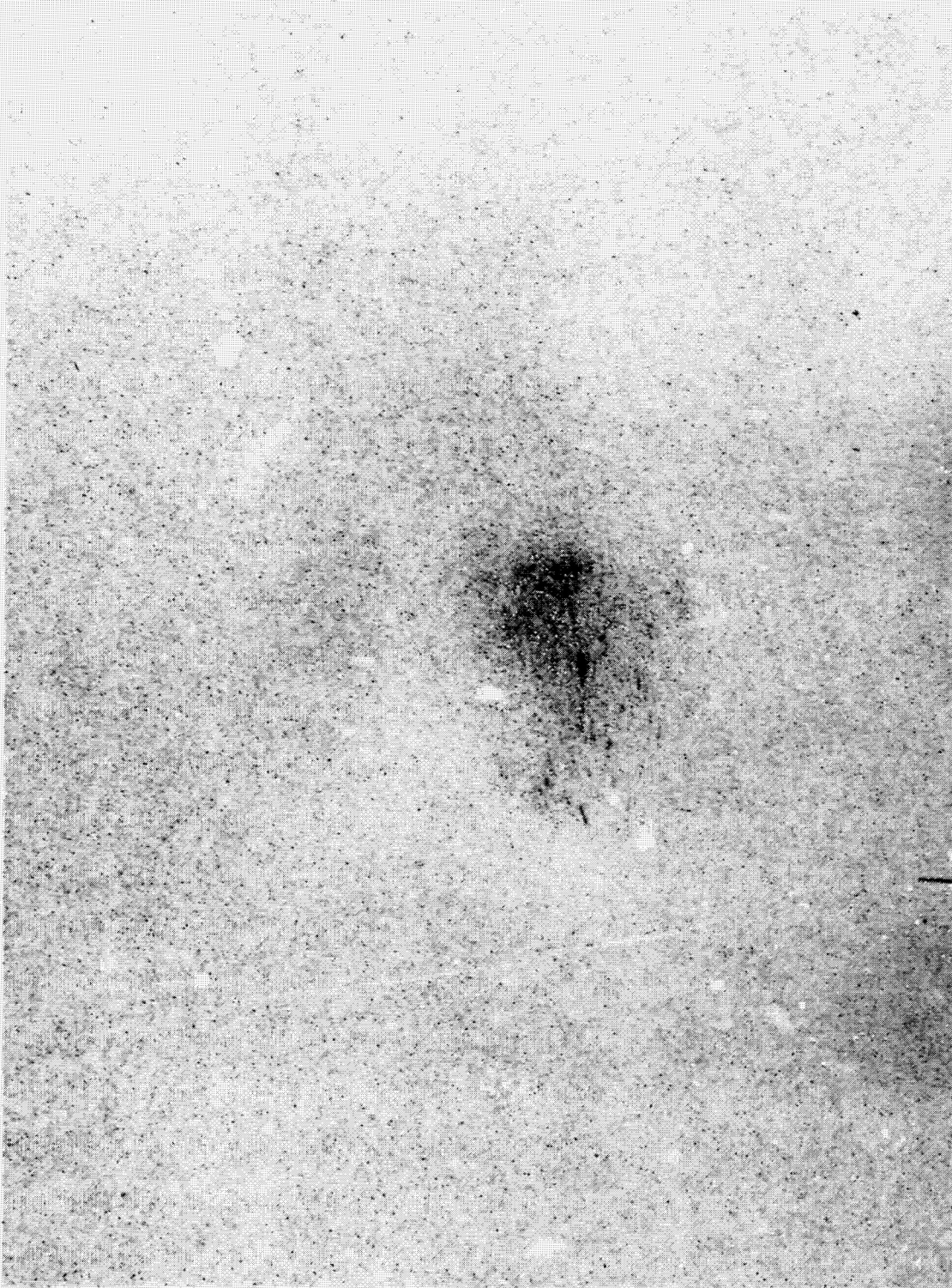


Figure 23. Second 70-mm frame showing particles from water dump.

REPRODUCIBILITY OF THE ORIGINAL PAGE IS POOR,



Figure 24. Last 70-mm frame showing particles from water dump.

The half-angle of the dump cone as seen in the 70-mm film is 17.5 deg. If the HEC was held perpendicular to the hatch window, as required in the crew procedures, 17.5 deg would correspond to a dump cone half-angle of from 3 to 4 deg (this assumes the camera and dump nozzle have the same origin). Although such a narrow angle is consistent with crew observations, it is not consistent with ground-based tests. McPherson [9] reports that in a vacuum chamber the water forms a half-angle of 15 to 20 deg. If the camera were tilted only 22 deg with respect to the dump direction, then 17.5 deg would correspond to a 15-deg half-angle. Since the crew reported they did not hold the camera at any special orientation, no definite conclusion can be made about the half-angle of the dump.

Moonlight on the window obviates obtaining meaningful mass distribution data. Although there are frames of the 70-mm film which do not have particles in them, the HEC was not started until after dump initiation. Since the background brightness in the darker areas of the negative is too high to have been caused by scattered moonlight alone, it must be the result of small unresolvable particles in the dump cone.

APPENDIX

A SPACECRAFT CONTAMINATION PARTICLE TRAJECTORY STUDY

Introduction

This study is an analysis of photographic recorded trajectories of particles emerging from a point source on a spacecraft. The main analysis is based on a program that was developed to generate the perspective projection of particles emerging from a nozzle and viewed by a camera. The study was undertaken to analyze photographs obtained by cameras on the Apollo 15, 16 and 17 missions. This report presents the formulation of the equations used and various results of the study.

Theory

The formulation of the equations of motion, the perspective projections, the film image, and the radiance of the particles are presented in this section.

EQUATION OF MOTION

To define the trajectory or position of a particle, a convenient coordinate system is introduced and then transformed into the camera coordinate system. The development assumes that the particles are emerging from a point at a known location with respect to the camera.

The vector \vec{R}_1 to the origin of the particles, a nozzle, with respect to the spacecraft-mounted camera system is given as follows:

$$\vec{R}_1 = (x_c^1, y_c^1, z_c^1) \quad .$$

The vector \vec{R}_2 from the origin of the particles along the axis of the nozzle to a position normal to the particle with respect to the nozzle axis is given as follows:

$$\vec{R}_2 = (\alpha^2, \beta^2, \gamma^2) \quad .$$

The vector \vec{R}_3 , a normal from the nozzle axis to the particle, is given as follows:

$$\vec{R}_3 = (r^3, s^3, t^3) \quad ,$$

where r^3, s^3, t^3 and $\alpha^2, \beta^2, \gamma^2$ are to be defined in a convenient manner.

The position of the particle from the camera \vec{R} is then given as follows:

$$\vec{R} = \vec{R}_1 + \vec{R}_2 + \vec{R}_3 \quad ,$$

as shown in Figure A-1. The particle coordinate system is in a mixed mode of coordinate variables:

$$\vec{R} = \vec{R}_1 (x_c^1, y_c^1, z_c^1) + \vec{R}_2 (\alpha^2, \beta^2, \gamma^2) + \vec{R}_3 (r^3, s^3, t^3) \quad .$$

Therefore, the vectors \vec{R}_2 and \vec{R}_3 are to be defined and transformed into the camera coordinate system by coordinate transformation matrices.

The camera coordinate system is shown in Figure A-2, where the x_c axis is the optical axis of the camera and $+y_c$ is to the left of the window.

The nozzle axis is assumed to make an angle η with \hat{x}_c (a unit vector along $+x_c$). In defining the α, β, γ coordinates, the α axis is assumed to be collinear with the nozzle axis and the x_c axis is assumed to lie in the $\alpha - \beta$ plane with $\hat{\gamma}$ defined by $(\hat{x}_c) \times (\hat{\alpha})$. Hence, to obtain $\vec{R}_2 = |\vec{R}_2| \hat{\alpha}$ in the camera coordinate system, one first transforms the α, β, γ coordinate system by a rotation of $-\eta$ about the γ axis to obtain \vec{R}_2 in a $(\hat{x}_c, \hat{\beta}, \hat{\gamma})$ coordinate system. The transformation is shown in Figure A-3. This system is transformed into the camera coordinate system by a rotation of $-\nu$ about the x_c axis (Fig. A-4). The angle ν specifies the rotation of a plane which contains the nozzle axis and \hat{x}_c from the $\hat{z}_c - \hat{x}_c$ plane. The coordinates for a nozzle perpendicular to the Apollo Command Service Module (CSM) skinline in

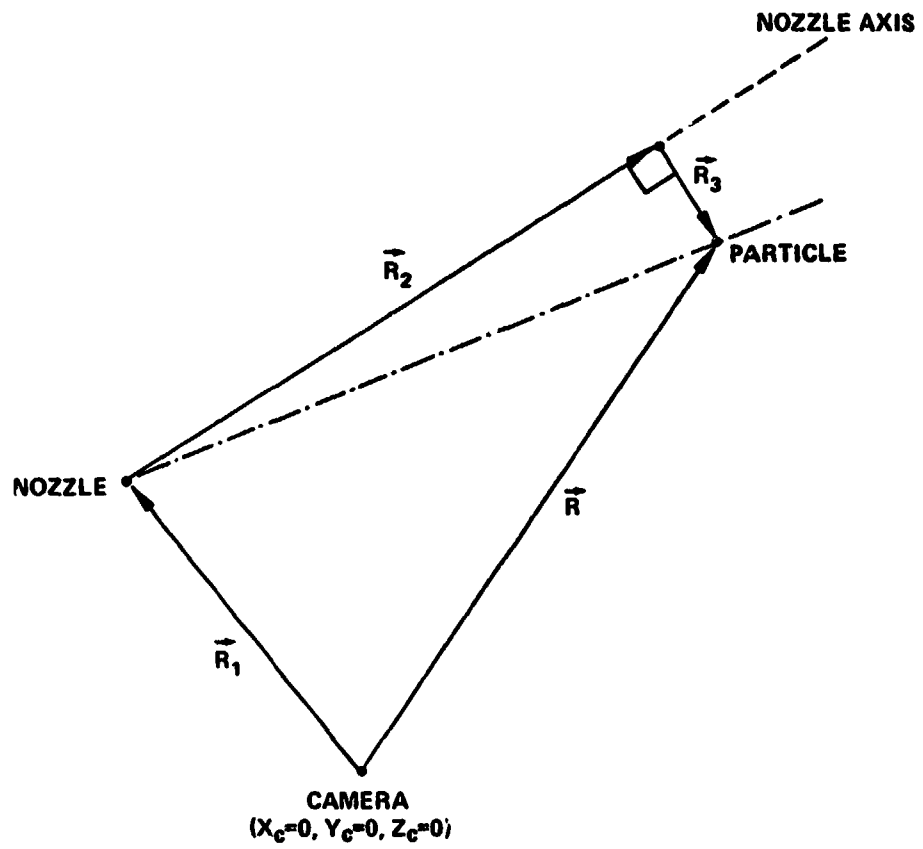


Figure A-1. Particle coordinate system.

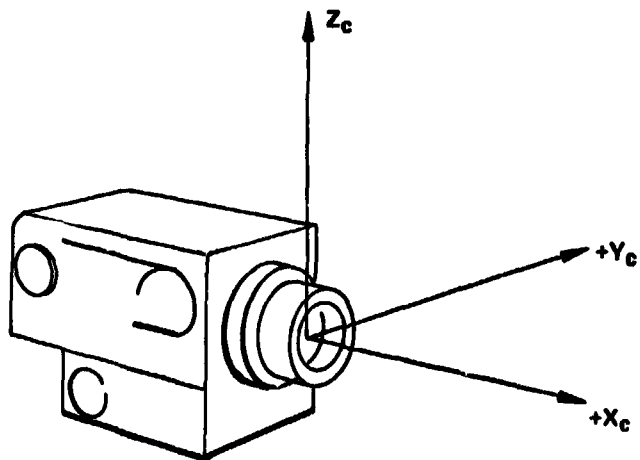


Figure A-2. Camera coordinate system.

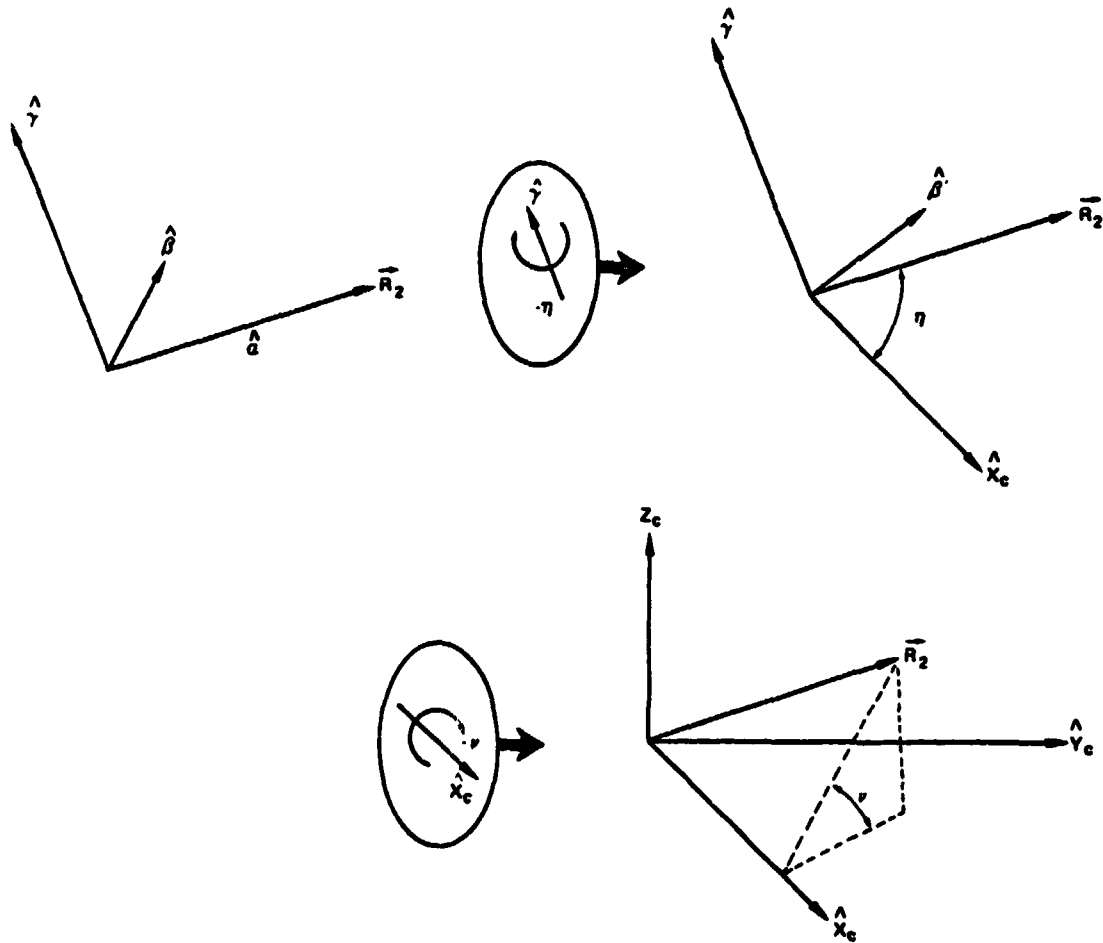


Figure A-3. Transformation of \vec{R}_2 .

the spacecraft center of mass coordinates would specify ν :

$$\nu = \arctan \left(\frac{-y_{cm}^{nozzle}}{-z_{cm}^{nozzle}} \right) .$$

The coordinate transformation matrix equation for \vec{R}_2 is given as follows [10] :

$$\vec{R}_2(x_c, y_c, z_c) = \begin{bmatrix} 1 & 0 & 0 \\ 0 & \cos \nu & -\sin \nu \\ 0 & \sin \nu & \cos \nu \end{bmatrix} \begin{bmatrix} \cos \eta & -\sin \eta & 0 \\ \sin \eta & \cos \eta & 0 \\ 0 & 0 & 1 \end{bmatrix} \begin{bmatrix} |\vec{R}_2| \\ 0 \\ 0 \end{bmatrix}$$

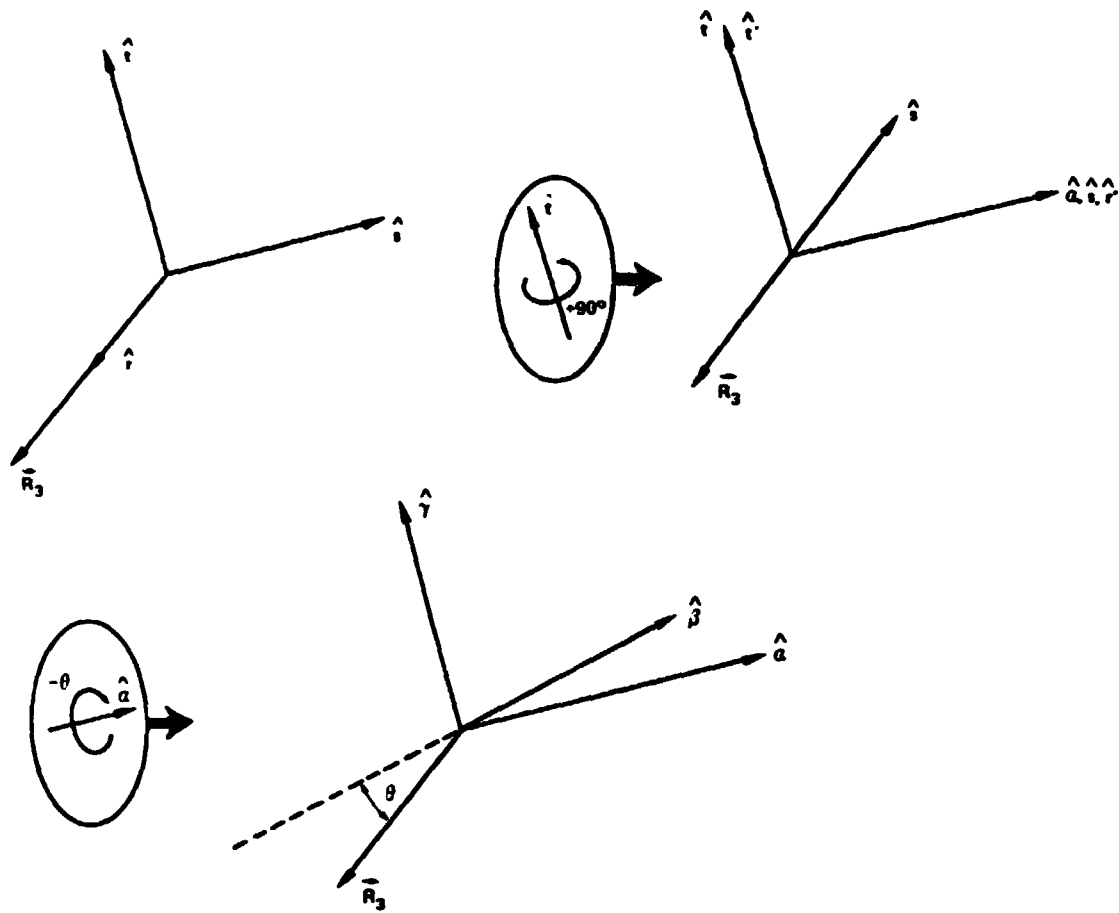


Figure A-5. Transformation of \vec{R}_3 .

The complete coordinate transformation matrix equation for \vec{R}_3 is given as follows:

$$\vec{R}_3 = \begin{bmatrix} 1 & 0 & 0 \\ 0 & \cos \nu & -\sin \nu \\ 0 & \sin \nu & \cos \nu \end{bmatrix} \begin{bmatrix} \cos \eta & -\sin \eta & 0 \\ \sin \eta & \cos \eta & 0 \\ 0 & 0 & 1 \end{bmatrix} \begin{bmatrix} 1 & 0 & 0 \\ 0 & \cos \theta & -\sin \theta \\ 0 & \sin \theta & \cos \theta \end{bmatrix} \begin{bmatrix} 0 & 1 & 0 \\ -1 & 0 & 0 \\ 0 & 0 & 1 \end{bmatrix} \begin{bmatrix} |\vec{R}_3| \\ 0 \\ 0 \end{bmatrix}$$

$$\vec{R}_3(x_c, y_c, z_c) = \begin{bmatrix} \cos \theta \cdot \sin \eta \cdot |\vec{R}_3| \\ -\cos \nu \cdot \cos \theta \cdot \cos \eta \cdot |\vec{R}_3| + \sin \nu \cdot \sin \theta \cdot |\vec{R}_3| \\ -\sin \nu \cdot \cos \theta \cdot \cos \eta \cdot |\vec{R}_3| - \cos \nu \cdot \sin \theta \cdot |\vec{R}_3| \end{bmatrix}.$$

The position of the particle can be defined in terms of the distance from the nozzle. For a particle velocity V and a time t after the emergence of the particle from the nozzle, then the distance is Vt ; i. e.,

$$|\vec{R}_2 + \vec{R}_3| = Vt \quad .$$

From Figure A-6, one has the following relations:

$$|\vec{R}_2| = \cos \beta \cdot Vt$$

$$|\vec{R}_3| = \sin \beta \cdot Vt \quad ,$$

where β is the angle between the trajectory and the nozzle axis. Hence, the particle position \vec{R} in the camera coordinate system is given as follows:

$$x_c = x_c^1 + \cos \eta \cos \beta \cdot Vt + \cos \theta \sin \eta \sin \beta \cdot Vt$$

$$y_c = y_c^1 + \cos \nu \sin \eta \cos \beta \cdot Vt - \cos \nu \cos \theta \cos \eta \sin \beta \cdot Vt \\ + \sin \nu \sin \theta \sin \beta \cdot Vt$$

$$z_c = z_c^1 + \sin \nu \sin \eta \cos \beta \cdot Vt - \sin \nu \cos \theta \cos \eta \sin \beta \cdot Vt \\ - \cos \nu \sin \theta \sin \beta \cdot Vt$$

$$|\vec{R}| = \left(x_c^2 + y_c^2 + z_c^2 \right)^{1/2} \quad .$$

The parameters to the above questions are (1) x_c^1, y_c^1, z_c^1 = the nozzle position relative to the camera; (2) η, ν = the orientation of the nozzle axis with respect to x_c, y_c, z_c ; (3) V, β, θ = the particle trajectory in polar coordinates relative to the nozzle axis; and (4) t = time since the emergence of the particle from the nozzle.

SCATTERING THEORY

As the particles transverse their trajectories, they are observed due to the scattering of sunlight. The scattered radiance flux per unit area per

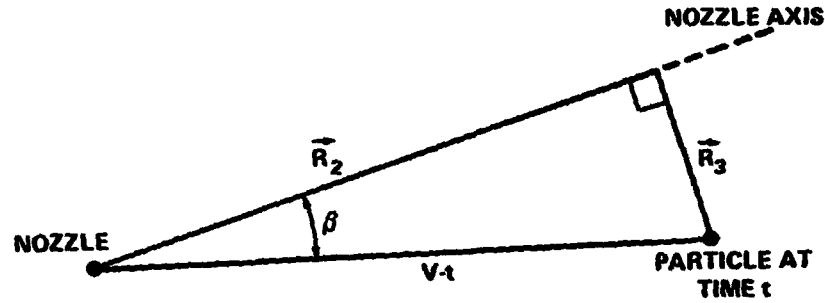


Figure A-6. Position parameter $V \cdot t$.

unit wavelength L_s^λ for a particle is given as follows:

$$L_s^\lambda = \frac{L_{\text{sun}}^\lambda}{R^2} \frac{d\sigma}{d\Omega} \text{ [energy area}^{-1} \text{ time}^{-1}] \quad ,$$

where L_{sun}^λ is the solar spectral radiance flux per unit area at the earth, R is the distance from the particle to a perpendicular area (in this study the camera lens), and $d\sigma/d\Omega$ is the differential scattering cross section for the particles as a function of the scattering angle θ . The scattering angle is defined as the angle between the direction of the incident light and the direction of the scattered light. The differential scattering cross section is defined as the ratio of the flux per unit solid angle scattered from an object to the flux incident on the object per unit area. The value L_s^λ will give the power incident on the camera lens when multiplied by the area of the camera lens and integrated over wavelength.

The differential scattering cross section is determined by the physical shape and chemical structure of the particle. In general, the nature of the particles is not known. However, the effects of the particles can be studied by assuming isotopic scatterers or by assuming spherical particles and using the Mie theory to find the differential cross section.

The isotopic model assumes that all the energy incident on a particle is scattered isotopically. The isotope differential scattering cross section is given as

$$\frac{d\sigma}{d\Omega} = \frac{a^2}{4} .$$

This model is independent of wavelength, refractive index, and scattering angle; hence, L_s is dependent only on L_{sun} and $1/R^2$.

SCATTERING ANGLE

The scattering angle is dependent on the relative position of the particle, the camera, and the sun. These relative positions can be determined by knowing the orientation of the camera system in the celestial sphere, the celestial coordinates of the sun, and the line of sight to the particle. Hence, it is assumed that the right ascension and declination of the $+x_c$ axis and the sun are known. Also, the rotational orientation of the camera and the (y_c, z_c) point of the particle (i. e., the line of sight) must be known. Figure A-7 shows the various axes extended to the celestial sphere. The x_c axis is pointed toward the right ascension RA_x and the declination DEC_x . The line of sight to the particle extends to the point (RA_p, DEC_p) . The sun is at (RA_s, DEC_s) , and the y_c axis is at (RA_y, DEC_y) . The camera coordinate orientation is different from the celestial coordinates and the rotation between them must be determined in order to determine the line of sight (RA_p, DEC_p) of the particle. Figure A-8 shows the spherical trigonometry for the program. ϵ is the angle between the line of sight to the particle and the x_c axis:

$$\epsilon = \arctan \left[\frac{(y_c^2 + z_c^2)^{1/2}}{x_c} \right] .$$

ξ is the angle between the y_c axis and the declination axis at the x_c axis:

$$\xi = \arccos \left[\sin(DEC_y) \cos(DEC_x) - \cos(DEC_y) \sin(DEC_x) \cos(RA_y - RA_x) \right] - 90 .$$

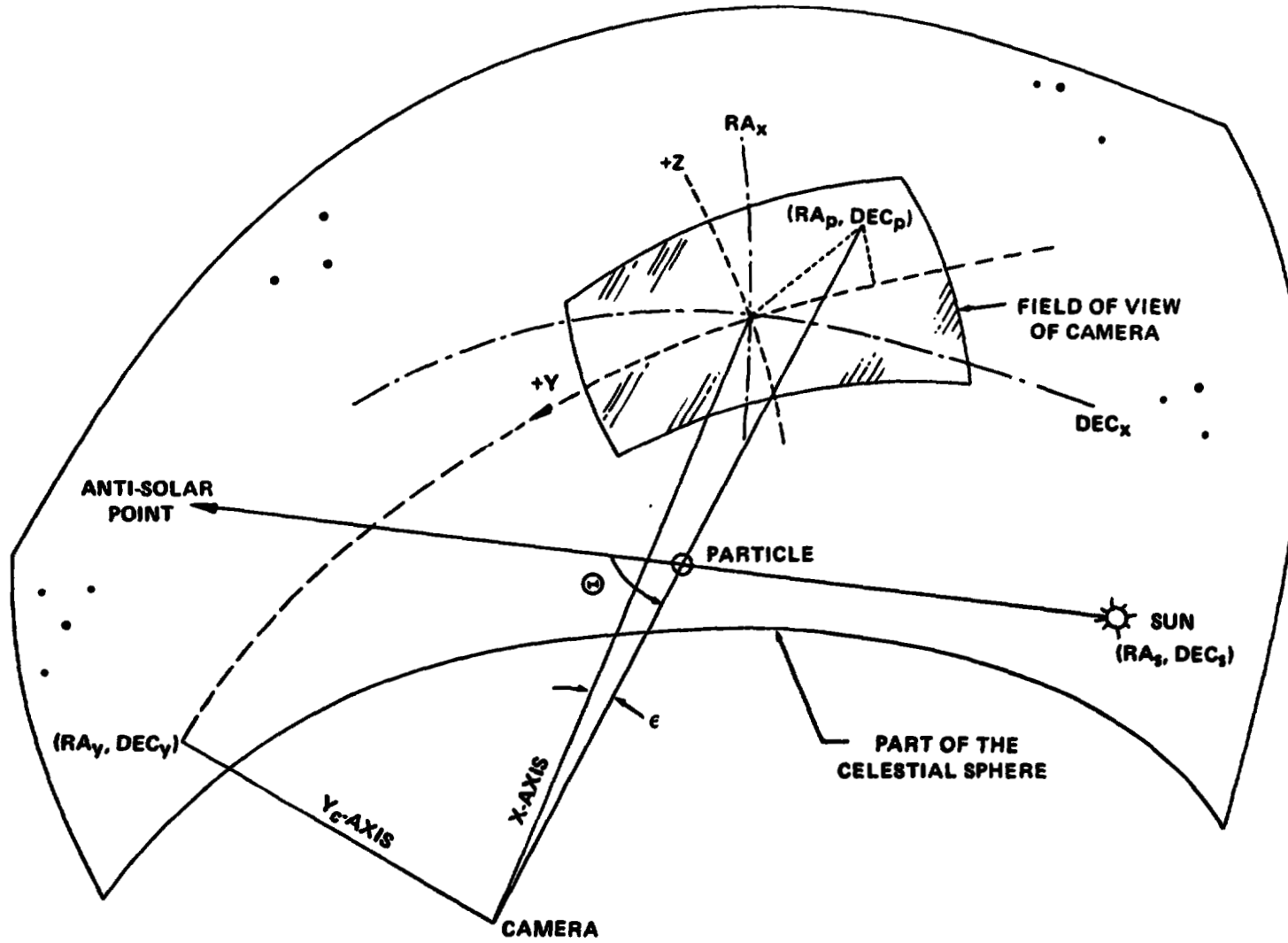


Figure A-7. The scattering angle Θ .

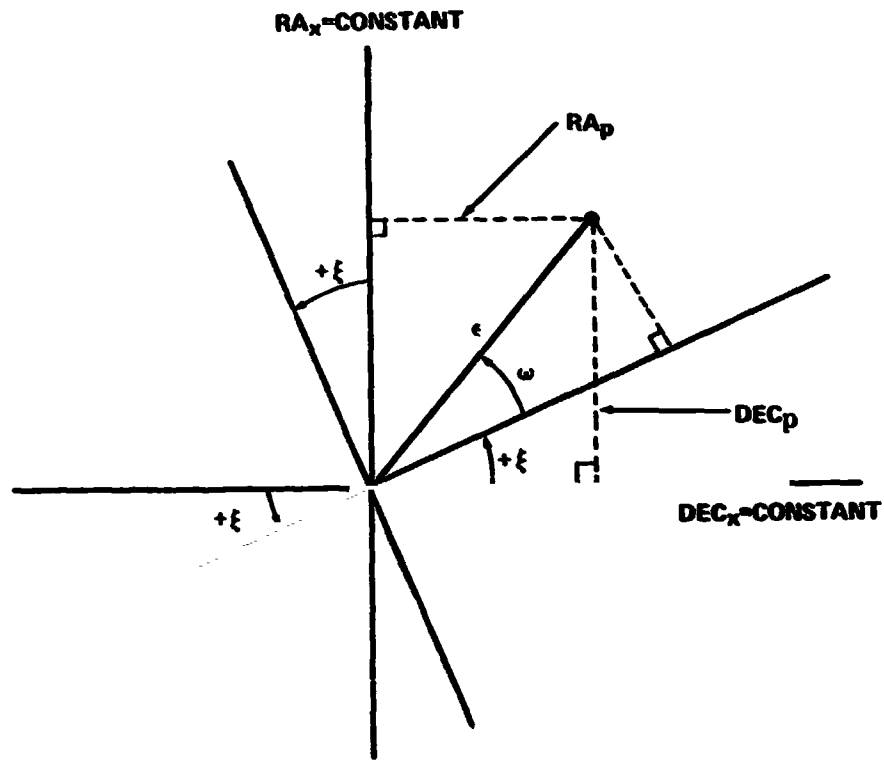


Figure A-8. Spherical trigonometry.

The positive direction of ξ is as shown in Figure A-8*, and ω is the angle defined by:

$$\omega = \arctan \left(\frac{z_c}{-y_c} \right) .$$

*If (DEC_x, RA_x) is given, then $DEC_y = 90^\circ - \arccos [-\cos (DEC_x) \sin \xi]$

and

$$RA_y = \arccos \left[\frac{\sin (DEC_x) \sin (\xi)}{\cos (DEC_y)} \right] + RA_x .$$

The correction for the right ascension and declination of the line of sight of the particles to that of the x_c axis is RA_d and DEC_d . By trigonometry, these corrections are given as follows:

$$DEC_d = \arcsin [\sin \epsilon \sin (\omega + \xi)]$$

$$RA_d = \arcsin [\sin \epsilon \cos (\omega + \xi) / \cos DEC_d] \quad .$$

Hence, the celestial coordinates of the particle line of sight are as follows:

$$RA_p = RA_x - RA_d$$

$$DEC_p = DEC_x + DEC_d \quad .$$

Note that the negative sign in the right ascension equation is a result of the right ascension increase along the $+y_c$ axis direction.

Now the scattering angle is the spherical trigonometry difference between the solar direction (RA_s, DEC_s) and the line of sight through the particle (RA_p, DEC_p). From Figure A-9 the scattering angle is given as follows:

$$\cos \Theta = [\cos (|RA_p - RA_s|) + \cos^2 (90 - DEC_s) (1 - \cos (|RA_p - RA_s|))] \cos (|DEC_p - DEC_s|) \quad .$$

The parameters for the scattering angle equation are RA_s, DEC_s = solar celestial coordinates; x_c, y_c, z_c = particle camera coordinates; and RA_x, DEC_x and RA_y, DEC_y or ξ = the spacecraft orientation.

SPACECRAFT MOTION

The following statements concern the effects of a spacecraft rotation and an effective translation upon the position of a particle in the camera coordinate system. The coordinate systems to be considered are shown in Figure A-10. The particle camera coordinates are (x_c^p, y_c^p, z_c^p) , and, after a

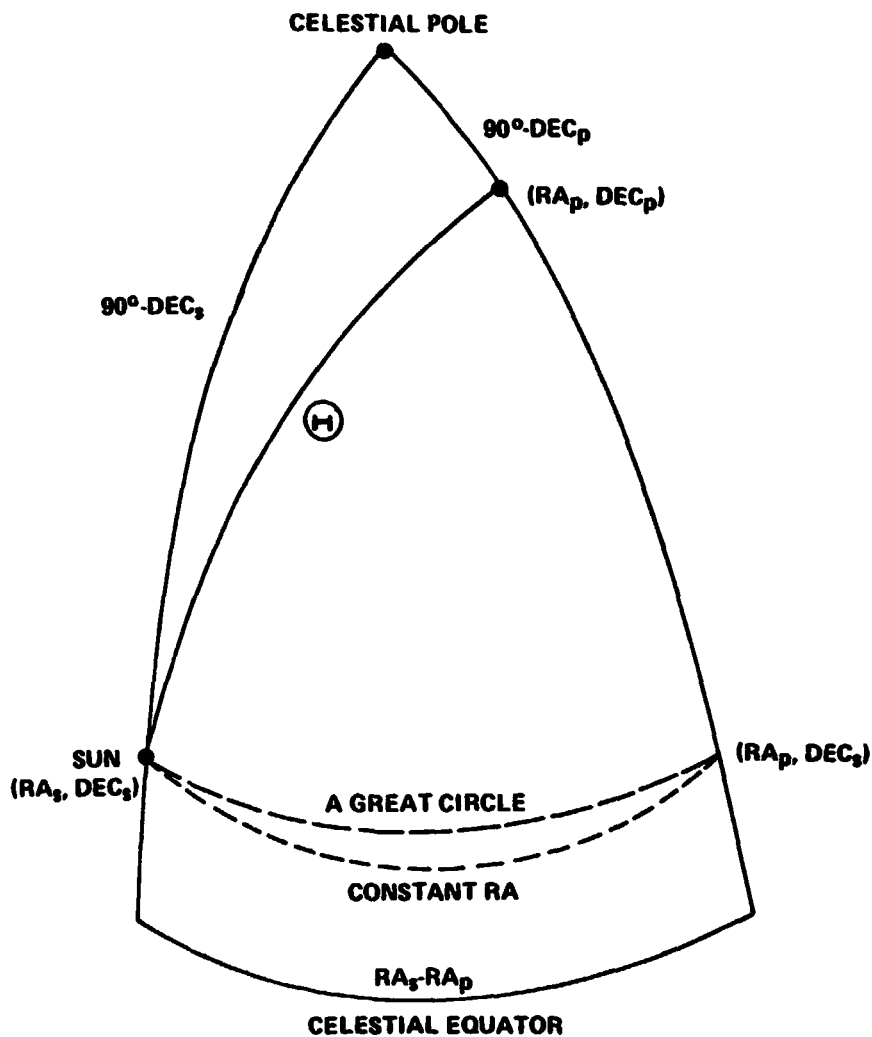


Figure A-9. The scattering angle θ in terms of right ascension.

rotation and a translation at time $t = T$, the coordinates are $(\tilde{x}_c^p, \tilde{y}_c^p, \tilde{z}_c^p)$. Similar notation is used for the coordinates of the particle in the spacecraft center of mass system; i.e., $x_{cm}^p, y_{cm}^p, z_{cm}^p$ and $\tilde{x}_{cm}^p, \tilde{y}_{cm}^p, \tilde{z}_{cm}^p$.

The procedure is to find the particle in the camera coordinate system assuming no transformation (i.e., rotation or translation) and then convert over into the center of mass coordinates (cm). After the cm coordinates are obtained, the transformations are performed. Thereafter, the conversion of the cm coordinates to the camera coordinates gives the new relative position for the particle with respect to the camera.

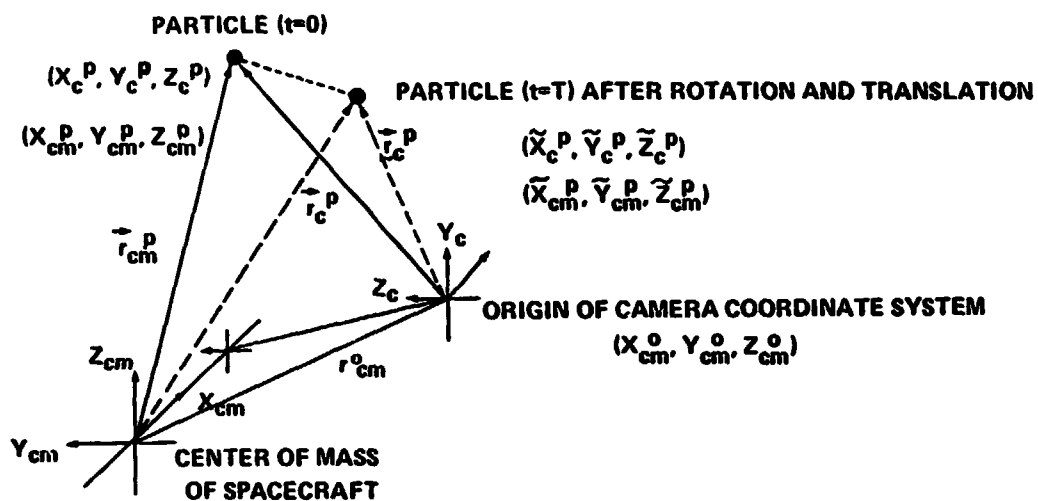


Figure A-10. Coordinate systems for spacecraft motion considerations.

The particle coordinates in the cm system are given by:

$$x_{cm}^p = x_{cm}^o + x_c^p$$

$$y_{cm}^p = y_{cm}^o + y_c^p$$

$$z_{cm}^p = z_{cm}^o + z_c^p$$

where $(x_{cm}^o, y_{cm}^o, z_{cm}^o)$ is the origin of the camera system in terms of cm coordinates.

Now assume that the cm has an acceleration of $a_{cm} = (a_x, a_y, a_z)$ during time Δt from the particle emergence until the time being considered. The effective translation is then:

$$x_{cm}^t = \frac{1}{2} a_x (\Delta t)^2$$

$$y_{cm}^t = \frac{1}{2} a_y (\Delta t)^2$$

$$z_{cm}^t = \frac{1}{2} a_z (\Delta t)^2 \quad .$$

The cm coordinates after translation are:

$$x_{cm}^p = x_{cm}^o + \frac{1}{2} a_x (\Delta t)^2$$

$$y_{cm}^p = y_{cm}^o + \frac{1}{2} a_y (\Delta t)^2$$

$$z_{cm}^p = z_{cm}^o + \frac{1}{2} a_z (\Delta t)^2 \quad .$$

The rate of rotation is given by the rate of the gimbal angles which are a set of Euler angles relating the spacecraft axes to an inertial system. Let $\dot{\phi}_G$, $\dot{\theta}_G$, and $\dot{\psi}_G$ be the rates of a set of Eulerian angles ϕ_G , θ_G , and ψ_G ; then the rotation of the spacecraft is given as follows:

$$\phi_G = \dot{\phi}_G \Delta t$$

$$\theta_G = \dot{\theta}_G \Delta t$$

$$\psi_G = \dot{\psi}_G \Delta t \quad .$$

Therefore, the particle position in the rotated cm coordinates is given by the following equations [10]:

$$\begin{aligned} \tilde{x}_{cm}^p &= [\cos \psi_G \cos \phi_G - \cos \theta_G \sin \phi_G \sin \psi_G] x_{cm}^p \\ &+ [\cos \psi_G \sin \phi_G + \cos \theta_G \cos \phi_G \sin \psi_G] y_{cm}^p \\ &+ [\sin \psi_G \sin \theta_G] z_{cm}^p \quad , \end{aligned}$$

$$\begin{aligned} \tilde{y}_{cm}^p &= [-\sin \psi_G \cos \phi_G - \cos \theta_G \sin \phi_G \cos \psi_G] x_{cm}^p \\ &+ [-\sin \psi_G \sin \phi_G + \cos \theta_G \cos \phi_G \cos \psi_G] y_{cm}^p \\ &+ [\cos \psi_G \sin \theta_G] z_{cm}^p \end{aligned}$$

$$\begin{aligned}\tilde{z}_{cm}^p &= [\sin \theta_G \sin \phi_G] x_{cm}^p + [-\sin \theta_G \cos \phi_G] y_{cm}^p \\ &+ [\cos \theta_G] z_{cm}^p \quad .\end{aligned}$$

Now, after the rotation, the new camera coordinates are given as follows:

$$\begin{aligned}\tilde{x}_c^p &= x_{cm}^p - x_{cm}^o \\ \tilde{y}_c^p &= y_{cm}^p - y_{cm}^o \\ \tilde{z}_c^p &= z_{cm}^p - z_{cm}^o \quad .\end{aligned}$$

The celestial positions of the rotated \tilde{x}_c and \tilde{y}_c axes are now to be determined. One must first calculate the original $+z_c$ axis in celestial coordinates. Using ξ , one finds DEC_z and RA_z similar to DEC_y and RA_y :

$$\begin{aligned}DEC_z &= 90^\circ - \cos^{-1} [-\cos(DEC_x) \sin(\xi - 90^\circ)] \\ RA_z &= RA_x + \cos^{-1} \left[\frac{\sin(DEC_x) \sin(\xi - 90^\circ)}{\cos(DEC_z)} \right] \quad .\end{aligned}$$

The directional cosines between the celestial Cartesian coordinates (l, m, n) and the unrotated camera coordinates (x_c, y_c, z_c) are given by:

$$\begin{aligned}\alpha_w &\equiv \cos(\langle n, w \rangle) = \cos(90 - DEC_w) \\ \beta_w &\equiv \cos(\langle l, w \rangle) = \cos(RA_w) \cos(DEC_w) \\ \gamma_w &\equiv \cos(\langle m, w \rangle) = \cos(RA_w - 90) \cos(DEC_w) \quad ,\end{aligned}$$

where w refers to x_c, y_c , or z_c axes.

Then the $+x_c$ values in the (l, m, n) system are given as follows:

$$\begin{pmatrix} l_x \\ m_x \\ n_x \end{pmatrix} = \begin{pmatrix} \alpha_x & \alpha_y & \alpha_z \\ \beta_x & \beta_y & \beta_z \\ \gamma_x & \gamma_y & \gamma_z \end{pmatrix} \begin{pmatrix} l \\ m \\ n \end{pmatrix},$$

where $+y_c$ and $+z_c$ are obtained similarly. Hence the values of l_x, m_x, n_x , etc., for the rotated values are obtained by the matrix equation:

$$\begin{bmatrix} \tilde{l}_w \\ \tilde{m}_w \\ \tilde{n}_w \end{bmatrix} = \begin{bmatrix} \cos \psi \cos \phi - \cos \theta \sin \phi \sin \psi & -\cos \psi \sin \phi - \cos \theta \cos \phi \cos \psi & \sin \psi \sin \theta \\ \sin \psi \cos \phi + \cos \theta \sin \phi \cos \psi & -\sin \psi \sin \phi + \cos \theta \cos \phi \sin \psi & -\cos \psi \sin \theta \\ \sin \theta \sin \phi & \sin \theta \cos \phi & \cos \theta \end{bmatrix} \begin{bmatrix} l_w \\ m_w \\ n_w \end{bmatrix}.$$

where angles in the rotation matrix have taken on negative values for the angular rates. The rotated $+x_c$ and $+y_c$ positions are determined from:

$$RA_w = \arctan(\tilde{m}_w / \tilde{l}_w)$$

$$DEC_w = \arcsin(\tilde{n}_w)$$

and can be used to calculate the new scattering angles.

IMAGE THEORY

The calculated position, distance, and radiance for the particles are transformed by the camera into a recorded image. The image depends on optical transformation performed by the camera.

The camera forms a perspective projection of the object points. Normally, this projection is inverted, but for analysis the inversion will not be considered. The location of each point on the film is given by the tangent of the

angle between the line of sight to the point to be projected and the vector normal to the center of the plane of the film (the x_c axis of the camera system)

(Fig. A-11). Given the camera coordinate system, assume a vector \vec{R} in that system pointing toward the point to be imaged. Then the y_f and z_f coordinates on the film of the projection of the point are given as follows:

$$y_f = (-y_c / x_c) F1$$

$$z_f = (-z_c / x_c) F1$$

where $\vec{R} = (x_c, y_c, z_c)$ and $F1$ is the focal length of the camera.

The field of view of the camera determines if the particle will appear on the film plane. Using x_c as a parameter and for a camera with a δ degrees by μ degrees format, the defining equations are as follows:

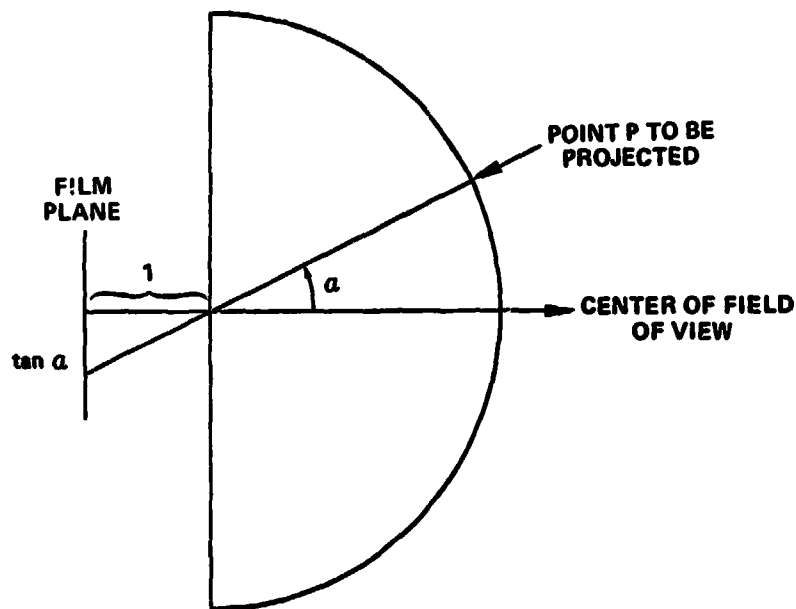


Figure A-11. Perspective projection.

$$-x_c \tan \delta < y_c \leq + x_c \tan \delta$$

$$-x_c \tan \mu \leq z_c \leq + x_c \tan \mu$$

as shown in Figure A-12.

The effective diameter on the film will be derived by using basic optics. If a point source is not focused by the camera, the image will be enlarged. Let s_o and s'_o be the object distance and the image distance, respectively, for the actual camera settings determined by [11],

$$\frac{1}{F1} = \frac{1}{s_o} + \frac{1}{s'_o} \quad .$$

For the true object distance s , the image distance s' is given as follows:

$$\frac{1}{F1} = \frac{1}{s} + \frac{1}{s'} \quad .$$

From the last two equations and Figure A-13, the effective image size d_G , as a result of having the film plane not at the focal point, is given as follows:

$$d_G = |s'_o - s'| \cdot D/s' \quad .$$

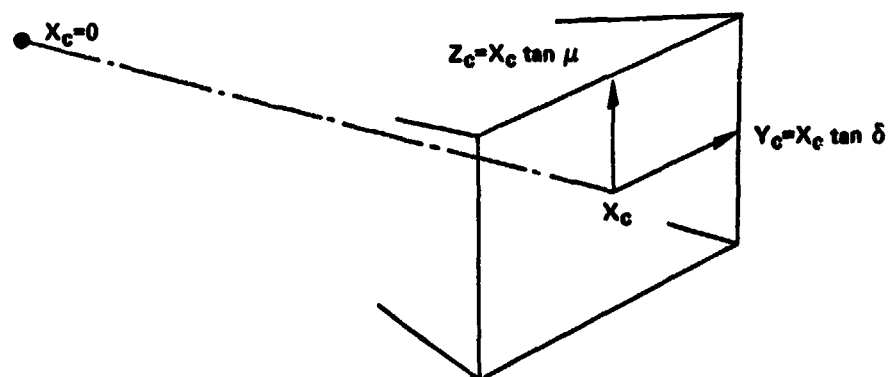


Figure A-12. Field-of-view boundaries

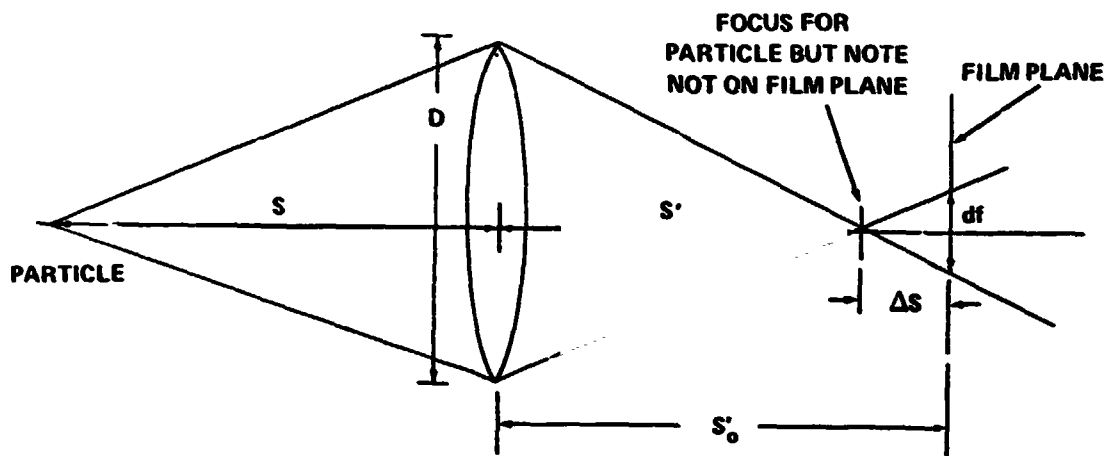


Figure A-13. Defocusing effects.

This equation can be written as:

$$d_G = |s - s_0| \cdot F1 \cdot D / (s |s_0 - F1|)$$

or in camera coordinates this becomes

$$d_G = |x_c - x_c^0| \cdot F1 \cdot D / (x_c |x_c^0 - F1|) ,$$

where x_c^0 is the object distance setting of the camera. Hence, the image size for a particle on the film decreases as the particle reaches the object distance setting and then increases.

For an extended source of radius a , the image size for a focused particle will be:

$$d_I = a s' / s$$

or in camera coordinates:

$$d_I = a F1 / |F1 - x_c|$$

where similar equations are employed as before.

Diffraction by the lens aperture increases the diameter by a term of:

$$d_D = 2\lambda F1/D$$

where λ is the effective wavelength and D is the diameter of the lens.

The effect of diffusion of light within the film gives an additional term d_F [12]. Hence, an estimate of the image size on the film becomes:

$$d = |x_c - x_c^0| D \cdot F1 / (x_c |x_c^0 - F1|) + d_F + 2 \cdot \lambda \cdot F1/D + aF1/|F1-x_c| \quad .$$

Further improvement of the above formula would employ the optical transfer function for the camera being used.

DENSITY LEVEL

The density level obtained on the film depends on the radiance at the film and the film sensitivity.

The scattered spectral radiance $L_s(\lambda)$ times the area of the camera lens $\pi D^2/4$ defines the power incident into the camera system. This power is concentrated into the image of area $\pi d^2/4$; hence, the spectral radiance of the film is:

$$E(\lambda) = L_s(\lambda) \frac{D^2}{d^2} \quad .$$

For a particular developing process the spectral film sensitivity $S(\lambda)$ is defined as the reciprocal of the exposure required at a given wavelength to produce a given density. Thus, the energy per unit area required to produce a given density D is given by

$$E(D, \lambda) = \frac{1}{S(D, \lambda) t} \quad ,$$

where t = exposure time.

The energy per unit area at the film from a particle scattering sunlight is given by

$$E = \int_0^{\infty} \frac{L_{\text{sun}}(\lambda)}{R^2} \frac{D^2}{d^2} \frac{d\sigma}{d\Omega}(\theta, \lambda) d\lambda$$

The density produced by the resulting exposure is determined from the appropriate characteristic curve for the film and processing.

The differential scattering cross section θ dependence would be included by taking an integral over the solid angle defined by the camera lens [13]. The variation in θ is small, and the value of $d\sigma/d\Omega$ at the average value of θ is assumed.

The formulation developed in this section allows one to determine the photographic images of particles emerging from a nozzle and traversing the field of view of a spacecraft camera. The approximations allow the determination of the optical image and density on the film.

Analysis

In this section, results of the developed perspective projections are presented. Views of various nozzle dumps and window locations are presented to establish a basis for the particular results from the various Apollo photography to be considered.

REPRESENTATIVE TRAJECTORIES

Figures A-14 and A-15 are the computer plots for a water dump as viewed from window 2 with a field-of-view of 20 by 20 deg (Hasselblad) about the x axis. In each case ($\beta = 50$ and 60 deg) the particle trajectory tracks are traced from when they enter the field of view from the left until 20 sec after they have emerged from the nozzle. The set per view is given for $\theta = +5, 0, -5, -10, -15,$ and -20 deg.

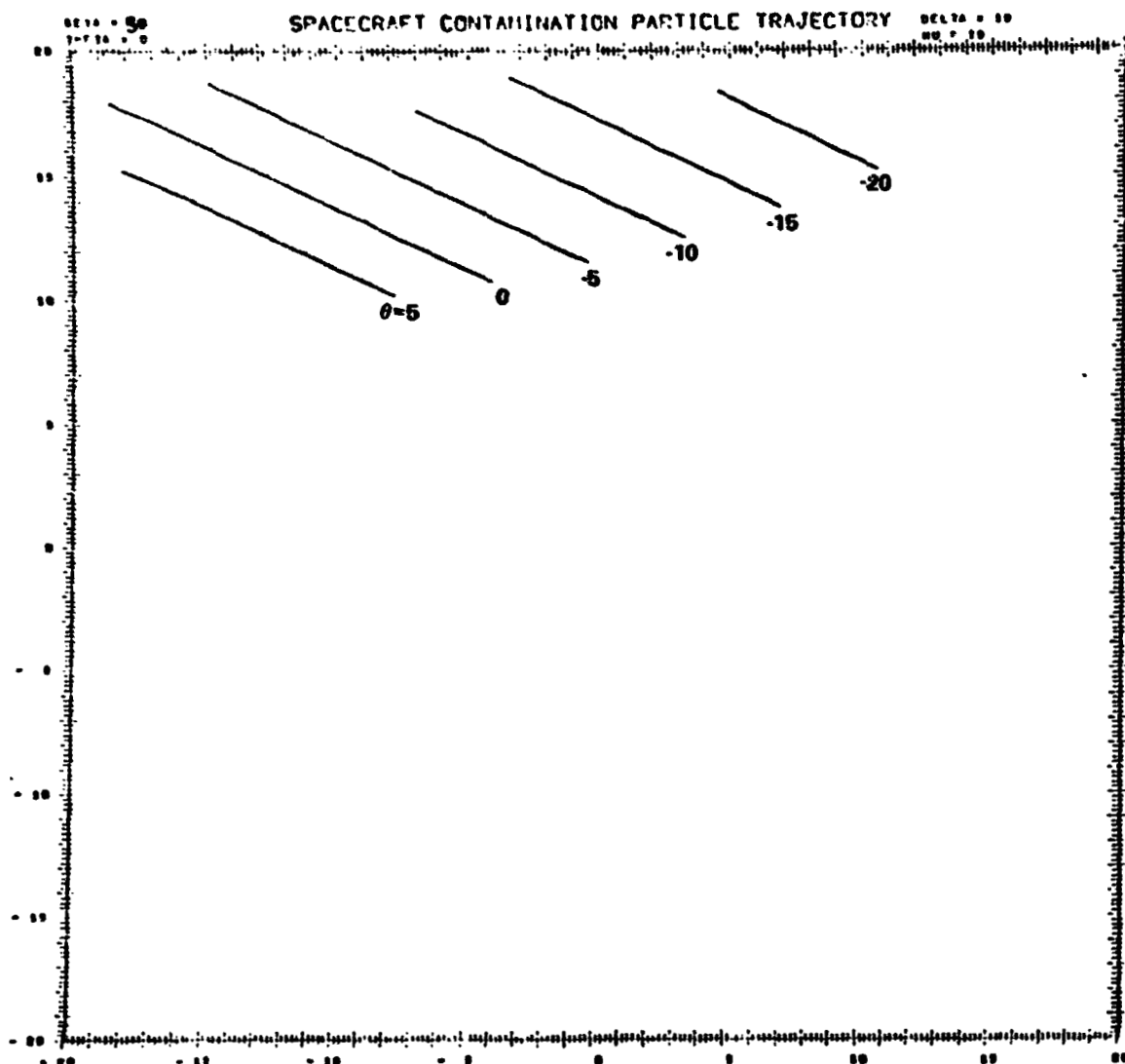


Figure A-14. Computer plot of particle from water dump as seen in window 2; $\beta = 50$ deg and $\theta = 5, 0, -5, -10, -15, -20$ deg.

Of particular importance is the case $\beta = 60$ and $\theta = 0$ deg. Then the particle's y_c and z_c coordinates are constant, and only x_c changes according to $x_c = x'_c + Vt$. Therefore, the particle's perspective trajectory appears to sweep toward the center of the field of view. The center of the frame is then the asymptotic limit for this case, since:

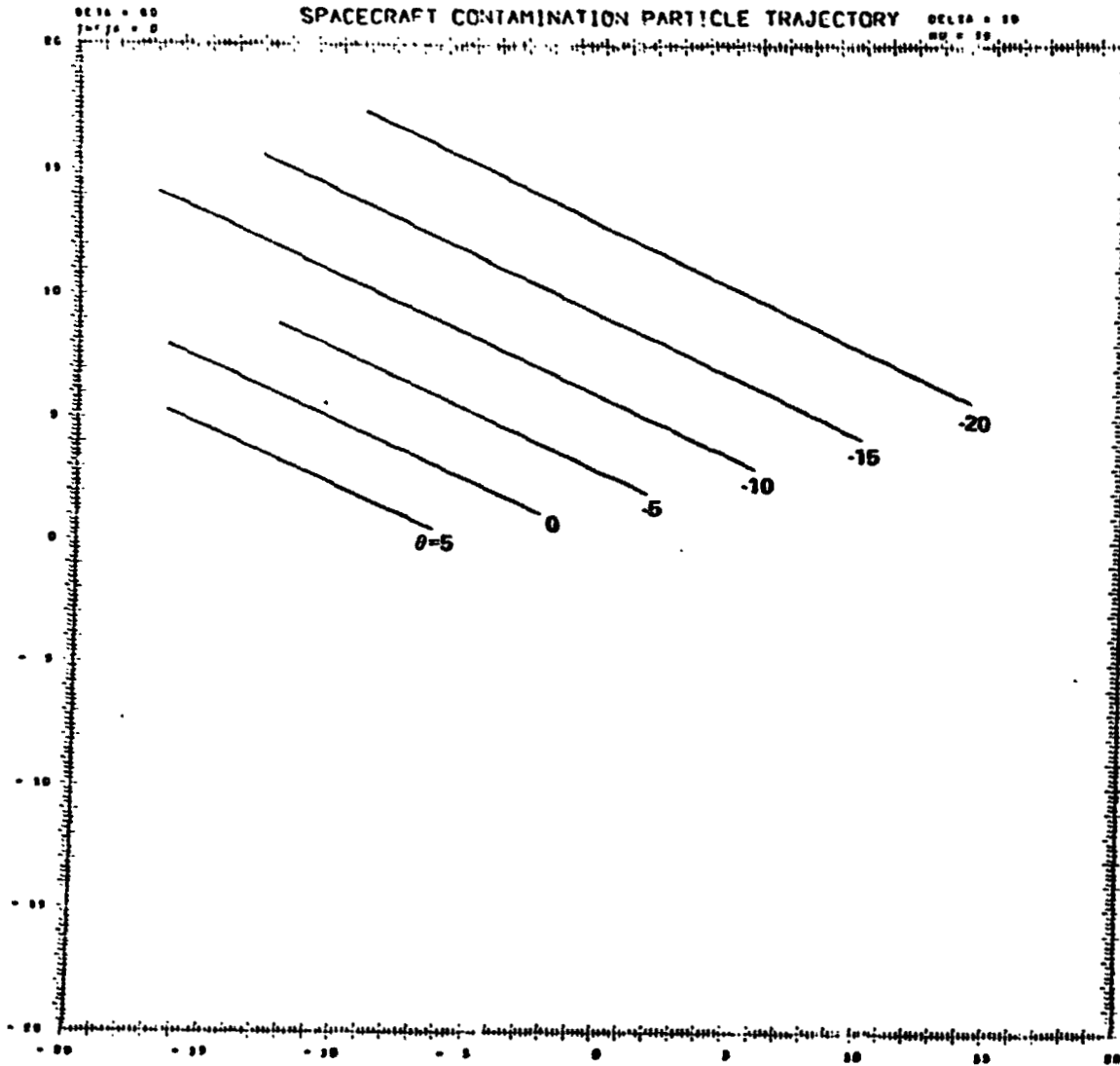


Figure A-15. Computer plot of particle from water dump as seen in window 2; $\beta = 60$ deg and $\theta = 5, 0, -5, -10, -15, -20$ deg.

$$\lim_{x_c \rightarrow \infty} \arctan \left[\frac{(y_c^2 + z_c^2)^{1/2}}{x_c} \right] \rightarrow 0$$

If the particles appear on the frame further away from the nozzle direction than the center, then it follows that these particles have a cone angle β greater than 60 deg.

For the set of β 's it is seen that as β increases, the cone formed by the termination of trajectories at $t = 20$ sec and the set of θ 's steps across the frame (Fig. A-16).

Figures A-17 and A-18 illustrate the effect of a spacecraft rotation. In this case, a hypothetical nozzle is located in front of the camera, and the spacecraft rates $\dot{\phi}$, $\dot{\theta}$, and $\dot{\psi}$ are a rapid 1 deg per sec. When the particle is close to the spacecraft, the angular rate across the frame is fast and the spacecraft

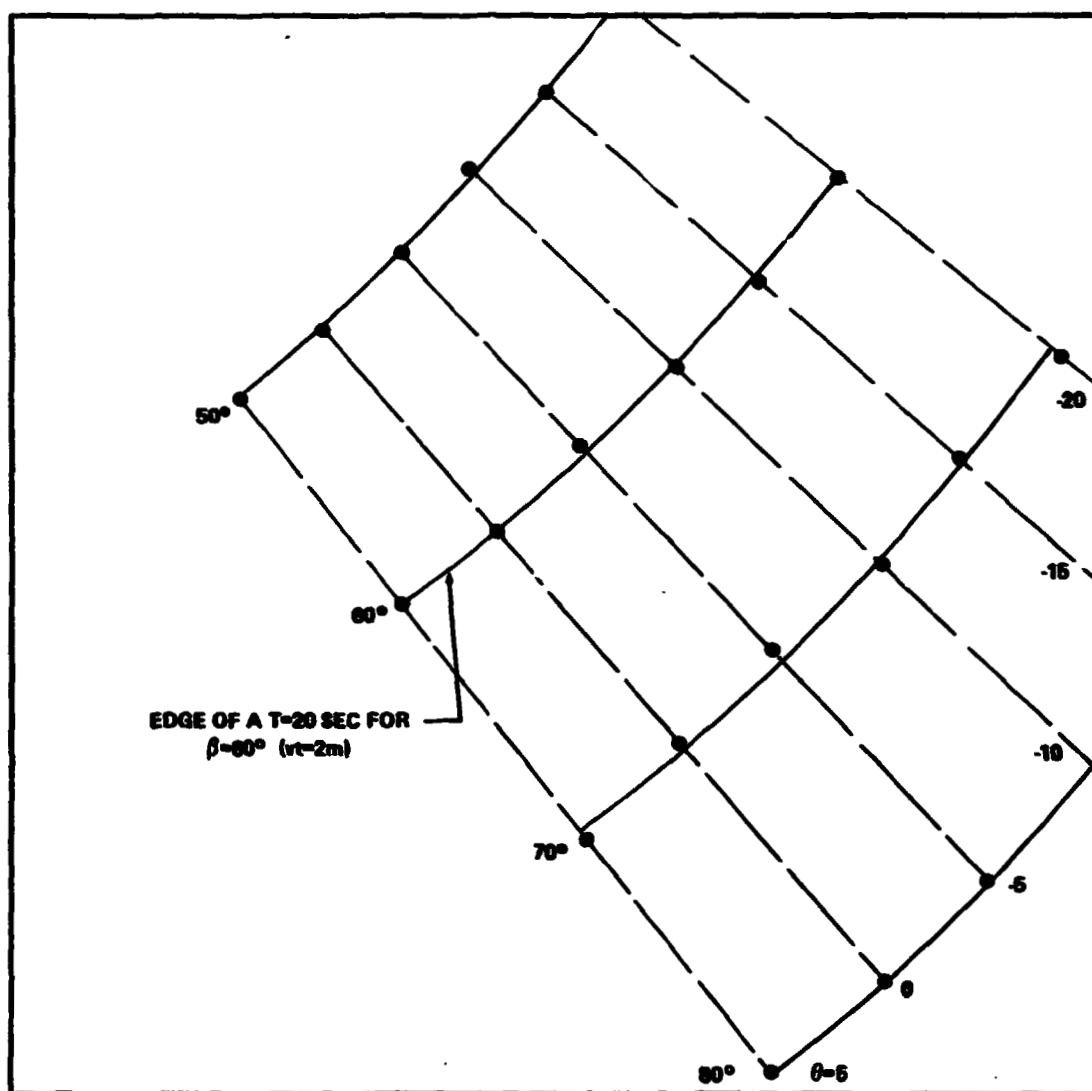


Figure A-16. Surfaces of the cones formed by water dump as seen from window 2; cones are defined by β and generated by θ .

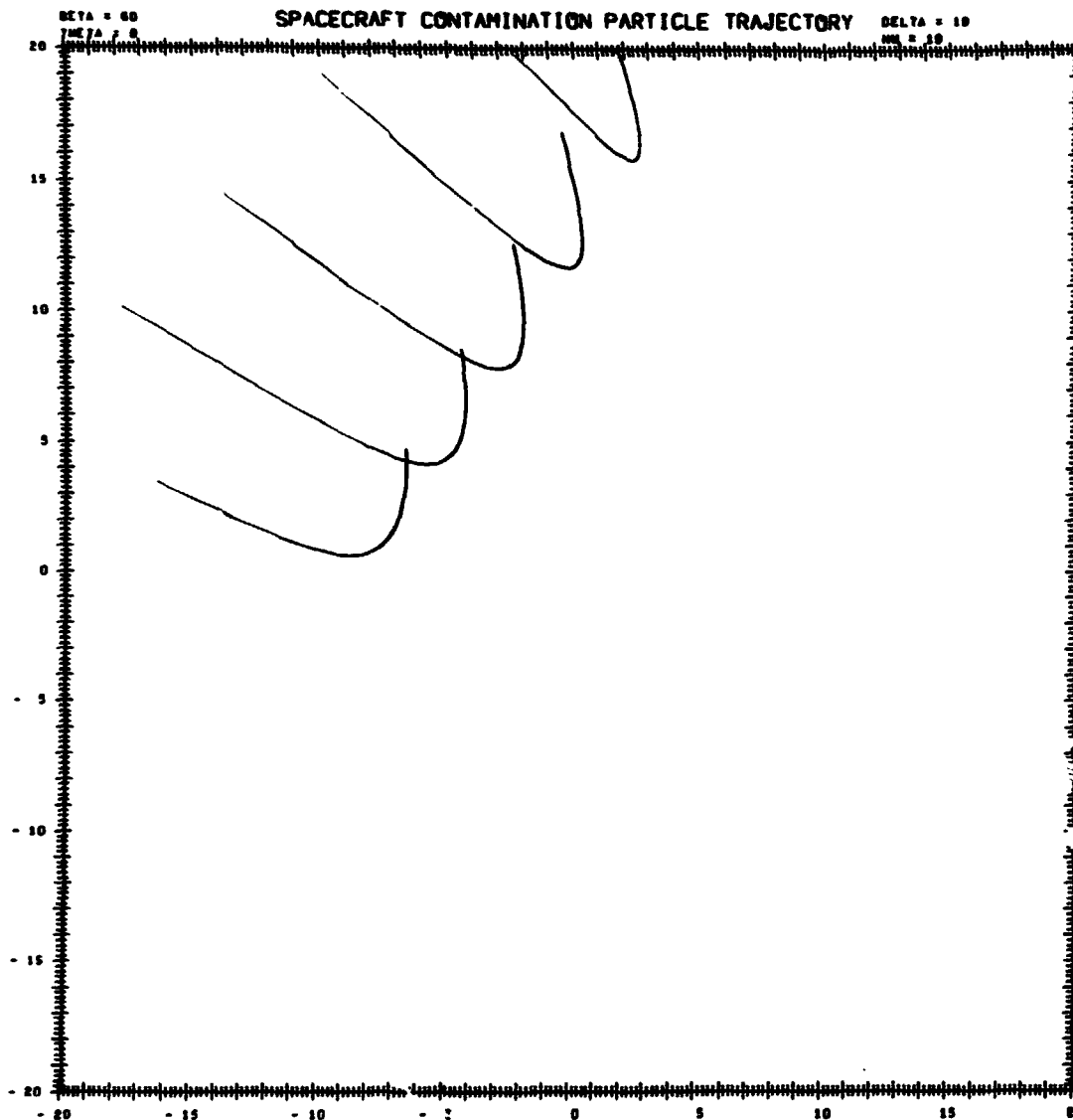


Figure A-17. Effect of spacecraft rotation on particle tracks as seen from window 2; $\beta = 60$ deg and $\theta = 5, 0, -5, -10, -15$ deg.

rates in comparison are slow. As the particle moves away from the spacecraft, the angular rate of the particle decreases and the spacecraft rate dominates. In the case illustrated, the spacecraft rotation is downward and drives the particle tracks toward the top of the frame. The angular rate for the particular particle for which y_c and z_c are constants and $x_c = x'_c + Vt$ is given as follows:

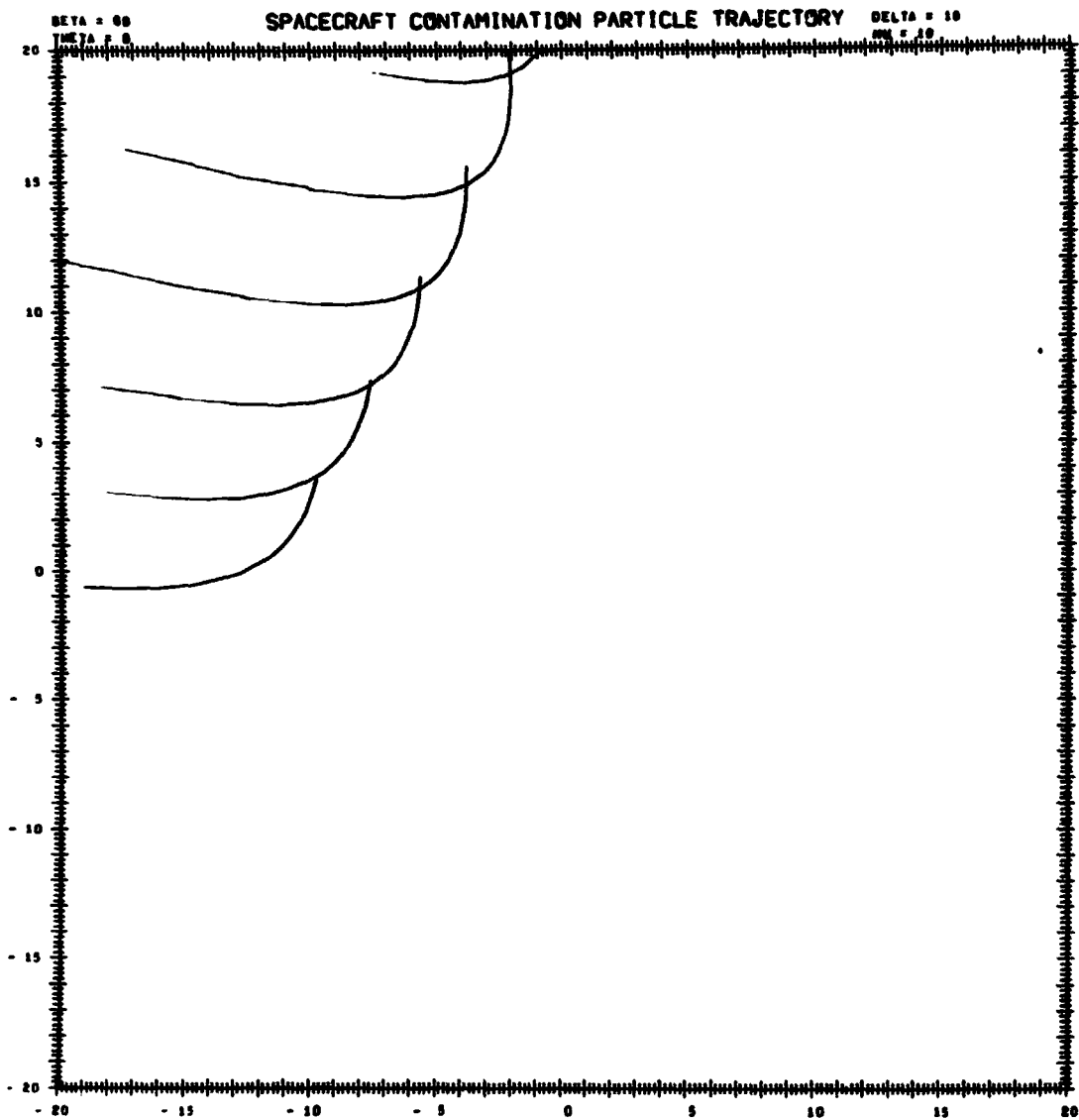


Figure A-18. Effect of spacecraft rotation on particle tracks as seen from window 4; $\beta = 60$ deg and $\theta = 5, 0, -5, -10, -15, -20$ deg.

$$\dot{\theta} = \frac{d\theta}{dt} = \frac{d}{dt} \left\{ \arctan \left[\frac{(y_c^2 + z_c^2)^{1/2}}{x_c + Vt} \right] \right\} = \frac{V (y_c^2 + z_c^2)^{1/2}}{(x_c + Vt)^2 + (y_c^2 + z_c^2)} = \frac{Vb}{r^2}$$

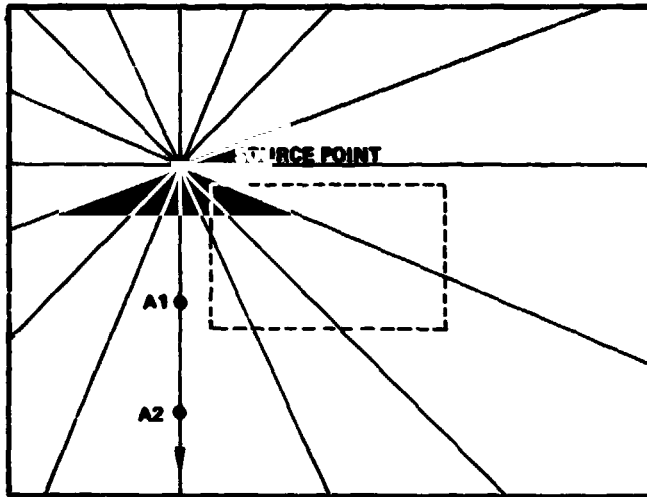
where $b = \sqrt{y_c^2 + z_c^2}$ and $r = \sqrt{(x_c + Vt)^2 + y_c^2 + z_c^2}$. Assuming that $\dot{\omega}$ is the spacecraft rotation rate and that it is perpendicular to the particle apparent motion, then the angle of the particle's apparent motion with its original track will increase according to $\arctan(r^2\dot{\omega}/Vb)$.

For Figures A-14 and A-15, the nozzle is located behind the camera $x_c = 0$ plane. As a result, the tracks of the emerging particles appear to converge as they pass in front of the camera instead of diverging as one would first expect. This perspective is illustrated in Figure A-19, where in Figure A-19(a) the source is in front of the camera and the particle tracks diverge from the source. In Figure A-19(b) the camera forming this frame is looking away from the source and the particles appear to converge. In Figure A-19(c) this result is shown as being strictly a result of geometry. Two particles emerge from the source; one particle (A) passes through point A1 then A2, and the other (B) passes through point B1 and B2. The particle A appears to radiate from the source as viewed by camera A. Particle B appears to converge toward the image point which is located by drawing a line from the source through the camera B. The points (A1, A2 and B1, B2) are shown in Figures A-19(a) and A-19(b) also. If a particle reached the image point without interference, then it would be viewed by camera B as a point.

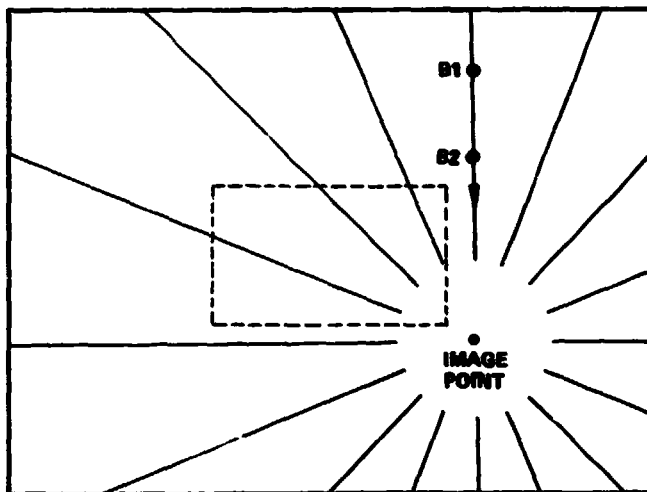
An accumulation for the trajectories from Figure A-14 is shown in Figure A-20. The tracks are continued outside the field of view and are shown to converge at the image point. The figure has been reflected about a plane normal to the paper.

As an illustration of the angular rate expected, the $\theta = 0$, $\beta = 60$ deg case is considered for a water dump as viewed from window 4. Figure A-21 depicts the position of the particle in 1-sec increments from a time 7 sec to 21 sec after it emerges. As seen from the equation for θ , this decrease in rate is approximately Vb/r^2 .

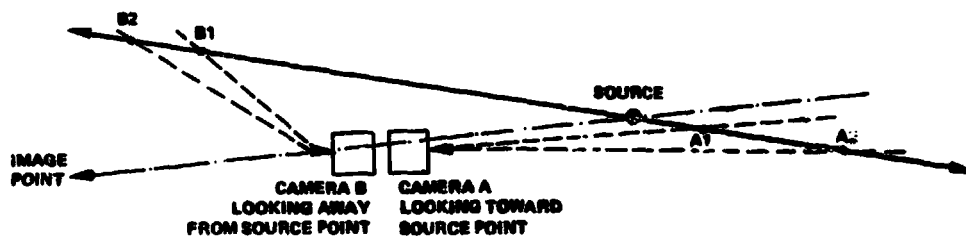
In terms of photographs, the exposure ($E = \text{irradiance times exposure time}$) determines the density levels obtained. As a particle recedes, the irradiance at the camera due to scattered light is proportional to $1/r^2$. Since the exposure time is dependent on how long a particle's light is impinging on a location on the film, then it is dependent on θ . Therefore, the exposure is approximately independent of the particle position. The further away the particle is, the weaker the irradiance, but it irradiates an area on the film longer before traveling to an adjacent area (Fig. A-22).



a. Source point in front of camera and in large field of view; small field of view shown as dashed box.



b. Source point behind camera and image point in large field of view.



c. Geometry of camera and source for a and b; dot-dash lines run through source and camera lens.

Figure A-19. Effect of location of source on particle tracks.

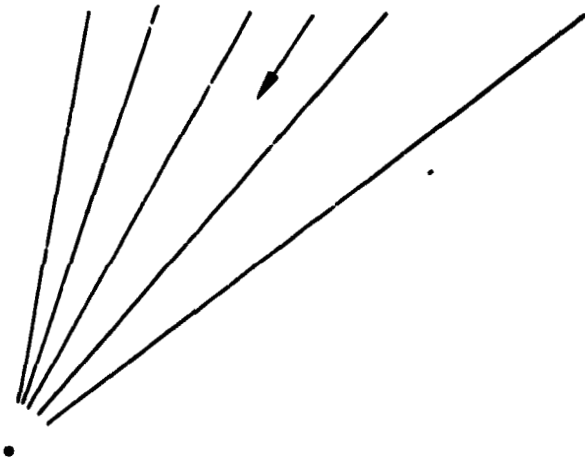
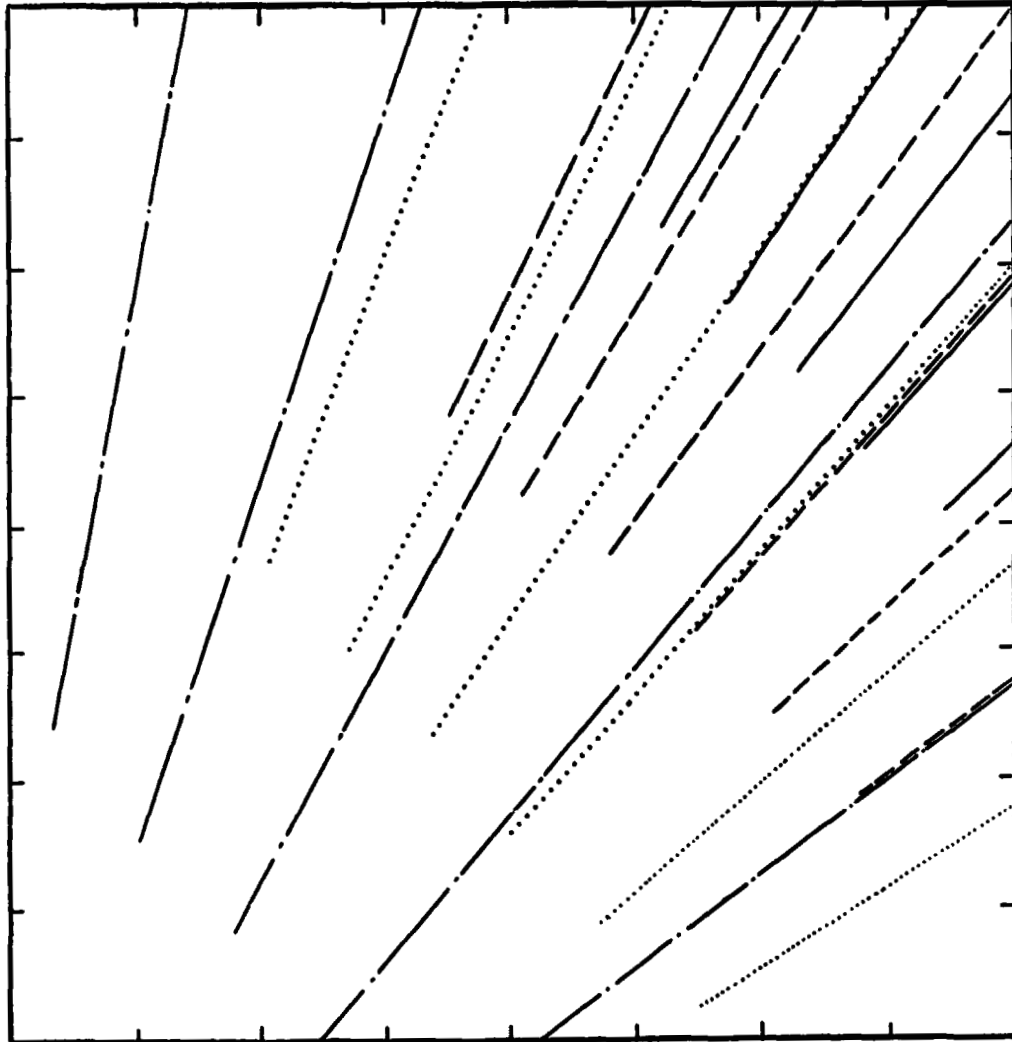


Figure A-20. Accumulation for trajectories of particles seen in Figure A-14.

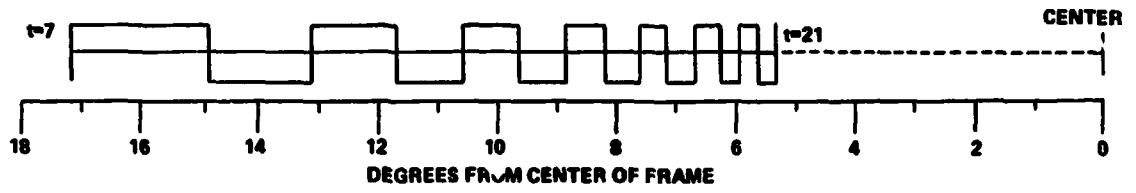


Figure A-21. Position of particle in 1-sec increments; $\theta = 0$ and $\beta = 60$ deg; window 4, water dump nozzle, and $V = 100$ cm/sec used to generate tracks.

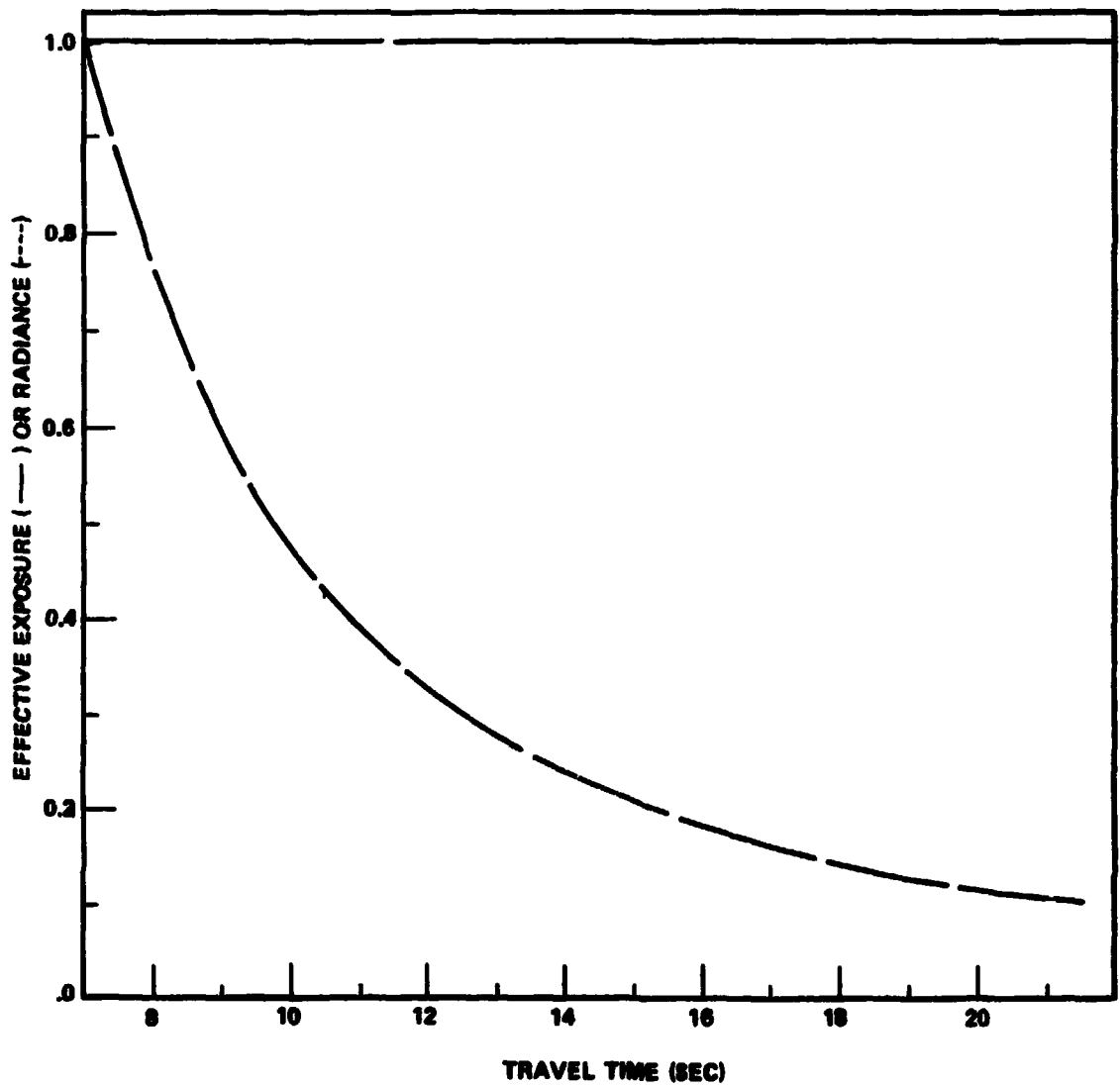


Figure A-22. Effective exposure versus time from emergence from nozzle; the effective radiance shows the $1/R^2$ effect.

Figure A-23 is an illustration of an auxiliary hatch dump viewed from windows 2 and 4 by a 16-mm DAC. In Figure A-23(a) the tracks for the left and right window are shown. From the indicated slopes, the tracks appear to be converging to an image point in each case. Figure A-23(b) represents a sample track obtained simultaneously from each window. In Figure A-24 a single track is analyzed in terms of the stereographic views. The vertical bars specify the position of the other camera's field of view at the indicated time. The particle had to be down the x_c axis by 220 cm before it could be observed by both cameras. The vertical starting and end points of a particle are the same for each camera. Since the particle is closer but above window 2, the slope of the trajectories in that case is more inclined.

As a prelude to the discussion of Apollo 15 photography, the theoretical results of a waste water dump and a urine dump as observed from window 4 are presented. Figure A-25 shows the same general tracks as Figure A-14. Table A-1 gives various time points and the location in normalized coordinates which give the center as (0, 0) and the upper right-hand corner as (1, 1). Figure A-26 and Table A-2 give the same information for a urine dump as viewed by the 16-mm DAC camera (24 x 32 deg). The extended trajectory tracks for both dump nozzles are given in Figure A-27 for window 4. The solid lines are coming from the water dump nozzle and the dashed lines are coming from the urine dump nozzle.

APOLLO 15 PHOTOGRAPHY

On the Apollo 15 mission, a series of photographs was taken from window 4 with the 16-mm DAC using the 18-mm lens [2]. The lens was set at $f/0.95$ and focused on infinity. Type S016 9W film was used.

Four photographic sequences were taken: (1) just prior to the liquid dumps at GET 272:00:00, (2) 1 to 5 min after the dump, (3) 8 to 10 min after the dump, and (4) 25 to 28 min after the dump. A sequence consisted of a set of four exposures at 1, 20, 60, and 100 sec. The objective was "(1) to measure the intensity of the contamination cloud associated with the spacecraft in a clean configuration (just prior to a liquid dump with thrusters inhibited) and (2) to evaluate the impact of liquid dumping on seeing conditions."

Two 20-sec photographs at 8 to 10 and 25 to 28 min are shown in Figure A-28. Figure A-29 shows the association of a particle with the water and urine dump nozzles. It is seen that particle A is associated with the water dump nozzle. This choice is conclusive when the slope versus track length is plotted

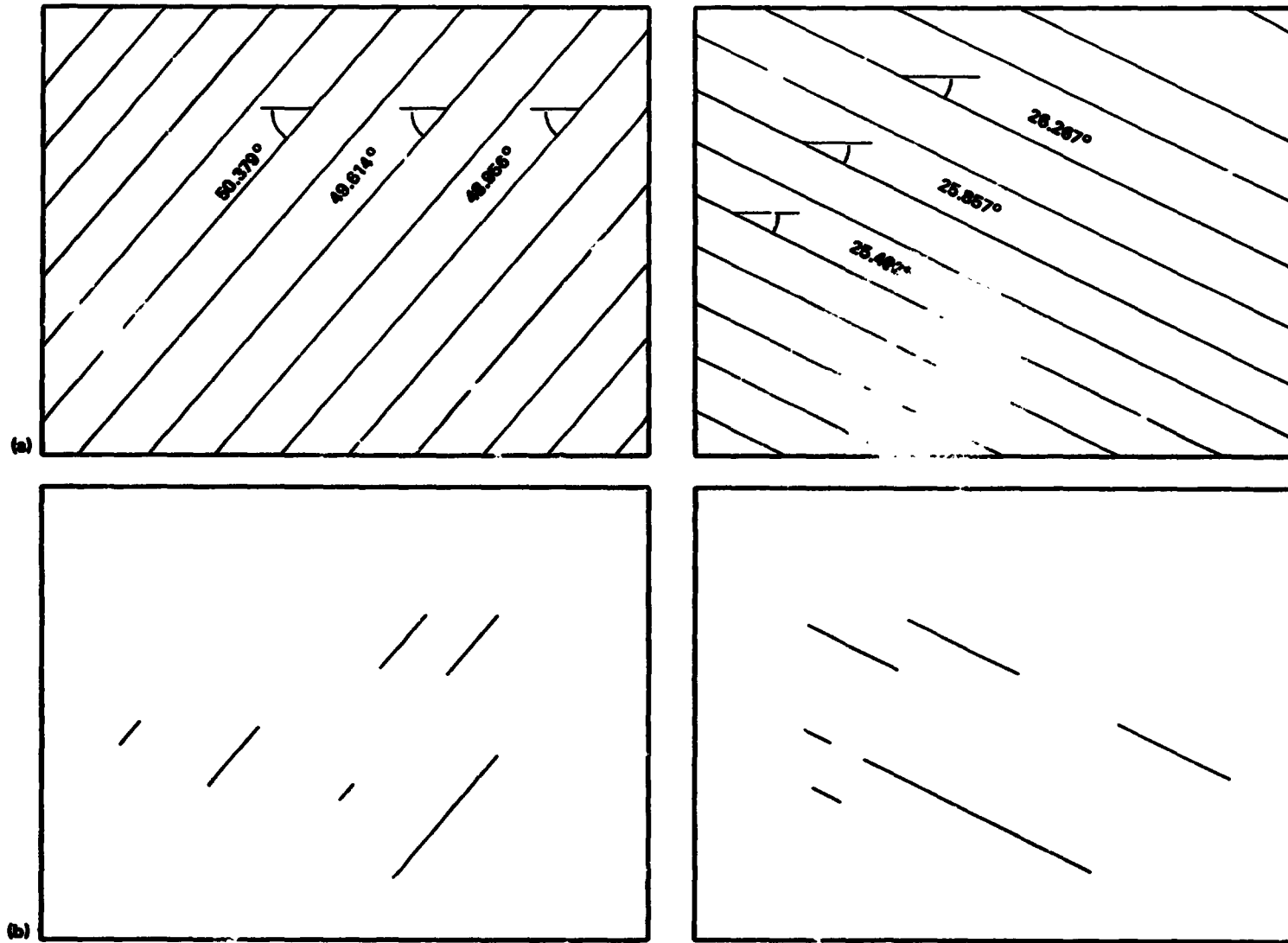


Figure A-23. Particle trajectories resulting from water dump from auxiliary dump nozzle and viewed from windows 2 and 4.

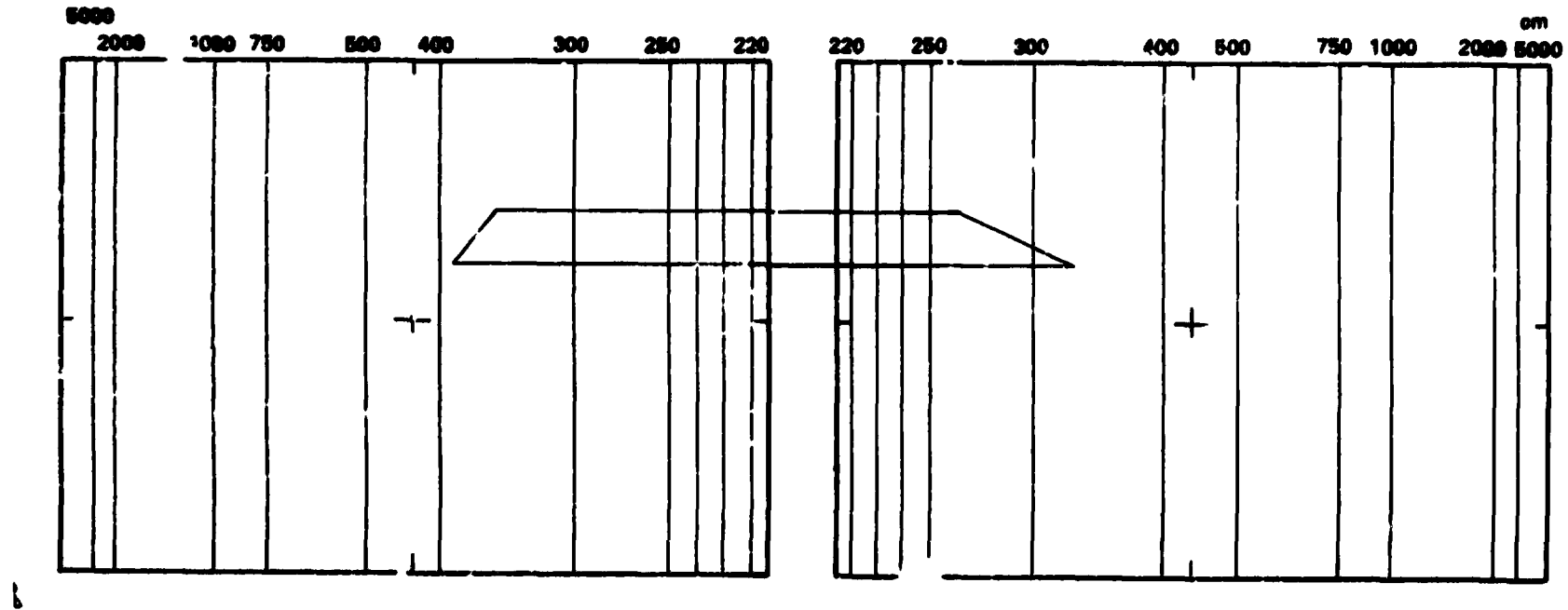


Figure A-24. Trajectory of particle from hatch dump nozzle as seen from window 2 (left) and 4 (right) simultaneously.

WATER DUMP NOZZLE

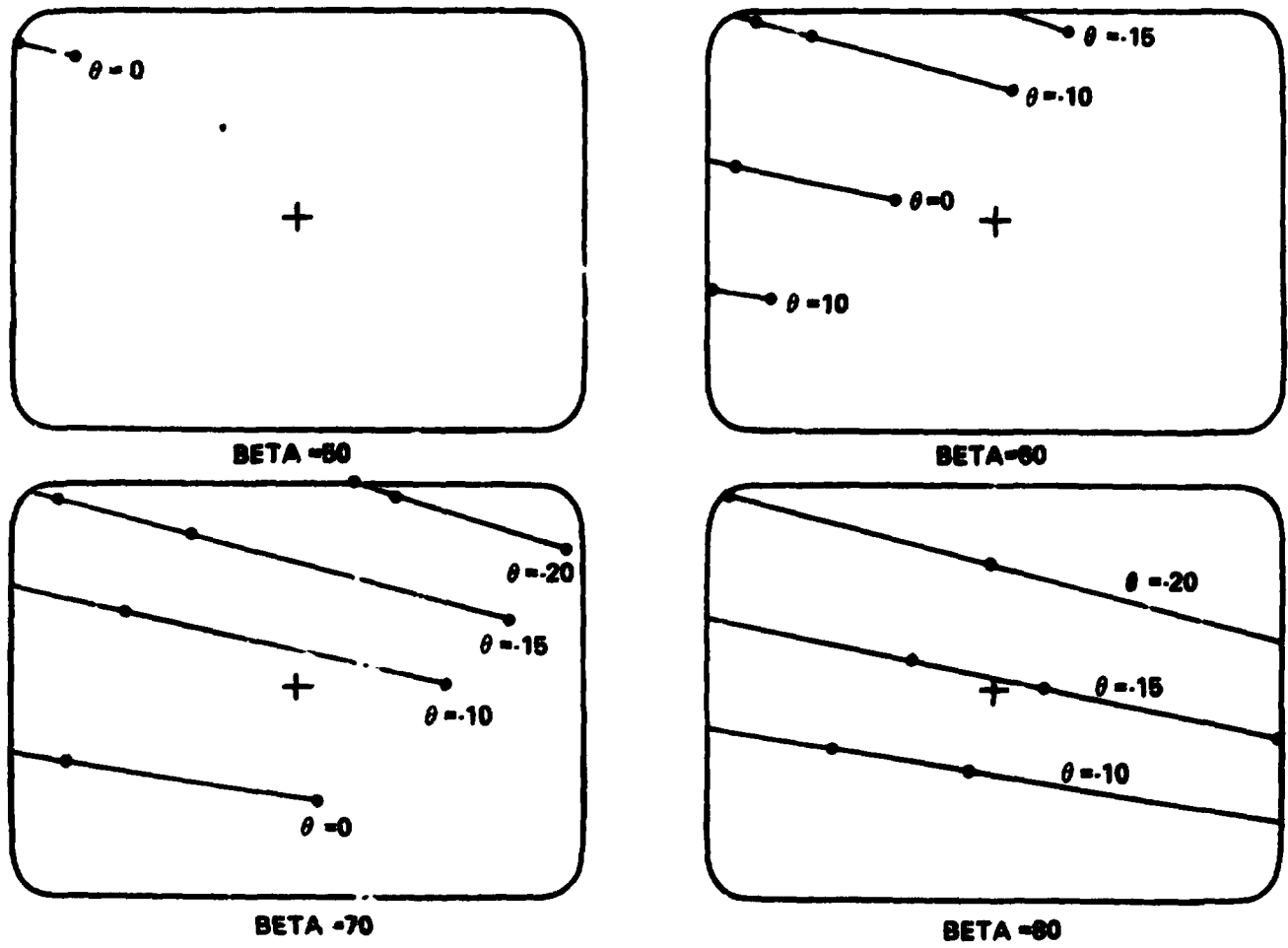


Figure A-25. Trajectories of particles from water dump seen from window 4 with a DAC.

TABLE A-1. WATER DUMP NOZZLE, $V = 1 \text{ m/sec}$

Beta Theat.	50			60			70			80		
	T	X	Y	T	X	Y	T	X	Y	T	X	Y
-20							6	-0.1221	0.9983	3	0.9285	0.9183
							7	-0.3088	0.9199	4	0.0253	0.5952
							20	-0.9546	0.6488	8	-1.0158	0.2228
-15				11	0.0410	1.0210	4	0.8358	0.8827	4	0.2901	0.1426
				12	-0.0136	0.9984	5	0.3766	0.7186	5	-0.1660	+0.0116
				20	-0.2450	0.9027	20	-0.7398	0.3196	11	-0.9961	-0.2268
-10				6	0.8305	0.9392	4	1.0685	0.4935	4	0.5621	-0.2748
				7	0.6325	0.8670	5	0.6055	0.3537	5	0.1001	-0.3790
				20	-0.0573	0.5157	20	-0.5244	0.0124	20	-1.0139	-0.6301
0	13	1.0305	0.8360	7	1.0555	0.2947	5	1.1016	-0.3091			
	14	0.9791	0.8183	8	0.9076	0.2534	6	0.8069	-0.3702			
	20	0.7697	0.7463	20	0.3384	0.0945	20	-0.8020	-0.5544			
10				12	1.0342	-0.3215	7	1.1394	-0.9865			
				13	0.9830	-0.3321	8	0.9852	-1.0062			
				20	0.7743	-0.3754						

URINE DUMP NOZZLE

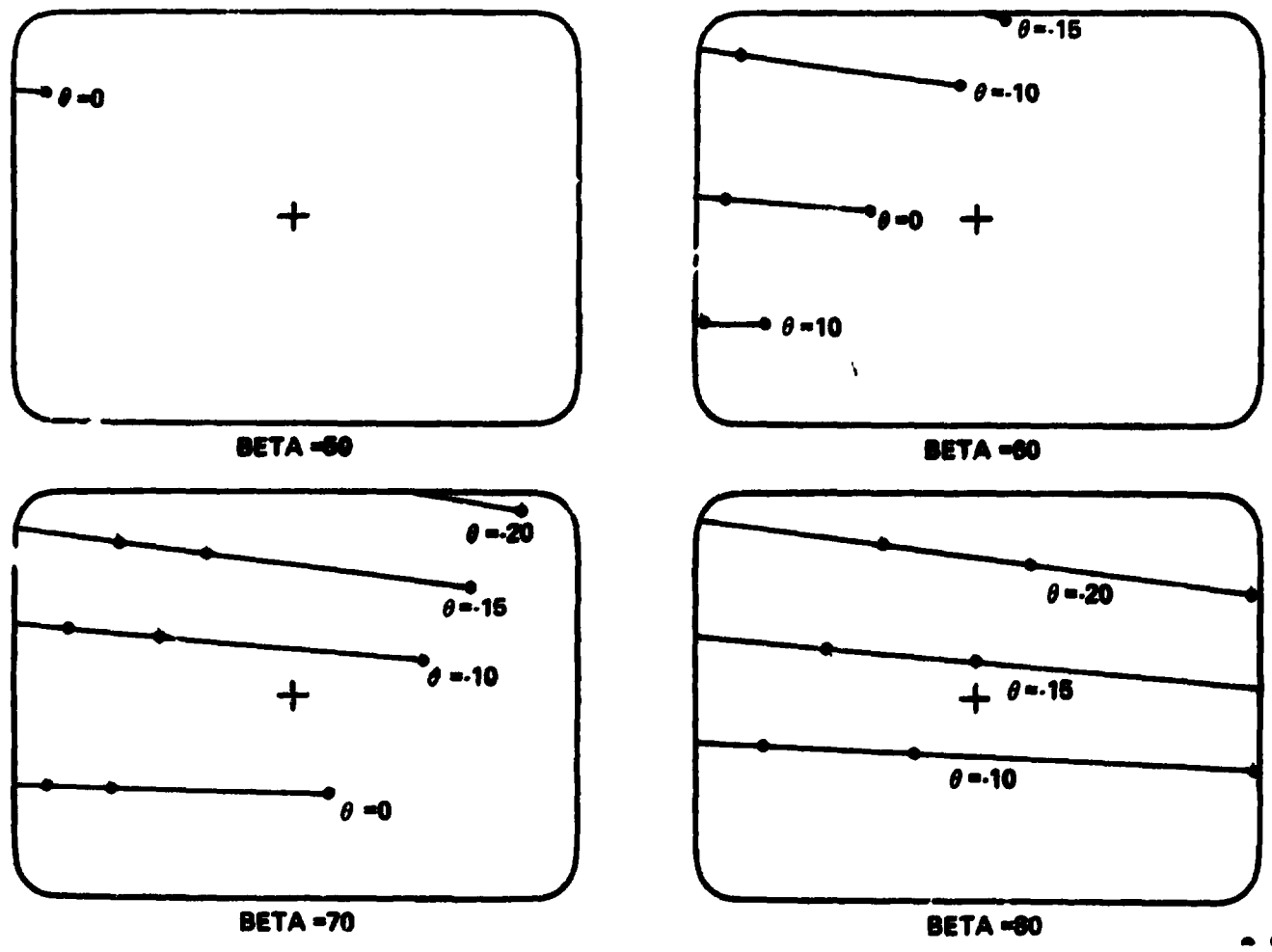


Figure A-26. Trajectories of particles from urine dump seen from window 4 with a DAC.

TABLE A-2. URINE DUMP NOZZLE, $V = 1$ m/sec

Beta Theta	50			60			70			80		
	T	X	Y	T	X	Y	T	X	Y	T	X	Y
-20							4	0.9891	1.0423	4	0.3349	0.4714
							5	0.4603	0.9841	5	-0.1898	0.4433
							20	-0.8222	0.8428	10	-1.0717	0.3961
-15				7	0.6875	1.0165	5	0.6220	0.5461	4	0.5301	-0.0299
				8	0.5263	0.9986	6	0.3039	0.5270	5	0.0099	-0.0282
				20	-0.0926	0.9299	20	-0.6532	0.4695	13	-1.0462	-0.0247
-10				6	1.0600	0.6754	5	0.7977	0.1364	4	0.7391	-0.4995
				7	0.8362	0.6596	6	0.4795	0.1317	5	0.2182	-0.4713
				20	0.0551	0.6042	20	-0.4807	0.1176	18	-1.0021	-0.4051
0	15	1.0297	0.5505	8	1.0133	0.0000	6	0.8718	-0.6064			
	16	0.9934	0.5484	9	0.8891	0.0000	7	0.6513	-0.5921			
	20	0.8860	0.5422	20	0.3783	0.0000	20	-0.1173	-0.5422			
10				9	1.0743	-0.3018	6	1.0936	-0.9607			
				10	0.9798	-0.2987	7	0.8671	-0.9379			
				20	0.5565	-0.2853	20	0.0777	-0.8586			

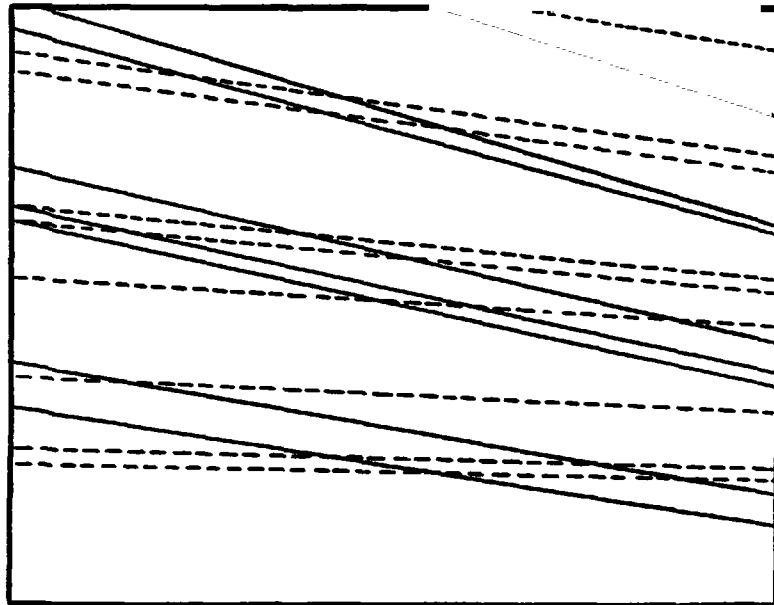


Figure A-27. Extended trajectories of particles from water and urine dumps as seen from window 4 (solid lines are from water dump nozzle; dashed lines are from urine dump nozzle).

(Fig. A-30). The slope varies because of spacecraft rotation. For near particles, the slope approaches that given for no rotation. Then, for these cases, the separation of particle species can be made. For particle B, if a β of 80 to 70 deg is assumed, then the velocity is approximately 80 to 135 cm/sec.

STELLAR CAMERA PHOTOGRAPHY

In lunar orbit the stellar camera on Apollo 15 recorded numerous bursts of particles. Figure A-31 is such an example. On Apollo 16 and 17 no phenomenon approaching such particle showers was recorded on the stellar camera. Very few frames had any contamination. On those showing contamination, the number of particles seen is small.

Correlation of the times of the particle showers on Apollo 15 with the times of the urine and waste water dumps has revealed that in most cases particles appear 4 hours after a dump and just after the terminator has been passed. Table A-3 gives the time of the initial frames showing tracks, the time of the dumps, and the time of the terminator.



a. 8-10 minutes after dump.



b. 28-28 minutes after dump.

Figure A-28. 20-sec photographs of water and urine dump;
photographs are from Apollo 15 [2].

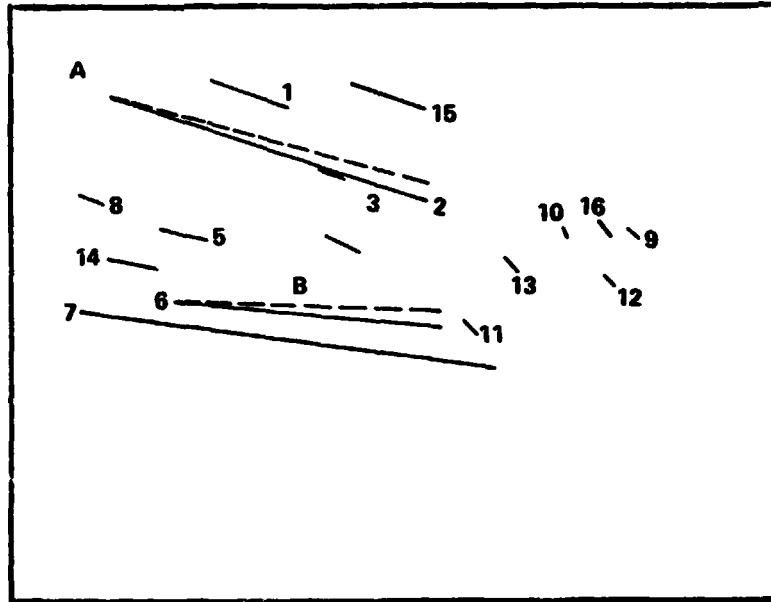


Figure A-29. Selected tracks from Figure 28(a); particle A is associated with the water dump, and particle B with the urine dump nozzle.

The stellar camera was not extended during any dumps. All extensions, with one exception, were approximately 2 to 4 hours after dumping had ended.

Figure A-32 shows again the trajectories from Figure A-31 which appear to come from a source. However, there are several trajectories which are randomly oriented. Also shown on Figure A-32 are the tracks which would appear if the particles had originated from the reaction control system A-1 engine or the waste water dump nozzle. Since these particles do not match the observed ones, another source must be sought.

When the tracks are extended, there is a localization of track crossings at 65.6 deg below and 69.2 deg to the right of the frame. Employing the rough position for the origin of the tracks, the origin would have to lie on a line defined in stellar camera coordinates by:

$$y_s = -x_s \tan 69.2 \text{ deg}$$

$$z_s = -x_s \tan 65.6 \text{ deg}$$

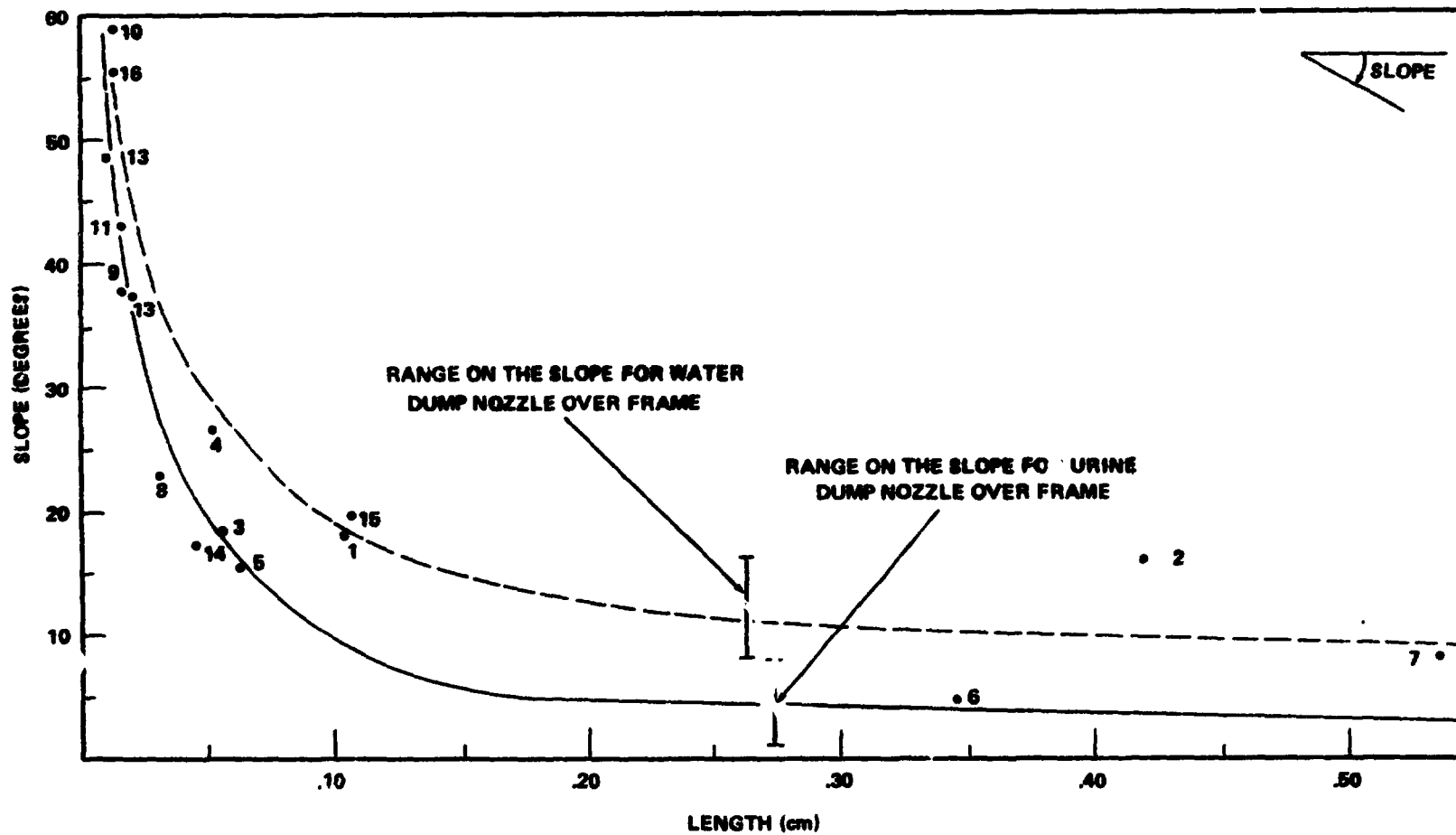
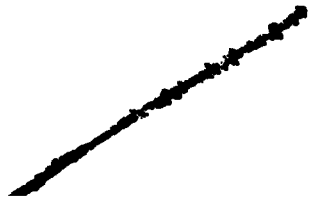


Figure A-30. Slope versus track length for particles from urine and water dump nozzle (numerals correspond to particle numbers in Figure A-29).



REPRODUCIBILITY OF THE ORIGINAL PAGE IS POOR,

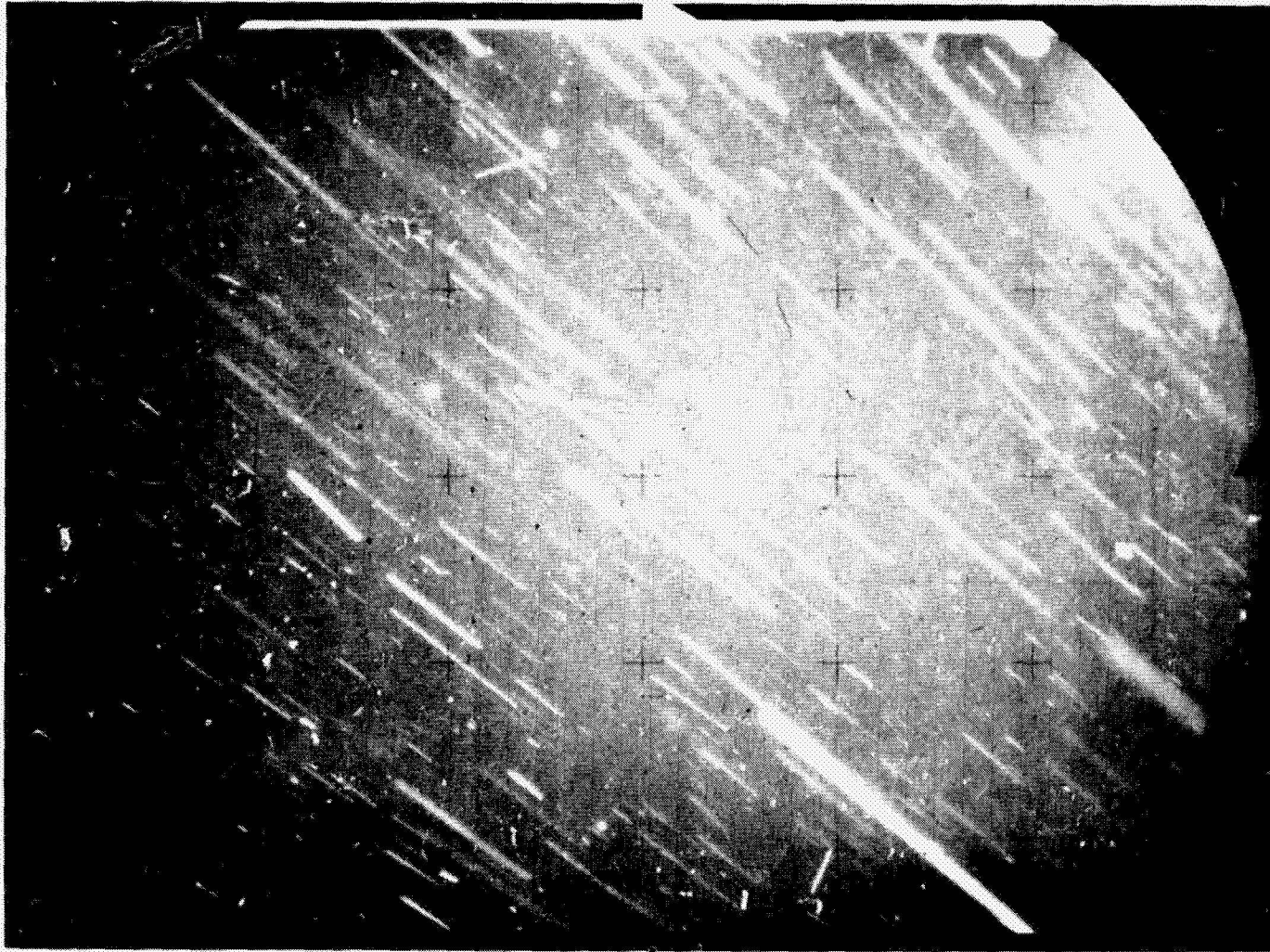


Figure A-31. Example of stellar camera frame from Apollo 15 which records a particle shower.

TABLE A-3. TIME CORRELATION OF STARS WITH STELLAR CAMERA
 FRAMES CONTAIN. MINATION

GET for Dump ^a	GET for Terminator	GET for Initial Photograph	REV
80:20	84:42	84:48	4
97:52			
125:20	129:26	129:32	27
146:59			
170:25	174:50	174:54	50
193:59	194:32	194:35	60

a. Times supplied by Robert Giesecke of Johnson Space Center.

This line is shown on Figure A-33, after a transformation to spacecraft coordinates. The dashed portion of the line is within the interior of the spacecraft. Since the origin would be on the spacecraft skinline, there are two origins, one within 0.5 m of the stellar camera and the other in front of CM window 1. Both positions have no known vents associated with them.

The extend/retract times and times for maneuvers which may affect the stellar camera are given in Table A-4. The extension at 194:30 corresponds to the end of the time allotted (1 hour) for a urine dump.

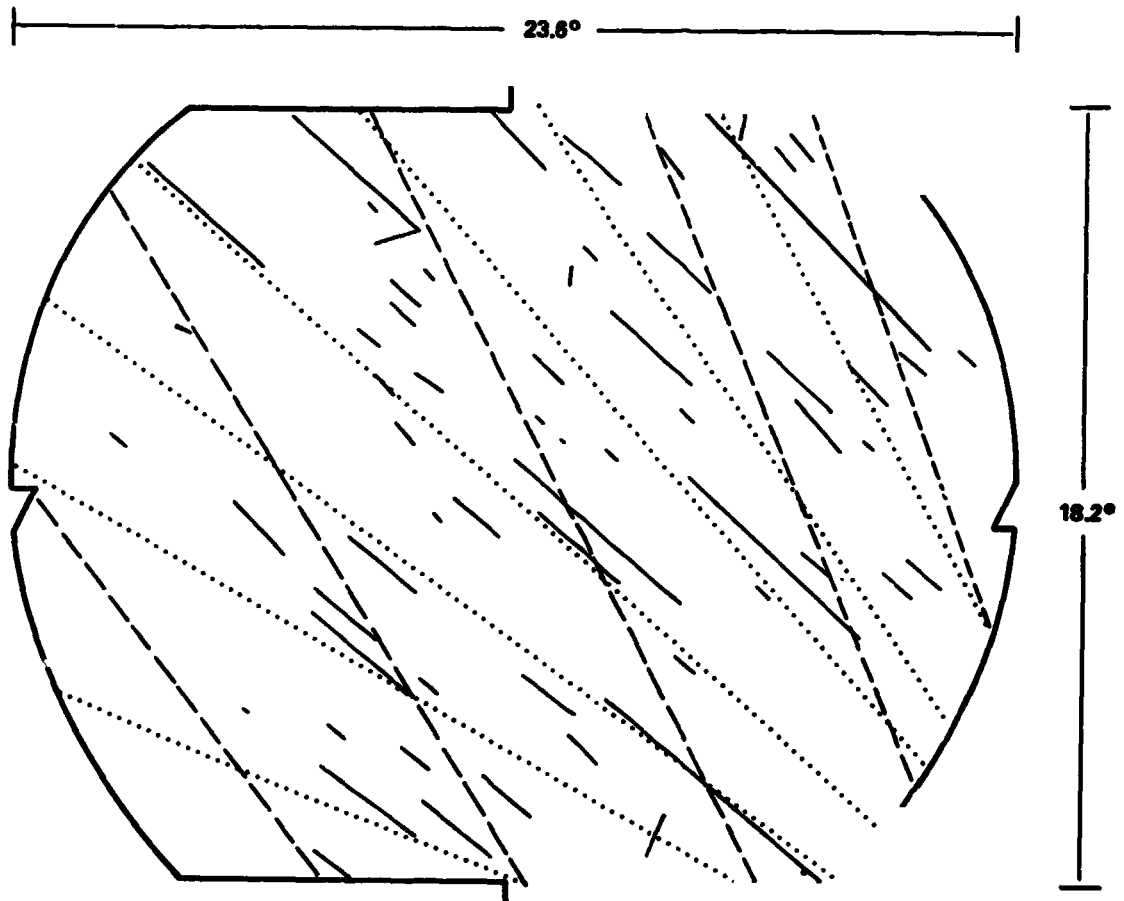


Figure A-32. Trajectories of Figure A-31 retraced to show relationship to particles from reaction control system A-1 engine (dashed line) and waste water dump (dotted line).

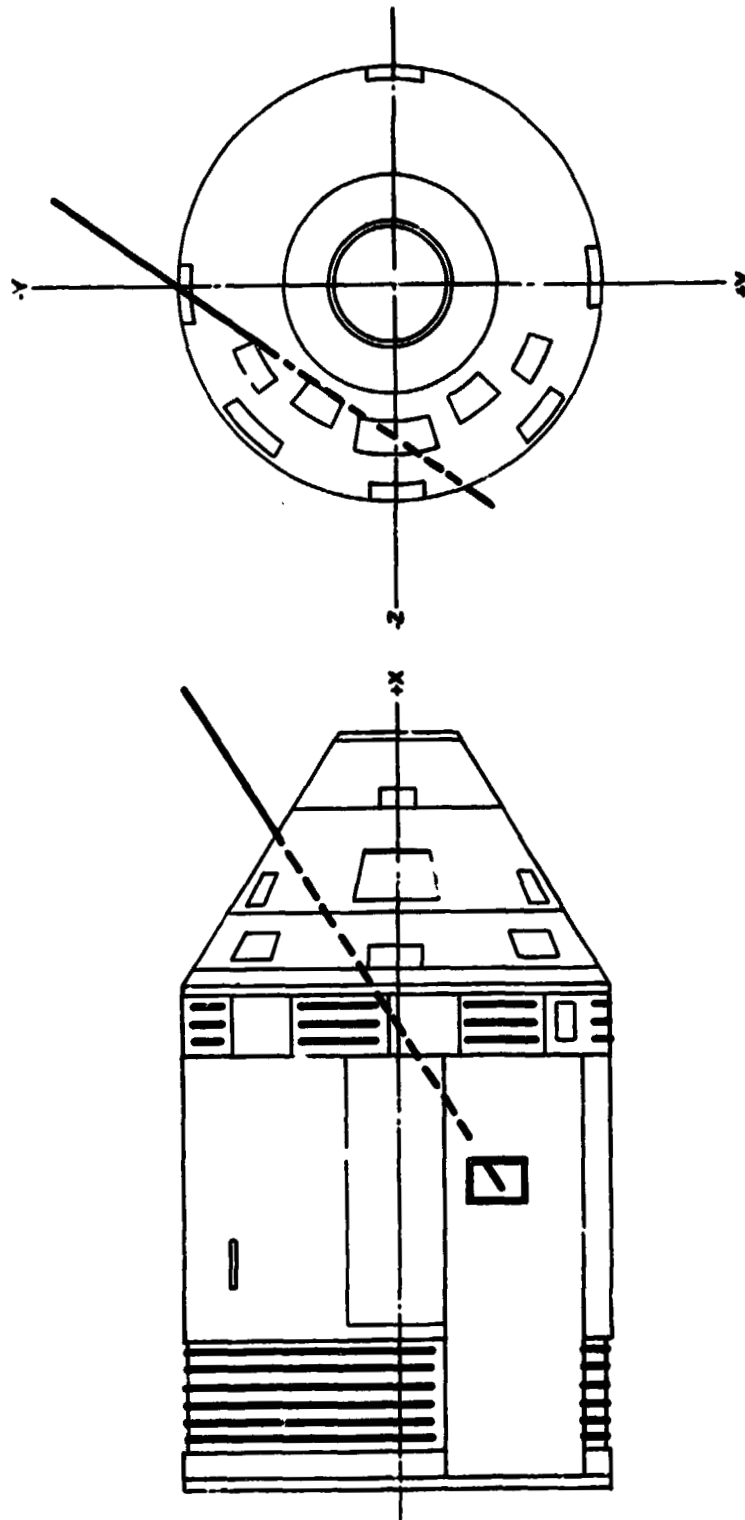


Figure A-33. Locus of origins for particle tracks seen in Apollo 15 stellar camera frame.

TABLE A-4. TIME OF EVENTS WHICH MAY GENERATE PARTICLES

GET Extend	GET Retract	GET Maneuver	Maneuver
84:07	95:12	84:11	+x forward
128:30	130:40	125:47	+x forward
150:02	152:13	145:04	40° north oblique
174:40	175:31	173:15	+x forward
194:30	195:30	193:30	+x forward

REFERENCES

1. Craven, P. D. and Gary, G. A.: Contamination Photography, Experiment Proposal for Manned Space Flight. Marshall Space Flight Center, April 1971.
2. Naumann, R. J.: Apollo 15 Contamination Photography. NASA TM X-6081, July 5, 1972.
3. Goetzl, C. G. and Singletory, J. B., eds.: Space Materials Handbook. Lockheed Missiles and Space Co., Sunnyvale, Calif., 1962, pp. 183 and 475-478.
4. Applying the Sensitometry and Identification to the Very High Speed Black and White Film (VHBW). Manned Spacecraft Center, FCSD, Report No. CF74-A-824B, December 15, 1970.
5. Sensitometry Application to the Very High Speed Black and White Film for Use in the Nikon 35 mm Camera. Manned Spacecraft Center, FCSD, Report No. CD42-A-830, July 6, 1971.
6. Weinberg, J. L.: The Zodiacal Light at 5300\AA . *Annales d'Astrophysique*, vol 27, 1964.
7. Smith, L. L., Roach, F. E., and Owen, R. W.: The Absolute Photometry of Zodiacal Light. *Planetary and Space Sciences*, vol. 13, 1965.
8. Smith, L. L., Roach, F. E., and Owen, R. W.: A Photometric Map of the Milky Way. BNWL-1419, Battelle Memorial Institute, June 1970.
9. McPherson, D. G.: Apollo Telescope Mount Extended Applications Study Program, ATM Contamination Study. Ball Brothers Research Corp., NASA Contractor Report CR-61173, May 25, 1967.
10. Goldstein, H.: *Classical Mechanics*. Addison-Wesley Publishing Co., Inc., Reading, Mass., 1950.
11. Born, M. and Wolf, E.: *Principles of Optics*. Pergamon Press, Oxford, 1950, pp. 153 and 163.
12. Selwyn, E. W. H.: *Photography and Astronomy*. Eastman Kodak Co., 1950.
13. Gucker and Tuma: *J. Colloid and Interface Science*, vol. 27, 1968.

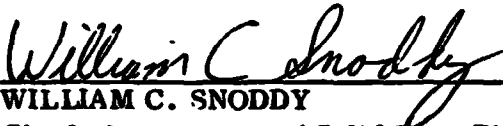
APPROVAL

APOLLO-SKYLAB CONTAMINATION PHOTOGRAPHY (S226)

By P. D. Craven and G. A. Gary

The information in this report has been reviewed for security classification. Review of any information concerning Department of Defense or Atomic Energy Commission programs has been made by the MSFC Security Classification Officer. This report, in its entirety, has been determined to be unclassified.

This document has also been reviewed and approved for technical accuracy.



WILLIAM C. SNODDY
Chief, Astronomy and Solid State Physics Division